8-2016

Advances in Monitoring Dynamic Hydrologic Conditions in the Vadose Zone through Automated High-Resolution Ground-Penetrating Radar Images and Analysis

Adam R. Mangel
Clemson University

ADVANCES IN MONITORING DYNAMIC HYDROLOGIC CONDITIONS IN THE VADOSE ZONE THROUGH AUTOMATED HIGH-RESOLUTION GROUND-PENETRATING RADAR IMAGING AND ANALYSIS

A Dissertation
Presented to
the Graduate School of
Clemson University

In Partial Fulfillment
of the Requirements for the Degree
Doctor of Philosophy
Environmental Engineering

---

by
Adam R. Mangel
August 2016

Accepted by:
Stephen M.J. Moysey
Lawrence C. Murdoch
Ronald W. Falta
Christophe Darnault

ABSTRACT

This body of research focuses on resolving physical and hydrological heterogeneities in the subsurface with ground-penetrating radar (GPR). Essentially, there are two facets of this research centered on the goal of improving the collective understanding of unsaturated flow processes: i) modifications to commercially available equipment to optimize hydrologic value of the data and ii) the development of novel methods for data interpretation and analysis in a hydrologic context given the increased hydrologic value of the data.

Regarding modifications to equipment, automation of GPR data collection substantially enhances our ability to measure changes in the hydrologic state of the subsurface at high spatial and temporal resolution (Chapter 1). Additionally, automated collection shows promise for quick high-resolution mapping of dangerous subsurface targets, like unexploded ordinance, that may have alternate signals depending on the hydrologic environment (Chapter 5). Regarding novel methods for data inversion, dispersive GPR data collected during infiltration can constrain important information about the local 1D distribution of water in waveguide layers (Chapters 2 and 3), however, more data is required for reliably analyzing complicated patterns produced by the wetting of the soil. In this regard, data collected in 2D and 3D geometries can further illustrate evidence of heterogeneous flow, while maintaining the content for resolving wave velocities and therefore, water content. This enables the use of algorithms like reflection tomography,

which show the ability of the GPR data to independently resolve water content distribution in homogeneous soils (Chapter 5).

In conclusion, automation enables the non-invasive study of highly dynamic hydrologic processes by providing the high resolution data required to interpret and resolve spatial and temporal wetting patterns associated with heterogeneous flow. By automating the data collection, it also allows for the novel application of established GPR data algorithms to new hydrogeophysical problems. This allows us to collect and invert GPR data in a way that has the potential to separate the geophysical data inversion from our ideas about the subsurface; a way to remove ancillary information, e.g. prior information or parameter constraints, from the geophysical inversion process.

DEDICATION

For Tom, Robin, Kristy, Nicholas, and Katie Mangel for all their support over the years, especially Mom and Dad who have done more for me than they will ever know.

For my EEES family for the years of problem solving, focus, collaboration, and celebration over the past six years, especially Kenneth Dunn who was always excited to learn something about our projects and help us out in any way possible.

Lastly, and wholeheartedly, to Joseph Thomas Kreusch, my friend who was always there regardless of the conditions, ready to cause a little trouble or simply be the most genuine person I've ever met. To my friend who never got the chance to truly live; never got the chance to flex his sheer genius and excel in academia like we all knew he would have. One of God's own prototypes. A high-powered mutant of some kind never considered for mass production. Too weird to live, and too rare to die.

ACKNOWLEDGEMENTS

This material is based upon work supported by, or in part by, the US Army Research Office (W911NF-10-1-0365, W911NF-10-1-0292), and the National Science Foundation (EAR-1151294). We would also like to thank Clemson University for a generous allotment of compute time on the Palmetto Cluster.

TABLE OF CONTENTS **PAGE**

TABLE OF CONTENTS (CONTINUED) **PAGE**

TABLE OF CONTENTS (CONTINUED) **PAGE**

TABLE OF CONTENTS (CONTINUED) **PAGE**

LIST OF TABLES **PAGE**

LISTOF FIGURES **PAGE**

LISTOF FIGURES (CONTINUED) **PAGE**

LISTOF FIGURES (CONTINUED) **PAGE**

LISTOF FIGURES (CONTINUED) **PAGE**

LISTOF FIGURES (CONTINUED) **PAGE**

LISTOF FIGURES (CONTINUED) **PAGE**

LISTOF FIGURES (CONTINUED) **PAGE**

LISTOF FIGURES (CONTINUED) **PAGE**

CHAPTER 1 - AUTOMATED HIGH-RESOLUTION GPR DATA COLLECTION FOR MONITORING DYNAMIC HYDROLOGIC PROCESSES IN TWO AND THREE DIMENSIONS

NOTICE: This chapter has been published in the February 2015 issue of the Society of Exploration Geophysicist's journal, The Leading Edge: Special Issue on Near-Surface Geophysics. The full citation is listed below.

Mangel, A.R., B.A. Lytle & S.M.J. Moysey, 2015. Automated high-resolution GPR data collection for monitoring dynamic hydrologic processes in two and three dimensions. *The Leading Edge*, 34(2), pp.190–195.

1.1 Abstract

An automated GPR data collection system was constructed to monitor dynamic hydrologic processes with high spatiotemporal resolution. The design of the system allows for fast acquisition of constant-offset profiles (COPs) and common-midpoint surveys (CMPs) to monitor unsaturated flow at multiple locations. A fast and accurate motion control system allows us to study high-resolution spatial patterns of reflectors through time while preserving important information about the normal moveout of reflectors for velocity analysis. Two examples where infiltration was monitored using time-lapse GPR measurements in two and three dimensions are discussed. The data from both experiments provide substantial qualitative insight about the dynamics of hydrologic events and a path forward for quantitative analysis of surface based GPR monitoring data. We show i) the

advantages of collecting high-resolution time-lapse data, ii) the complexities of patterns associated with the wetting of the soil, and iii) evidence of non-uniform propagation of a wetting front through the soil column.

1.2 Introduction

Accurate positioning and rapid data collection are required for high resolution time-lapse monitoring using ground-penetrating radar (GPR). Given that sub-wavelength spacing is required for full 3D resolution during static imaging [*Grasmueck et al.* 2005], high-speed, time-lapse imaging introduces significant technical challenges for acquiring the data. Compromises are often made when collecting time-lapse data sets by either increasing the time between repeated measurements or by decreasing the spatial data coverage. The manual operation of commercially available systems makes it difficult to obtain the high resolution required in both space and time to monitor highly dynamic hydrologic events (e.g., infiltration) in real time. Therefore, systems which are capable of quickly and accurately positioning GPR antennas are needed to enable time-lapse surveys.

Over the past decade, many advances in the design of GPR systems have been made. Increases in data acquisition speeds have made it possible to collect more data in a short amount of time while interfaces with global positioning systems provide high resolution information for spatial registration of the data. However, practitioners are still responsible for positioning the GPR antennas. Some companies (e.g. Mala, 3D Radar, Niitek) have designed multi-channel antenna arrays which make it possible to cover swaths of an imaging area in a single pass and thus substantially reduce survey times. However, large singular units comprised of an array of antennas are not ideal for fast, multi-offset data collection given their size and limited capabilities for obtaining data at large offsets.

Therefore it would be advantageous to incorporate the versatility to change the function and orientation of the antennas into the system design.

GPR has recently received attention as a tool for monitoring near-surface hydrology as it has the potential to provide non-invasive hydrogeophysical data over a large area [*Grasmueck et al.* 2010; *Grote et al.* 2005; *Haarder et al.* 2011; *Huisman et al.* 2001; *Mangel et al.* 2012; *Moysey* 2010; *Steelman and Endres* 2010; *Truss et al.* 2007; *Vellidis et al.* 1990]. In these studies, the sampling time between traces and the spatial extent of the data are highly variable. For example, the study of *Moysey* [2010] represents the extreme sacrifice of spatial data to minimize time between repeated measurements. In this study, the author collected GPR data using a set of stationary bistatic antennas and showed that trajectories of specific arrivals on time-lapse GPR data are associated with hydrologic phenomena and can be used to estimate hydrologic parameters. However, due to the spatial limitations of the GPR data, the author was forced to assume a one-dimensional flow system. In contrast, the study of *Grasmueck et al.* [2010] represents a sacrifice of time to increase the spatial extent and resolution of the data. In this study, the authors monitored infiltration into a fractured carbonate bedrock using 3D time-lapse GPR (200 MHz) data collected over a 20 m x 20 m area. A laser positioning system coupled to the GPR provided feedback via a LED guidance system to ensure that high-resolution data were collected. The authors were able to create a 3D rendering of local time shifts in the data associated with a 4 m diameter zone of water propagating through the bedrock over a period of 5 days. While the data were very high resolution in space, i.e., 0.05 m line spacing, it took between

105-180 minutes to acquire a single data set. While in any experiment the researchers must determine the best trade-off between spatial and temporal resolution, an ideal GPR system would automate the data collection process to provide both.

In this paper we present an automated bistatic GPR data collection system that is coupled to a motion controller for accurate and independent, high-speed positioning of antennas. Using two examples where we monitor infiltration in two and three dimensions in a sand tank, we illustrate the capabilities of the automated system. Furthermore, we show that GPR, when coupled with automated data collection, is capable of collecting representative data of highly dynamic events, like infiltration, at high resolution in time and space.

1.3 Methods

To study unsaturated flow using GPR, a 4 m x 4 m wooden tank was constructed and filled to a depth of 0.60 m with river sand. The base of the tank is divided into 16 - 1 m x 1 m drainage cells, each of which drains independently to the exterior of the tank. In order to collect time-lapse GPR data over the tank in the most efficient way possible, we chose to automate the data collection process using a bistatic radar system which is mounted to a motorized gantry.

1.3.1 System Design

We use LabVIEW Software (National Instruments) to integrate the radar and positioning aspects of the data acquisition. The positioning control system is equipped

with a motion control board (NI PCI-7334, National Instruments) which interfaces with a four axis motion controller (NI UMI-7774, National Instruments). This interface controls three motor drivers and motors that allow independent positioning of the antennas along a 1.6 m gantry, which can itself be moved in the perpendicular direction. This configuration allows us to position the antennas at any location in the tank at offsets up to 1.2 m (Figure 1.1). Positioning accuracy in the x and y-directions are 0.02 cm and 0.0004 cm, respectively.

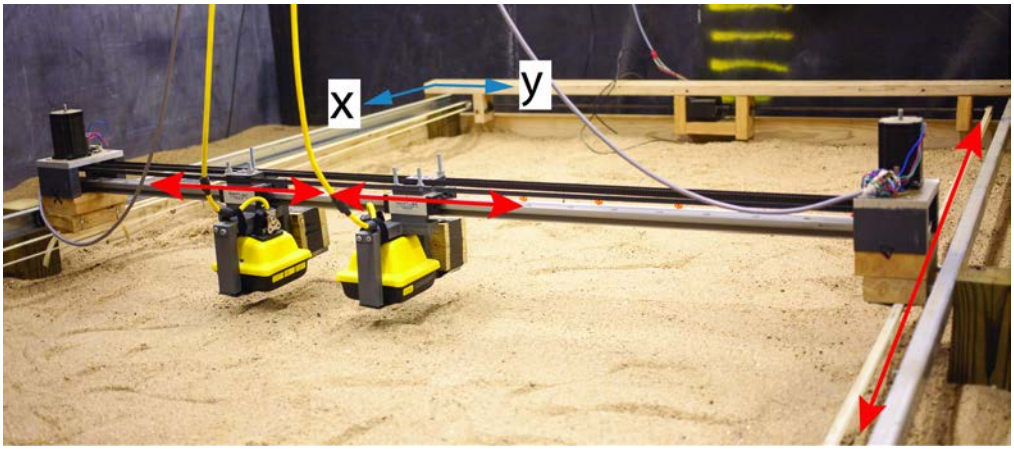

Figure 1.1: Picture showing the setup of the automated gantry and the relative motion of all the components.

For the GPR component, the system is equipped with the PulseEkko SPIDAR system (Sensors and Software, Mississauga, Ontario, Canada) which allows radar data collection to be controlled using a standard PC interfaced with a Network Interface Controller (NIC). The NIC is a microprocessor based module that provides complete control of the GPR system. Standard GPR acquisition parameters can therefore be set

through the LabVIEW interface, e.g. time window, sample interval, and trace frequency. For the majority of our work, we use 1000 MHz shielded antennas to obtain high resolution data with depth, although other frequencies are available. Traces are typically acquired at a rate of 100 traces per second using 4 stacks to keep acquisition time per trace at a minimum. At optimal operation, the system is able to continuously collect data at points spaced, on average, 0.05 cm apart, at a linear collection rate of 50 cm/sec and an area collection rate of 20 cm^2/sec.

1.4 Time Lapse imaging of a 2D Profile during Infiltration

To demonstrate the high temporal resolution of the system, an infiltration event in a tank was monitored using the automated GPR system. An impermeable object was embedded in the sand at the xyz-coordinate [2.0 m, 2.0 m, 0.06 m] to induce preferential flow. Time-lapse ground penetrating radar data consisting of common offset profiles (COPs) and common midpoint profiles (CMPs) were collected along a line bisecting the irrigated area at x = 2.0 m using the automated gantry system (Figure 1.2). Three CMPs were collected sequentially along the line with source-receiver offsets ranging from 0.16 to 1.03 m. The third CMP had a maximum offset of only 0.67 m due to the limited length of the gantry. The CMPs were followed by a COP with a source-receiver offset of 0.16 m, which profiled 0.65 m along the length of the antenna rail. This four profile cycle was repeated 100 times over 22 minutes, with approximately 13 seconds between replicate traces and collecting 137,377 traces in total.

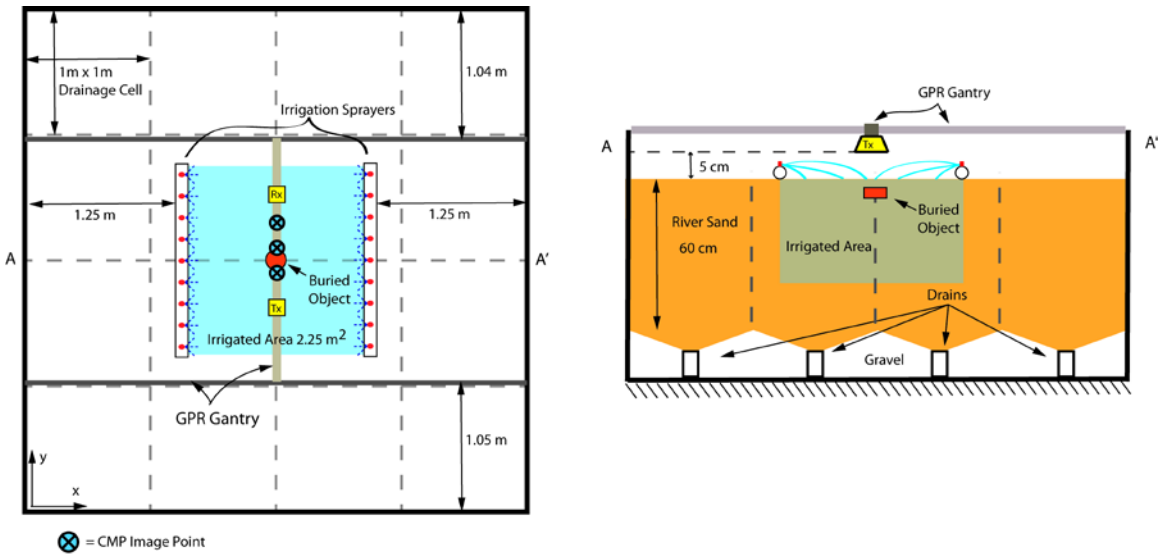

Figure 1.2: Experimental setup for 2D infiltration experiment.

Irrigation was uniformly applied to the sand surface using two 1.5 m sprayer arrays consisting of micro-sprayers mounted along PVC pipes. Flow to the irrigation sprayers was held constant at 8 LPM and applied to an effective area of 2.25 m^2, resulting in an average flux of 0.356 cm/min. Irrigation began one minute after the start of data collection and terminated after 22 minutes.

1.4.1 Results and Discussion

Changes in the CMP profiles are clearly visible when comparing data collected during irrigation (Figure 1.3). Before irrigation (Figure 1.3a, c, e), the CMPs show arrivals between 2 – 8 ns that have a moveout consistent with the electromagnetic velocity of air and that obscure the groundwave. The reflection from the base of the sand (B) is clearly visible at 9.5 ns traveltime at 0.16 m offset. After 1.5 minutes of irrigation each CMP

shows the appearance of an arrival associated with the wetting of the soil (W) in addition to the base of the sand reflection (B) (Figure 1.3b, d, f). There is also an increase in the traveltime and a reduction in the amplitude of the base of sand reflection (B) due to the wetting of the sand. While we suspect (W) to be a reflection caused by the wetting front moving through the soil column, the complicated moveout of this arrival makes it difficult to analyze. However, the high spatial and temporal acquisition of the data allows us to consider the appearance of this arrival in alternative projections that facilitate our interpretation.

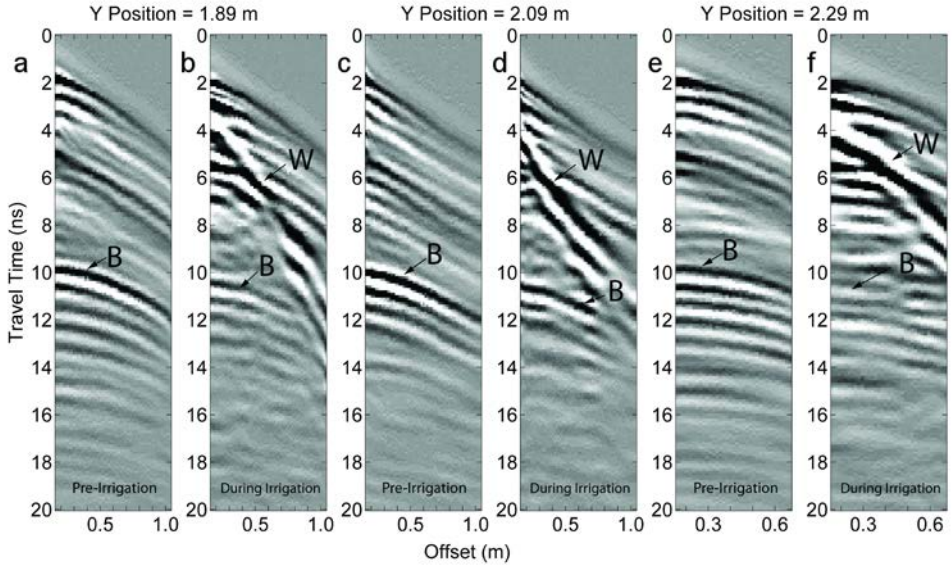

Figure 1.3: Common midpoint GPR profiles collected at three locations before irrigation (a, c ,e) and after 1.5 minutes of irrigation (b, d, f) to illustrate the changes in arrivals present in the profile. The base of tank arrival (B) is visible in all profiles, while the wetting front arrivals (W) are only visible after irrigation begins.

Figure 1.4a and b show how the first traces of the CMPs (i.e., at 0.16 m offset) in Figure 1.3a and e evolve during the infiltration experiment. Here, we can see a shift in the arrival time for the bottom of sand arrival (B) and wetting arrival (W) as the irrigation progresses. The base of sand reflection, initially at 9.5 ns, displays a trajectory with an increasing arrival traveltime after the onset of irrigation. At y = 1.89 m, (Figure 1.4a) the traveltime for the bottom of sand arrival has nearly doubled, arriving at the receiver at approximately 17 ns. Similarly, at y = 2.29 m (Figure 1.4b), the same arrival has only shifted to a traveltime of 14 ns. This difference indicates uneven wetting of the soil column as radar waves appear to be moving faster at y = 2.29 m than at y = 1.89 m. The arrival from the wetting front (W) follows a similar traveltime trajectory as (B) for the duration of the experiment; however, with a significantly greater slope. Given the larger slope of (W) when compared to (B), the traveltime of this arrival must also be changing due to an increasing depth to the reflector if a uniform velocity behind the wetting front is assumed.

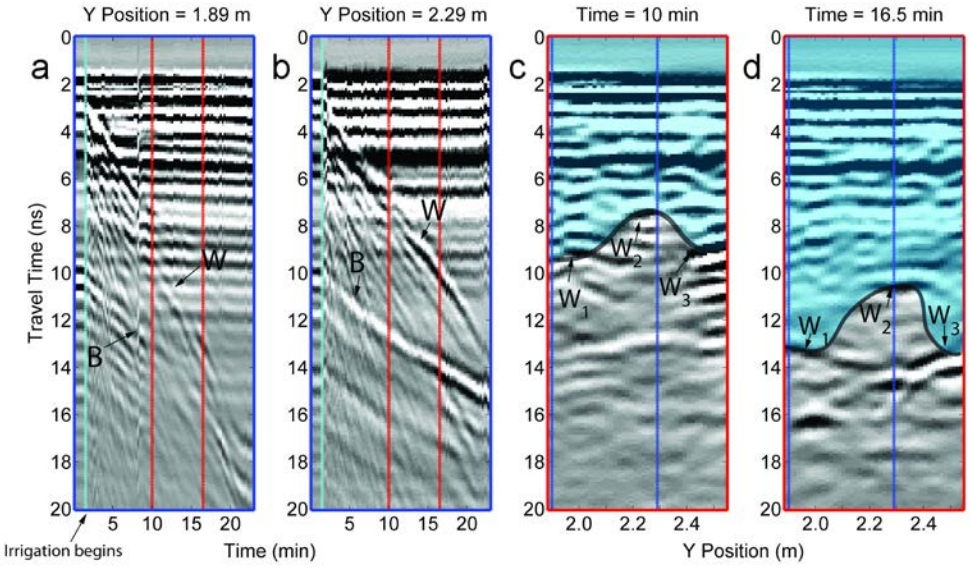

Figure 1.4: Time and space projections of the 2D data set showing the movement of the bottom of sand reflection (B) and the wetting front reflection (W): a) constant offset traces collected at y = 1.89 m and b) y = 2.29 m over time, c) and d) are COPs collected at 10 min and 16.5 min, respectively. The variable wetting front arrivals in space are labeled (W_1), (W_2), and (W_3) in (c) and (d). Vertical dashed red lines in (a) and (b) indicate the times of profiles (c) and (d); vertical dashed blue lines in (c) and (d) indicate the locations of time gathers in (a) and (b). The solid vertical line in (a) and (b) indicates the start of irrigation.

Additionally, we can see that the changes in wetting front (W) and base of sand (B) arrivals are not consistent through space. The wetting front arrival intersects the base of tank arrival at the edges of the profile area significantly earlier in the experiment than in the center of the tank. From Figure 2.4a, we can see that at y = 1.89 m, the wetting front and base of tank arrival intersect 20 minutes into the experiment, however, the two arrivals do not intersect during the experiment at y = 2.29 m (Figure 1.4b). The transport of water to the bottom of the tank at y = 1.89 m was verified as water was observed to drain from

this portion of the tank at 22 minutes into the experiment, whereas drainage was not observed elsewhere.

In addition to observing arrival (W) in the time-lapse images, it is also easily seen in constant offset profiles. If we interpret (W) as an arrival associated with the movement of a wetting front through the soil column, and we project the data along the profile, we can constrain the shape of the reflector in space for a given time. The blue shaded area in Figures 2.4c and 2.4d indicate the interpreted shape of the wetted zone over the profile. In the COP collected at 10 minutes, indicated by the vertical dashed red lines at 10 minutes on the trajectory gathers in Figures 2.4a and 2.4b, the wetting front reflection is visible at 7 ns near the center of the profile (W_2) and 9 ns at the margins (W_1,W_3) (Figure 1.4c). Later in the experiment at 16.5 minutes (Figure 1.4d), the spatial discontinuity of this reflector has increased as the wetting front arrival is observed at roughly 10.3 ns near the center of the profile (W_2) and 13 ns traveltime at the margins of the profile (W_1, W_2).

With this experiment, we conclude that GPR data with high temporal resolution are valuable for capturing variability in hydrologic processes. Arrivals associated with the wetting of a soil can have complex shapes in time and space. GPR systems designed to rapidly acquire data have the capability of monitoring highly dynamic hydrologic events and capturing heterogeneities in the wetting patterns of infiltrating wetting fronts. Most importantly, the capability to view data from multiple perspectives enhances the recognition of specific arrivals and improves interpretation of the patterns present in the data.

1.5 3D Time Lapse imaging during Infiltration

To demonstrate the high spatiotemporal resolution of the automated GPR system, an infiltration event in a tank was monitored in 3D. Time-lapse GPR measurements were used to monitor changes in the arrivals of a system containing an embedded impermeable object at the xyz-coordinate [2.93 m, 2.0 m, 0.06 m] in homogenous river sand. Drip irrigation was applied to the surface at a rate of 0.075 LPM for 30 minutes using a 1 cm diameter rubber hose located directly above the buried object. The GPR data consisted of a 3D data set collected as 51 COPs followed by 2 CMPs collected over a 0.5 m x 0.6 m imaging area (Figure 1.5). The 51 COPs were collected by profiling along the x-direction. The CMPs were collected directly over the buried object as well as at a location outside the irrigated area. This data collection cycle was repeated at 5 minutes, 20 minutes, and 30 minutes during the experiment, where each data set took roughly 2.5 minutes to collect resulting in 65,864 traces in total.

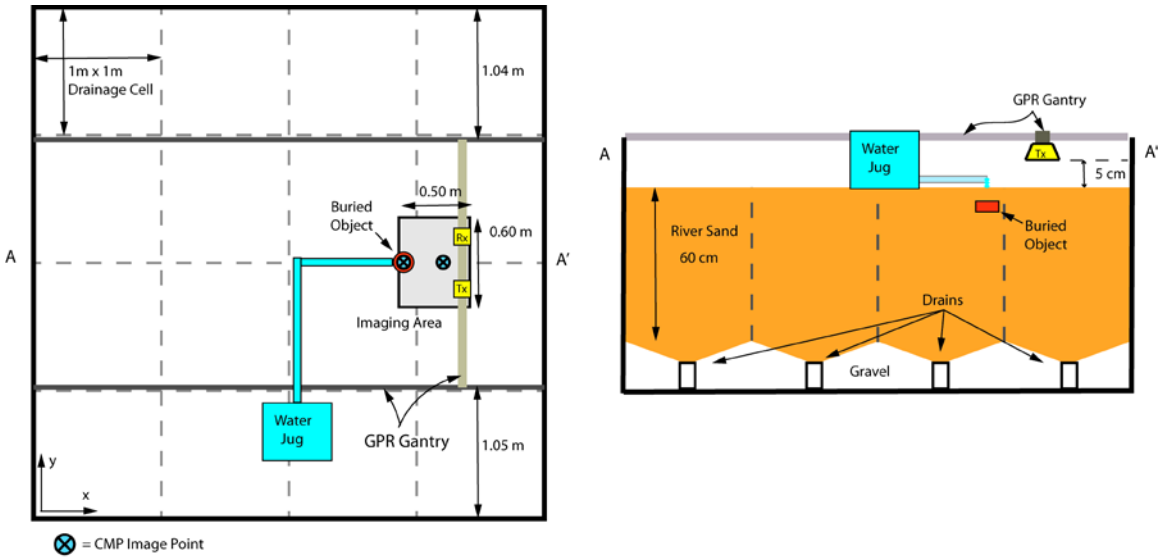

Figure 1.5: Experimental setup for 3D experiment

1.5.1 Results and Discussion

Changes caused by the applied irrigation are evident in arrivals on the COPs collected over the buried object (Figure 1.6 and Figure 1.7). Selected arrivals include the bottom of sand reflection (B), buried object diffraction (M) and anomalous arrivals (A_1) and (A_2). Prior to irrigation, the buried object arrival (M) is difficult to identify due to the small contrast in the dielectric properties of the buried object relative to the dry sand background (Figure 1.6a, and Figure 1.7a). After 5 minutes of irrigation, (M) is clearly identified given the increased contrast in dielectric permittivity. Additionally, there is a significant amount of ringing present in the data that indicates the trapping of radar waves in the wetted zone around the buried object (Figure 1.6b, Figure 1.7b). After 20 minutes of irrigation, (M) is easily identified in the y-profile (Figure 1.6c), but obscured on the x-

profile by arrivals associated with the wetting of the sand (A_1) (Figure 1.7c). After the sand was irrigated for 30 minutes the buried object arrival remains clear in the y-profile (Figure 6d) but cannot be identified in the x-profile (Figure 1.7d). This shows the advantage of collecting time-lapse data given the abrupt appearance of the buried object in the data after the onset of irrigation; however, interpretation becomes complicated when 2D sections are considered alone. Given that these complexities are also present in the CMPs over the buried object (not shown), 3D projections of the data can improve recognition of spatial patterns present in the arrivals and interpretation of their causes.

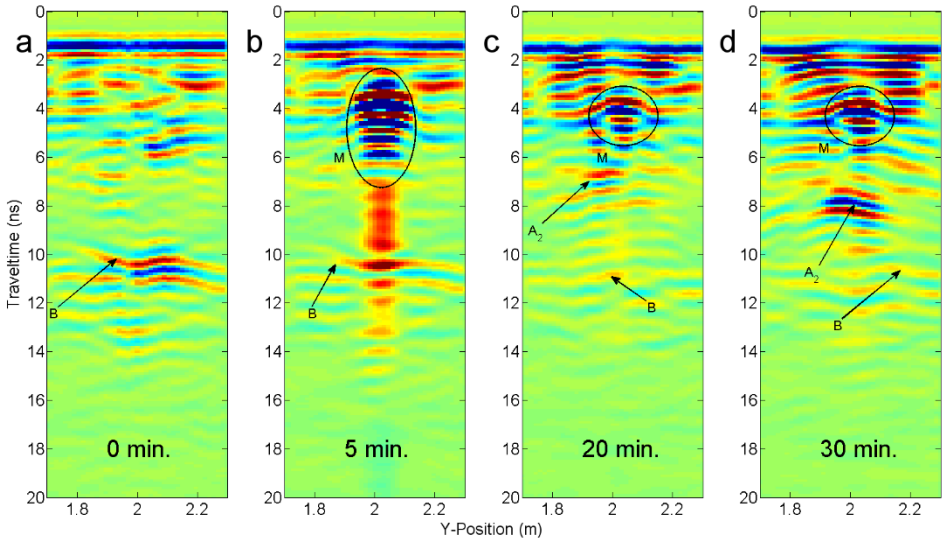

Figure 1.6: COPs collected in the y-direction at x = 2.93 m showing the bottom of sand reflection (B) at 0.60 m depth, the buried object diffraction (M) at 0.06 m depth, and two anomalous arrivals associated with the wetting of the soil (A_1, A_2) at a) initial conditions, b) after 5 minutes of irrigation, c) after 20 minutes of irrigation, and d) after 30 minutes of irrigation.

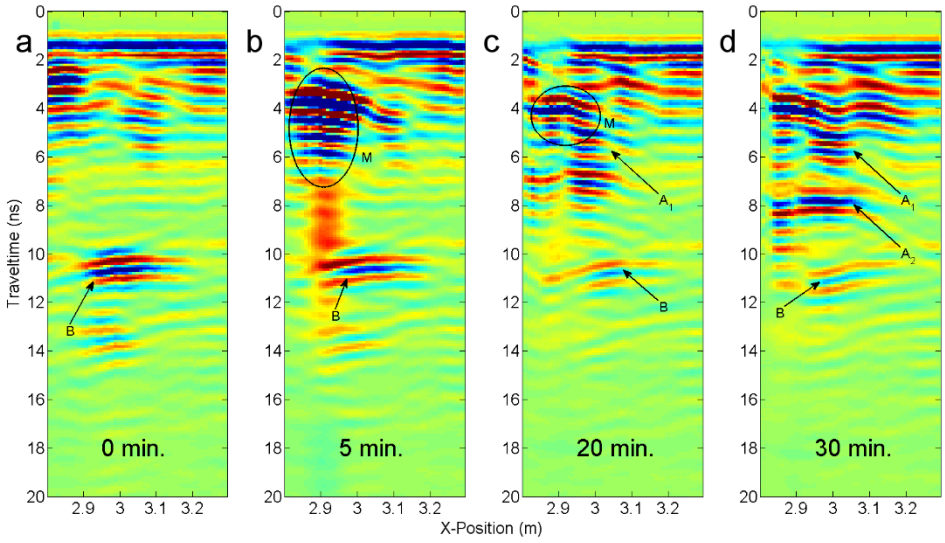

Figure 1.7: COPs collected in the x-direction at y = 2.0 m showing the bottom of sand reflection (B) at 0.60 m depth, the buried object diffraction (M) at 0.06 m depth, and two anomalous arrivals associated with the wetting of the soil (A_1, A_2) at a) initial conditions; b) after 5 minutes of irrigation; c) after 20 minutes of irrigation; and d) after 30 minutes of irrigation.

Figure 1.8 shows the common-offset data cubes collected for the given experiment times as 3D isosurface plots. The smoothed envelope of the GPR data was used to produce these figures using a smoothing window of 5 data points in the x, y, and z-directions. A vertical black line indicates the center of the buried object in the 3D volume. The bottom of tank arrival (B) is indicated by the green isosurface, arrivals associated with the buried object (M) are indicated as red, and arrivals associated with water moving through the soil column (A_1, A_2) are blue.

The bottom of sand arrival is clearly identified in all data cubes as an arrival with relatively constant amplitude at 10 ns traveltime. Regardless of the ability to project the

data as a 3D volume, the buried object arrival remains difficult to identify at initial conditions due to the low contrast with the sand and is not plotted (Figure 1.8a). However, in Figure 1.8b and c, the buried object arrival (M) and the ringing event are clearly identified by high amplitude arrivals, as seen in Figure 1.6b and Figure 1.7b. Projecting the data in 3D allows us to confirm the target identification given the shape of the arrival in the 3D space. The buried object is also identified after 20 minutes of irrigation; however, it is worth noting here that identification of the buried object in Figure 1.8c may be difficult if the data in Figure 1.8b were absent. Figure 1.8d shows the final data set, collected after 30 minutes of irrigation. While Figure 1.8d shows a red volume indicating the presence of the object, note that it was difficult to separate the buried object arrival from surrounding arrivals associated with water moving through the soil column.

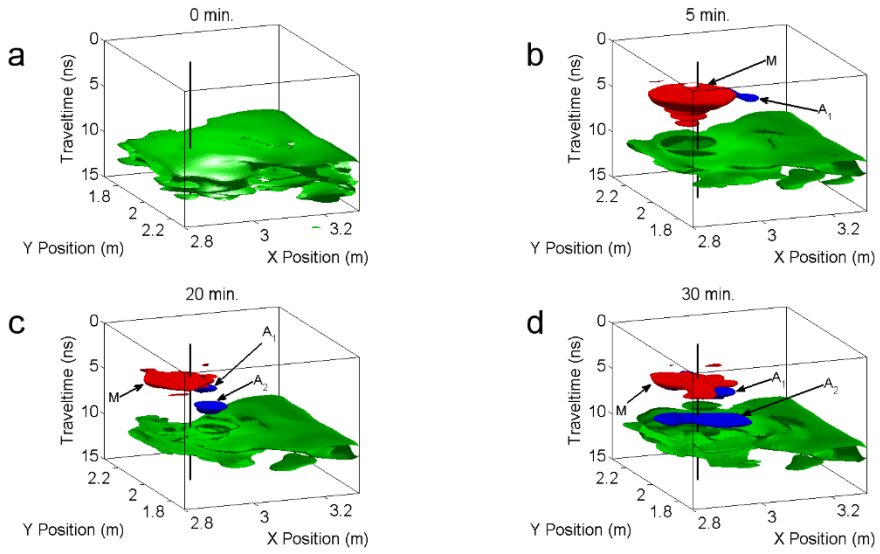

Figure 1.8: Volume plots of arrivals represented as isosurfaces within the data volumes for the bottom of sand arrival (green) at 0.60 m depth, buried object diffraction (red) at 0.06 m depth, and anomalous reflectors associated with water moving through the soil (blue). Specific instances of the buried object and anomalous reflectors are indicated as (M), (A_1) and (A_2), respectively.

In addition to (M) and (B), we see additional arrivals (A_1 and A_2) that appear to be associated with water moving around the impermeable object. At 5 minutes after irrigation, the fact that (A_1) is adjacent to the isosurface of the buried object indicates this arrival is associated with water moving laterally around the impermeable object (Figure 1.8b). This arrival continues to grow in volume over time indicating more of this area is being wetted. A second arrival (A_2) associated with water moving through the soil appears after 20 minutes of irrigation (Figure 1.8c). Given the increase in traveltime of (A_2) from 20-30 minutes of irrigation, we can expect a local increase in water content or downward movement of water in the soil column (Figure 1.8c and d). Additionally, the growth of

(A_2) in the x-direction from Figure 1.8c to 8d indicates lateral spreading of water in the soil at the scale of 0.20 m.

Although arrivals in 2D profile sections can easily become convoluted by changes in the state of a system, projecting data using a 3D volume can facilitate interpretations by providing information regarding the shape of reflectors in space. Additionally, time-lapse imaging can greatly improve interpretation by showing the hydrologic response of a system over time. Objects which may be geophysically invisible for a given hydrologic state are easily identified when the system is altered. With this experiment, we conclude that rapid, high-resolution GPR data collection used to monitor dynamic hydrologic events can reveal the time dependent response of arrivals and image reflectors in 3D space, greatly improving interpretation of the data and the subsurface.

1.6 Conclusions

A fully automated approach to collecting time-lapse surface based GPR data was evaluated using two examples of monitoring infiltration. In our 2D study, we showed that high resolution GPR data collection is capable of simultaneously capturing spatial and temporal variability in the wetting of a soil while collecting valuable multi-offset data for velocity analysis. Furthermore, in our 3D study, we showed that high resolution GPR data collection in time and space is extremely valuable to understanding spatial patterns created by the movement of water through the soil column. Additionally, we showed the advantage of time-lapse data over static data sets when attempting to identify targets that may possess similar dielectric properties as the media in which they are embedded. In conclusion, GPR

data collection systems used to monitor hydrologic events must be efficiently designed to capture highly dynamic patterns associated with underlying hydrologic processes that vary rapidly in space and time.

1.7 Acknowledgements

This material is based upon work supported by, or in part by, the US Army Research Office (W911NF-10-1-0365, W911NF-10-1-0292), and the National Science Foundation (EAR-1151294).

CHAPTER 2 - RESOLVING PRECIPITATION-INDUCED WATER CONTENT PROFILES BY INVERSION OF DISPERSIVE GPR DATA: A NUMERICAL STUDY

NOTICE: This chapter has been published in the June 2015 issue of the Journal of Hydrology. The full citation is listed below.

Mangel, A.R., S.M.J. Moysey & J. van der Kruk, 2015. Resolving precipitation induced water content profiles by inversion of dispersive GPR data: A numerical study. *Journal of Hydrology*, 525, pp.496–505. Available at: http://linkinghub.elsevier.com/retrieve/pii/S0022169415002607.

2.1 Abstract

Surface-based ground-penetrating radar (GPR) measurements have significant potential for monitoring dynamic hydrologic processes at multiple scales in time and space. At early times during infiltration into a soil, the zone above the wetting front may act as a low-velocity waveguide that traps GPR waves, thereby causing dispersion and making interpretation of the data using standard methods difficult. In this work, we show that the dispersion is dependent upon the distribution of water within the waveguide, which is controlled by soil hydrologic properties. Simulations of infiltration were performed by varying the *n*-parameter of the Mualem-van Genuchten equation using HYDRUS-1D; the associated GPR data were simulated to evaluate the influence of dispersion. We observed a notable decrease in wave dispersion as the sharpness of the wetting front profile

decreased. Given the sensitivity of the dispersion effect to the wetting front profile, we also evaluated whether the water content distribution can be determined through inversion of the dispersive GPR data. We found that a global grid search combined with the simplex algorithm was able to estimate the average water content when the wetted zone is divided into 2 layers. This approach was incapable, however, of representing the gradational nature of the water content distribution behind the wetting front. In contrast, the shuffled complex evolution algorithm was able to constrain a piece-wise linear function to closely match the shallow gradational water content profile. In both the layered and piece-wise linear case, the sensitivity of the dispersive data dropped sharply below the wetting front, which in this case was around 20 cm, i.e., twice the average wavelength, for a 900 MHz GPR survey. This study demonstrates that dispersive GPR data has significant potential for capturing the early-time dynamics of infiltration that cannot be obtained with standard GPR analysis approaches.

2.2 Introduction

Significant advances have recently been made using ground-penetrating radar (GPR) to study near-surface water content in both static [*Greaves et al.* 1996; *Grote et al.* 2010; *Huisman et al.* 2001; *Vellidis et al.* 1990] and dynamic conditions [*Haarder et al.* 2011; *Mangel et al.* 2012; *Moysey* 2010; *Steelman and Endres* 2010; *Truss et al.* 2007; *van Overmeeren et al.* 1997]. In time-lapse studies, it is common to see large increases in water content at the surface associated with infiltration events which create a high permittivity region of the soil column. When the thickness of this zone is comparable to the wavelength of the GPR signal, electromagnetic (EM) wave dispersion can occur [*Arcone* 1984; *van der Kruk et al.* 2006]. Several experimental studies of this phenomenon have focused on scenarios with distinct wet and dry zones separated by a wetting front [*Steelman et al.* 2010; *Strobbia and Cassiani* 2007; *van der Kruk et al.* 2006; *van der Kruk* 2006; *van der Kruk et al.* 2009a; *van der Kruk et al.* 2009b; *van der Kruk et al.* 2010]. In reality, however, these waveguides in soils may have non-uniform distributions of water content associated with gradual changes between wet and dry soil. Given that i) waveguide boundaries are derived from water content profiles and ii) wave dispersion is caused by interference between multiple shallow reflections, it is our hypothesis that hydrologic properties of a soil, e.g., capillarity, will affect the dispersion of GPR waves.

Low-velocity dispersive waveguides occur when a high permittivity layer is bounded by relatively low permittivity layers, e.g., a thin wetted layer of soil at the surface that traps GPR waves by causing total reflection at both the upper and the lower interface

of the waveguide [*van der Kruk et al.* 2006]. During the infiltration process, for example, reflections can occur at the boundary between the wetted and non-wetted layers of the media [*Mangel et al.* 2012] as well as at the air-soil interface. At shallow depths comparable to the wavelength of the GPR signal, this high permittivity wetted layer can act as a dispersive waveguide trapping GPR waves and causing the groundwave to appear as a package of dispersed waves [*van der Kruk et al.* 2009a]; the waveguide dispersion itself being caused by the interference of the multiple overlapping reflections trapped within the waveguide.

Dispersion curves are picked from the maximum of the phase-velocity spectrum calculated from multi-offset GPR data (Figure 2.1); this spectrum shows the frequency-dependent phase-velocity for a given waveguide. Inversion of dispersion curves was found to be a reliable method for determining the average relative permittivity of both the waveguide layer (ε_1) and underlying halfspace (ε_2), as well as the thickness (h) of the single-layer waveguide [*van der Kruk et al.* 2006; *van der Kruk* 2006]. There is no literature available, however, documenting how the sharpness of the lower boundary of a hydrologically derived waveguide will affect dispersion of the GPR energy and the resulting inversion for waveguide properties. While these studies [*van der Kruk et al.* 2006; *van der Kruk* 2006] applied dispersion analysis to field data, and likely encountered a hydrologically induced boundary, the authors did not comment on any effects caused by the distribution of water at the reflection interface. The authors do comment, however, on

the possibility of heterogeneities in the subsurface affecting the dispersion of the EM energy, and reserved further investigation for later studies.

Partially addressing heterogeneities in the waveguide, *van der Kruk et al.* [2010] collected three sets of 200 MHz common mid-point GPR data over a region where successive amounts of water added via natural rainfall altered the properties of the waveguide. *van der Kruk et al*. [2010] noted inconsistencies when inversion results were compared to measured permittivity from soil cores collected at the field site, which they attributed to the heterogeneous distribution of water within the waveguide compared to the dry soil beneath. The study illustrates the importance of understanding how a vertically heterogeneous waveguide, e.g., water content profile, affects the dispersion of GPR waves and how this influences the average value of permittivity obtained through inversion of the data. Additionally, *van der Kruk et al.* [2010] inverted dispersion curves using a two-layer model. When compared to the results from the single-layer waveguide inversion, the authors noted that the weighted arithmetic mean of the two waveguide layers obtained from the two-layer waveguide inversion (ε_1 & ε_2) was very similar to the first layer permittivity (ε_1) returned from the single-layer waveguide inversion. Given these results, it is clear that the two-layer conceptual model can better explain the dispersion caused by more complex water content profiles that may arise from multiple wetting events.

The work of *van der Kruk*, [2006], *van der Kruk et al.*, [2006], and *van der Kruk et al.*, [2010] illustrated how to utilize the dispersion to invert for properties of the waveguide, but little has been done to evaluate the effect of heterogeneity of the waveguide and its

effect on dispersion. Recently, *van der Kruk et al*. [2012] investigated the effects of interface roughness, heterogeneities, and dipping layers on the inversion of dispersive GPR data. To test their hypotheses, *van der Kruk et al*. [2012] numerically generated permittivity distributions using stochastic methods. This allowed the authors to test the generalizability of the inversion scheme to heterogeneous systems and investigate how dispersion changes given these conditions. The heterogeneities studied by these authors did not, however, account for spatial patterns typical of wetting events, which are the basis for precipitation-induced waveguides. The relationship between dispersion and hydrology therefore needs to be further explored, e.g., using numerical simulations as an initial mode of investigation.

In this paper we use dispersion analysis [van der Kruk et al., 2006] as a tool for evaluating the radar response of diffuse interfaces commonly encountered in the subsurface as a result of infiltration. This will be done through the evaluation of results from inversion of the dispersion curves from simulated multi-offset 2D GPR simulations in a 1D hydrologic context. This paper will apply the dispersion curve inversion method outlined by *van der Kruk et al.* [2006] and *van der Kruk et al.* [2010] in homogeneous soils with variable influence of capillarity during infiltration. Specifically, we will use the phase-velocity spectra from 2D GPR simulations to fit average permittivities of two layer models as outlined in *van der Kruk et al.* [2010]. We also use a multiple layer inversion, based on a piece-wise linear function, to represent the water content profile. It is our hypothesis that as the lower boundary of the waveguide becomes more diffuse the dispersion will decrease,

i.e., as capillarity dominates the flow regime the number of dispersive modes observed will decrease. We will also show that utilizing a conceptual model capable of representing the gradational nature of the water content profile produces a better representation of the dispersion curve data.

2.3 Background Information

While we provide a brief overview of the fundamentals of EM wave dispersion, a comprehensive overview of the modal theory equations and GPR pulse propagation in surface waveguides can be found in *Arcone et al.* [2003]. For more information about the waveguide model, the generation of theoretical dispersion curves, and inversion of dispersion curves, see *van der Kruk et al.* [2006], *van der Kruk* [2006] and *van der Kruk et al.* [2009a].

2.3.1 Dispersive Waveguide Theory

Modal theory states that incident energy will form into several modes consisting of specific frequencies, related to waveguide properties, traveling at their own phase velocity within the dispersive waveguide [*Arcone* 1984]. For a single waveguide layer of thickness (h) the fundamental equation of modal theory [*Budden* 1961] is defined as:

$$1 - R_{12}(f,\theta)R_{10}(f,\theta)\exp[-2\gamma_1 h\cos\theta] = 0 \qquad (2\text{-}1)$$

where $\gamma_1 = j\omega\sqrt{\varepsilon_1}/c_0$ is the propagation constant for GPR waves, where c_0 is the speed of light in a vacuum, ε_1 is the relative permittivity of the waveguide, f is frequency, θ is the angle of incidence, ω is the angular frequency, and R_{12} and R_{10} are the reflection

coefficients for the lower and upper boundary of the waveguide, respectively. In order to satisfy (Eq. 2-1) for guided waves, two constraints are required. First, the reflection coefficients at each interface must have amplitude equal to one. In order for this to happen, θ must exceed the critical angle (θ_c) which is dependent upon the permittivity of the waveguide (ε_1) and lower (ε_2) layer (Eq. 2-2a).

$$\theta_c = \sin^{-1}\left(\sqrt{\frac{\varepsilon_2}{\varepsilon_1}}\right) \tag{2-2a}$$

Thus, if the offset between the antennas does not allow for the measurement of the GPR wave beyond the critical angle, dispersion will not be observed in the data. By analyzing the phase component from the Fourier transform of Eq. (2-1) and substituting the propagation constant we obtain

$$\phi(\theta) - \frac{4\pi f\sqrt{\varepsilon_1}h\cos(\theta)}{c_0} = -2m\pi \tag{2-2b}$$

which shows that the total phase change (ϕ) after upper and lower interface reflections including twice the propagation through the waveguide must equal $2m\pi$ radians where *m* is an integer corresponding to the dispersive mode [*van der Kruk* 2006].

2.3.2 Empirical dispersion curves from CMP data

To determine the phase-velocity spectra for empirical data, the GPR data must first be transformed from the time-domain to the frequency domain. The method of *Park et al.* [1998] was employed by *van der Kruk et al.* [2006] in which the Fourier Transform of the

common mid-point GPR data, $E(x,t)$, are analyzed for each frequency component, $\hat{E}(x,f)$, by:

$$\hat{E}(x,f) = \int E(x,t) exp(-2\pi j f t) dt \tag{2-3}$$

which has an amplitude, $\left|\hat{E}\right|$, and phase component, φ. For a frequency component, f_i, with phase velocity v_i, the phase change, $\Delta\varphi$, as a function of the change in offset, Δx, is described as:

$$\Delta\varphi_i = -\frac{2\pi f_i}{v_i}\Delta x. \tag{2-4}$$

By correcting this phase change of the amplitude normalized electric field and summing over all offsets, the phase-velocity spectrum, $D(v,f)$, is obtained as:

$$D(v,f) = \left|\sum_x \frac{\hat{E}(x,f_i)}{|\hat{E}(x,f_i)|} exp\left(j\frac{2\pi f_i}{v_i}x\right)\right|. \tag{2-5}$$

The maximum spectral amplitude for a given frequency and dispersive mode defines the best estimate of phase velocity. Picking these points in the spectra produces the observed dispersion curves which can then be inverted to determine the waveguide properties. Depending on waveguide properties, the phase-velocity spectrum likely contains multiple modes of dispersion where the lowest frequency contained in each mode (m) of dispersion is determined by the cutoff frequency (f_c), which is a function of the thickness of the waveguide (h) and layer relative permittivities (ε_1 & ε_2):

$$f_c = \frac{[2\pi m + \phi(\theta_{12}^c)]c_0}{4\pi h\sqrt{\varepsilon_1 - \varepsilon_2}} \tag{2-6}$$

Below this cut-off frequency, there will be no solution for Eq. (2-1). Cutoff frequencies are associated with a wave that has a critical incident angle at the lower boundary and are manifested as discontinuities between modes in the frequency spectra.

2.3.3 Single Layer Approximations from Phase-Velocity Spectra

Phase-velocity spectra of dispersive GPR data show the relationship between EM wave frequency and phase velocity for specific modes of dispersion. As highlighted by *van der Kruk* [2006] and *van der Kruk et al.* [2006], specific parts of this data spectrum are sensitive to particular parameters of the dispersive waveguide. Specifically, *van der Kruk* [2006] shows that for a multi-modal dispersive waveguide, individual cutoff frequencies and layer permittivities can be approximated from the behavior of the amplitudes (dispersion curves) in this spectrum.

Figure 2.1a shows dispersive time domain data for the shock front case, which represents the extreme case of plug flow with no capillary influence. This model consists of an upper layer at a constant water content of 0.30 (vol. vol^{-1}.) and lower layer at a constant value of 0.10 (vol. $vol.^{-1}$), producing a sharp boundary similar to original simulations from *van der Kruk et al.* [2006]. It is important to note here that picking a single arrival at a given offset for the direct dispersed arrival would be difficult as there are multiple interfering reflections in the data. Note that the group velocity, i.e., the speed at which the envelope of the dispersed package of waves is moving through the waveguide (long solid black line), differs from the individual phase velocities (short dashed black lines), which indicates a frequency-dependent phase-velocity. These overlapping arrivals

in the data are characteristic of a dispersive wave and are similar to what *van der Kruk et al.* [2006, 2009a] termed a "shingling effect".

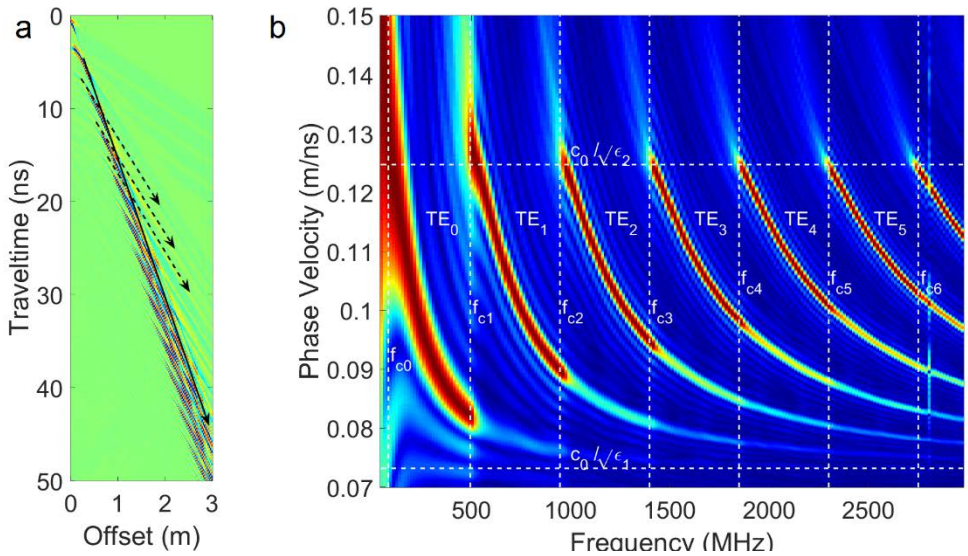

Figure 2.1 a) An example of dispersive time-domain data (shock front case), solid line indicates the group velocity and dashed lines indicate individual phase velocities; b) Phase velocity spectrum for the data presented in Fig. 1a showing the behavior of the dispersion curves in regards to the properties of the waveguide.

By applying the steps described in Section 3.3.2, we obtain the phase-velocity spectrum of the GPR data (Figure 2.1b). The upper and lower asymptotes of the dispersion curves represent the velocities of the lower halfspace and waveguide respectively. Furthermore, the beginning of these individual curves indicates the cutoff frequency of that specific mode. By manually picking the velocities and cutoff frequency values and combining them with Eq. 2-6, which has been solved for layer thickness (h), we can roughly estimate the thickness of the wetted zone acting as a low-velocity waveguide.

$$h = \frac{c_0[2\pi m + \phi(\theta_{12}^c)]}{4\pi f_c \sqrt{\varepsilon_1 - \varepsilon_2}} \tag{2-7}$$

2.3.4 Forward Model for a Dispersive Waveguide

Using the constraints from Eq. 2-2a and 2b to solve Eq. 2-1 for guided waves, a forward model can be generated that is suitable for inversion of dispersive data [*van der Kruk* 2006]. The model provides the phase velocity as a function of frequency (*f*), permittivity of the waveguide (ε_1), permittivity of the lower space (ε_2), and waveguide thickness (*h*):

$$v(f, \varepsilon_1, \varepsilon_2, h) = \frac{c_0}{\sqrt{\varepsilon_1}\sin[\theta(f, \varepsilon_1, \varepsilon_2, h)]} \tag{2-8}$$

2.3.5 Sensitivity of the Dispersion Curve

To test the sensitivity of the dispersion curve to changes in permittivity with depth, the dispersion forward model was run using 60 uniform layers, each of 0.01 m thickness. Initial values for the permittivity of each layer were set to the actual profiles derived from HYDRUS-1D [*Simunek and van Genuchten* 2005] simulations of flow in a homogenous soil. After the forward model was run to obtain a reference water content profile, each layer was perturbed successively by 10% of the mean of the profile and the dispersion curves were calculated. The impact of each layer perturbation was quantified using the misfit (*E*) of the curves generated by the true reference (*true*) and perturbed permittivity profiles (*pert*):

$$E = \frac{\sum_{i=1}^{nf_{true}} \frac{\left|v_{true}(f_i) - v_{pert}(f_i)\right|}{v_{true}(f_i)}}{nf_{pert}} \left[\frac{nf_{true}}{nf_{pert}}\right] \tag{2-9}$$

Here the phase velocities v_{true}, v_{pert} are a function of frequency f_i to define the true and perturbed dispersion curves, respectively. The misfit is normalized by the number of frequencies (*nf*) simulated given that the dispersion forward model will only generate phase velocity estimates for frequencies when Eq. 2-1 is satisfied. To generalize our findings to be independent of frequency, we chose to plot the results of this analysis using dimensionless depth, d^*, which is defined as:

$$d^* = \frac{depth}{wavelength} = depth\ \frac{frequency}{velocity} \tag{2-10}$$

While it may seem impossible to assume a single frequency and velocity in this study, it is reasonable to use the central frequency of the radar signal, 900 MHz, and an average velocity calculated from all the waveguides, which in this study is 0.0884 m ns^{-1}. This calculation gives us an average wavelength of 0.0983 m (note that the fractional term in Eq. 2-10 equates to the reciprocal of the radar signal wavelength). From Figure 2.2, we can see that there is no significant decrease in the misfit (Eq. 2-9) for permittivity perturbations beyond a dimensionless depth of 2, which correlates to an absolute depth of 0.20 m, i.e. roughly twice the radar wavelength. Therefore, we can assume that attempts to constrain the profile beyond this depth would be unrewarding given that the data will not sensitive to this part of the profile. Note that at the most sensitive depth, $d^* = 0.25$, a perturbation of 10% from the mean equates to nearly 1% deviation in the misfit (Eq. 2-9) when compared to the actual profile. This depth correlates well with what GPR practitioners would expect to be the resolution of the radar signal.

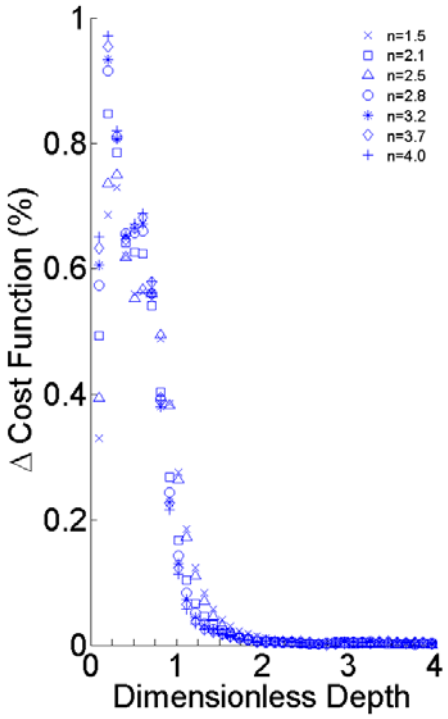

Figure 2.2 Results of sensitivity analysis that show the forward model is not sensitive to changes in permittivity beyond a depth of roughly twice the signal wavelength for all profiles considered.

2.4 Methods

To test our hypothesis that dispersion will decrease as capillarity increases, we ran multiple transient simulations, successively changing the *n*-parameter of the Mualem-van Genuchten soil model in the range of 1.5 – 4.0 for each simulation. The Mualem-van Genuchten soil model is commonly used to describe the water retention curve (i.e., relationship between pressure and water content) and relative permeability curve (i.e., relationship between hydraulic conductivity and water content) for a soil (van Genuchten, 1980). This relationship is described using five parameters: residual water content (θ_r),

saturated water content (θ_s), saturated hydraulic conductivity (K_s), and two shape parameters (α and n). While the parameters of the Mualem-van Genuchten soil model are not independent, we chose to solely vary the *n*-parameter [*Carsel and Parrish* 1998], which is related to the pore size distribution, because it has the largest effect on the sharpness of the infiltrating wetting front. However, we acknowledge that other parameters of the Mualem-van Genuchten soil model will likely have an effect on the dispersion of GPR waves in field settings.

In addition to the shock front model shown in Figure 2.1, and the variable *n* simulation results from HYDRUS-1D, we also used a homogeneous model where the water content profile is constant at 0.20 (vol. vol^{-1}) for the entire soil column. For all HYDRUS-1D simulation results, we chose to perform the dispersion analysis for a time during the infiltration event when the soil moisture profile produced a maximum reflection coefficient at 0.10 m depth. Given our radar frequency of 900MHz, we expect this thickness to produce a dispersive waveguide as the wavelength is comparable to the waveguide thickness. Two inversions were performed for each simulation: i) the waveguide represented as two constant permittivity layers, and ii) the waveguide represented by a piece-wise linear function.

2.4.1 Hydrologic Modeling and Simulations

The hydrologic simulations were performed using HYDRUS-1D [*Simunek and van Genuchten* 2005]. A depth of 0.6 m was chosen for the model domain, which was discretized into 601 uniformly sized cells (thickness=$1x10^{-3}$ m). A constant flux condition

was applied at the upper boundary of the soil column and a seepage face condition applied at the lower boundary. Mualem-van Genuchten parameters used in the simulations, with the exception of the variable *n*-parameter, are given in Table 2-1. To reduce the influence of initial conditions for each model, all simulations were run for a 20 year spin-up time period with the upper boundary flux set to zero and the initial conditions set to a uniform water content of 0.30. After equilibrium conditions were reached, the models were run with the upper flux set to 0.0044 m min^{-1} for 20 minutes time.

Table 2-1: Mualem-van Genuchten parameters for the HYDRUS-1D forward model from *Mangel et al.* [2012].

Residual Water Content θ_r [vol vol^{-1}]	Saturated Water Content θ_s [vol vol^{-1}]	Air-entry parameter A [cm^{-1}]	Shape Parameter [-]	Saturated Hydraulic Conductivity [cm min^{-1}]
0.04	0.35	0.045	Varied	2.8

2.4.2 Ground-Penetrating Radar Modeling and Simulations

Given that we are focused here on how soil capillarity affects the trends of waveguide dispersion in 1D flow systems, we chose to use the 2D finite difference time domain GPR forward model authored by *Irving and Knight* [2006]. We acknowledge, however, that the absolute amplitudes of the GPR signal would differ from that in our simulations due to 3D effects. The model domain (0.7 m x 4.0 m) for radar simulations was set up to collect data at large offsets so the critical angle for the waveguide would be reached. The domain was discretized into cells with Δx = 0.002 m and Δz = 0.001 m.

Magnetic permeability (μ) was set to a constant value of μ_0=1.256 x 10^{-6} H m^{-1} for the entire domain while electrical conductivity (σ) was set to constant values of 1 mS m^{-1} and 0 mS m^{-1} for the media and air, respectively. Note that the phase-velocity spectrum is obtained by only using the phase (see Eq. 2-2b) such that amplitude changes due to different conductivity values do not influence the results; simulations that used an order of magnitude increase in electrical conductivity of the waveguide showed no significant difference in dispersive behavior (results not shown). Therefore, we chose to fix these properties (σ and μ) to focus on the dominant effect of the dielectric permittivity profiles. Water content profiles simulated using HYDRUS-1D were converted to dielectric permittivity (ε) values using the Topp Equation [*Topp et al.* 1980] and replicated laterally for the GPR simulation. The 900 MHz source for the simulation was located at x = 0.5 m and z = 0 m with receivers placed every 0.025 m from x = 0.5-3.5 m. Perfectly matched layer (PML) absorbing boundaries were placed around the perimeter of the model domain to eliminate reflections from the edges of the domain. Simulations were run for a 60 ns time window. Note that the upper 0.1 m of the model domain is reserved for the air to generate the air/soil interface.

2.4.3 Inversion of the Dispersion Curves for a Two-Layer Model

To invert the dispersive GPR data and obtain properties of the low-velocity waveguide, a cost function was developed to compare the measured dispersion curves from simulations, v_{data}, to the modeled dispersion curve, v_{mod}, from a two layer forward model that utilizes the fundamental (TE0) and first (TE1) modes of the dispersive GPR data. We

investigate the two layer inversion approach here as it represents the current state of the art for resolving waveguide properties from dispersive GPR data (van der Kruk et al., 2010). The parameters for the forward model are the relative permittivity of each layer of the waveguide and the lower halfspace ($\varepsilon_1, \varepsilon_2, \varepsilon_3$) as well as the thicknesses of the two layers describing the waveguide (h_1, h_2). The cost function for the inversion is:

$$C(\varepsilon_1, \varepsilon_2, \varepsilon_3, h_1, h_2) = \frac{\sum_{i=1}^{nf_{data}} \frac{|v_{data}(f_i) - v_{mod}(f_i, param)|}{v_{data(fi)}}}{nf_{mod}} \left[\frac{nf_{data}}{nf_{mod}}\right] \quad (2\text{-}11)$$

Where f_i are the individual frequencies used in the inversion, nf_{mod} is the total number of frequencies considered in the inversion (i.e., dispersion forward model), and nf_{data} is the total number of frequencies available in the data (i.e., picked dispersion curves from simulations). The cost function effectively uses a normalized L1 norm for the data misfit and a model norm that penalizes the inversion for generating models with fewer frequencies than the data.

For the two layer inversions, we employ the method outlined in van der Kruk et al. (2010) which is a multiple starting model method that evaluates the cost function for multiple values of the independent variables in a global grid search. To limit the global search to feasible parameters, prior information extracted from the phase-velocity spectrum was used to bound the parameter space and increase the likelihood of finding a global minimum [*van der Kruk* 2006]. From the global search results, the top performing models, limited to a maximum of 30, are passed to a local simplex search [*Lagarias et al.* 1998],

obtaining multiple local minima. From these local minima, the best fit model is chosen on the criteria of the lowest cost function value.

2.4.4 Inversion of Dispersion Curves for Multi-Layer Piece-Wise Linear Model

In order to better represent the distribution of water in the subsurface we also investigated the case where a piece-wise linear function is used to represent the permittivity profile.

2.4.5 Parameterization of the Piece-Wise Model

To determine how many linear segments of the piece-wise function are needed to represent the upper 0.2 m of the profile, we ran the dispersion curve forward model multiple times, successively adding a linear segment to the representation of this section. Segment lengths were forced to be equal to avoid uneven weighting of specific sections of the profile. We also compared the performance of the piece-wise linear model to a layer model for capturing the dispersion response of the non-uniform water content profiles.

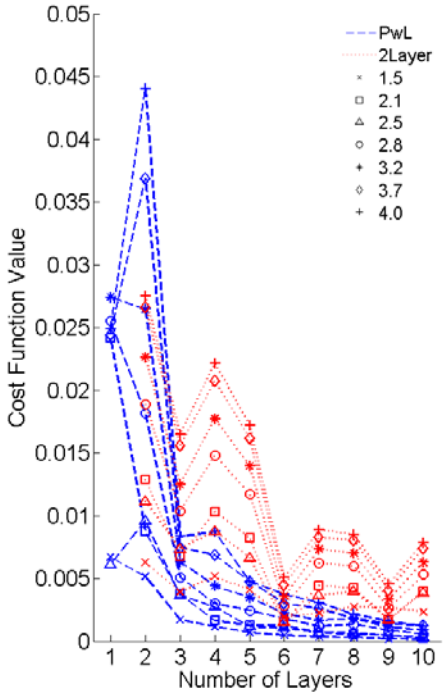

Figure 2.3**:** Parameterization tests show that if the upper 0.2 m is divided into 5 evenly spaced layers (*dz* = 0.04 m), the piece-wise linear function outperforms the two-layer model with the same layers in representing the dispersive data.

Figure 2.3shows the misfit of both models (Eq. 2-9) as a function of the number of segments used to represent the waveguide. For nearly all parameterizations of the waveguide, the dispersion curve generated using the piece-wise linear function matches the data significantly better. We therefore suggesting that a piece-wise linear function can better represent dispersive data associated with waveguides generated from infiltration events. Furthermore, given that using more than 5 linear segments does not lead to a

substantial reduction in the misfit, we use this geometry for the inversions performed in this study.

It is worth noting here that adjustments to the location of the boundaries in the layer model showed a substantial improvement in the misfit of the dispersion curves, illustrating the sensitivity of the layer geometry. For a given number of layers in the layer model or segments in the piece-wise linear forward model, however, the piece-wise linear model better represents the dispersion curve. Note that while this parameterization assessment used fixed layer thicknesses, the two-layer inversion outlined in Section 3.4.3 searches for optimal values for individual layer thickness (h_1 and h_2).

2.4.6 Inversion of the Data using Shuffled Complex Evolution

Given the increased number of parameters for the piece-wise linear model, the global grid search used for the two-layer model is no longer feasible. Shuffled complex evolution (SCE) [*Duan et al.* 1993] is a well-established optimization algorithm that has been used in multi-parameter hydrologic and geophysical problems [*Yapo et al.* 1998; *Mertens et al.* 2004; *Busch et al.* 2013; *von Hebel et al.* 2014] as well as other optimization research. The SCE algorithm uses a combination of probabilistic and deterministic approaches to move clusters of points spanning the parameter space toward a global minimum using competitive evolution between the clusters (see *Duan et al.,* [1993] for details). The starting model for individual SCE searches was determined using the approximation method outlined in Section 3.3.3. The range for each piece-wise linear model parameter was constrained by using the extreme values obtained by fitting all

simulated profiles, dispersive and non-dispersive, with the 5 layer piece-wise linear function (Section 3.4.1). We chose to use 10 complexes to explore the 10 dimensional parameter space and set the convergence criteria to a change of less than 5% in the best cost function value in 20 consecutive evolution loops.

In order to preserve the smooth nature of the water content profiles during the SCE search, we added a smoothness term to the cost function (Eq. 2-11). The smoothness value, *s*, of all simulated permittivity profiles was calculated using the normalized sum of the squared second derivative of the permittivity profile (ε).

$$s = \frac{\sum\left(\frac{d^2(\varepsilon)}{dz^2}\right)^2}{N} \tag{2-12}$$

Where *z* is the depth coordinate and *N* is the number of points making up the profile. These profiles are from simulation times that were not used in the dispersion analysis, i.e., the same hydrologic parameters and fluxes at different simulation times. The average value of the smoothness parameter from all simulated profiles was calculated to be 0.0142 and used as a representative smoothness for the profiles.

$$C = \frac{\sum_{i=1}^{nf_{data}} \frac{|v_{data} - v_{mod}v(f_i, param)|}{v_{data}}}{nf_{model}} \left[\frac{nf_{data}}{nf_{model}}\right] + \sum(s - 0.0142)^2 \tag{2-13}$$

2.5 Results

Selected results from hydrologic simulations were used in a ground-penetrating radar simulation to generate dispersive data. These simulated data were then analyzed using the dispersion analysis outlined by *van der Kruk et al.* [2006] to obtain dispersion

curves for the simulated data. These dispersion curves were inverted using the methods outlined in Sections 3.4.3 and 3.4.4.

2.5.1 Hydrologic Simulation Results

Figure 2.4a shows the selected water content profiles from simulations in HYDRUS-1D where the *n*-parameter of the Mualem-van Genuchten soil model was varied. The maximum first derivative of the water content profile (Figure 2.4b) was found to correlate well with the maximum GPR reflection coefficient, however, the profiles are displayed using water content to emphasize the hydrology as the controlling factor. Furthermore, we can also expect dispersion to occur as this reflector at 0.10 m depth, i.e., the inferred thickness of the induced waveguide (*h*), is comparable to the wavelength of the incident GPR signal.

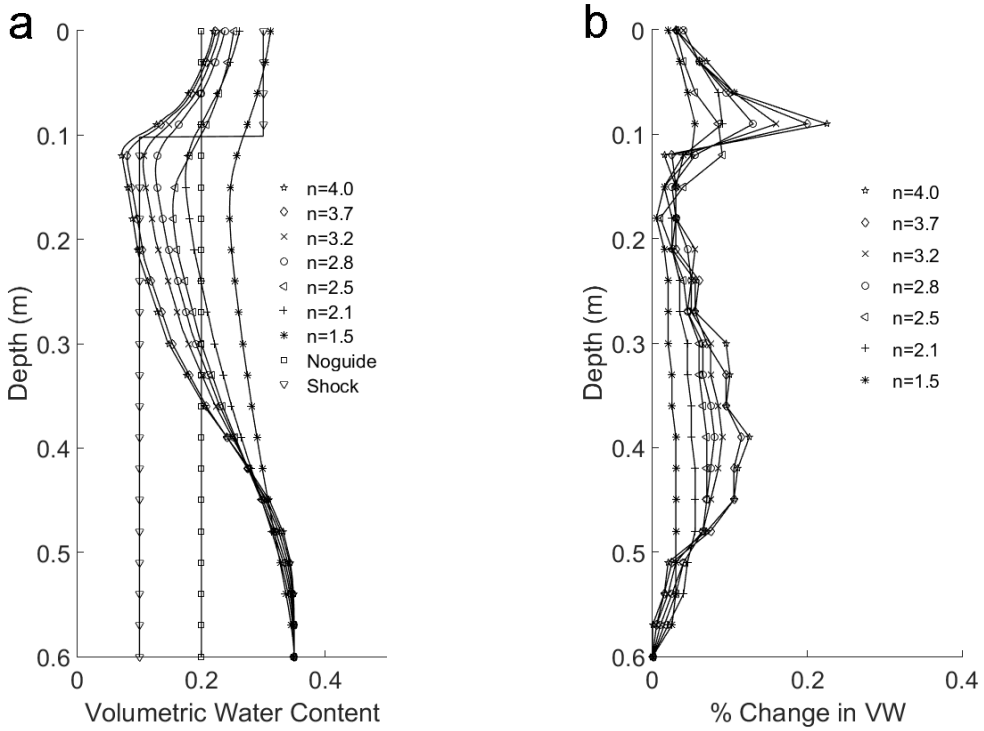

Figure 2.4**:** Effects on the water content profile by changing the *n*-parameter of the Mualem-van Genuchten soil model: a) Water content profiles for each simulation showing how the profile changes with capillarity. Note that high values of the Mualem-van Genuchten parameter '*n*' correspond with low values of capillarity; b) First derivative of water content profiles from Fig 4a as a percent gradient. Note how the sharpness of the water content profiles decreases significantly with increasing capillarity.

Visible in the hydrologic simulation results (n = 1.5 – 4) is the presence of an upper wetted region caused by the infiltrating water above 0.1 m depth (Figure 2.4a). Below this depth, the water content profiles resemble equilibrium conditions for their respective Mualem-van Genuchten parameters, ultimately reaching the saturated water content of 0.35 vol. vol.$^{-1}$. As n increases, i.e., the capillarity of the soil decreases, there is a significant decrease in the water content of the upper 0.10 m. Furthermore, as n increases, the

sharpness of the boundary between the wetted and background regions increases, raising the maximum first derivative, and therefore the reflection coefficient, at this depth (Figure 2.4b). As this contrast in the water content profile decreases, the conceptual model of a two-layer geometry, i.e., waveguide and lower halfspace, is increasingly less applicable.

2.5.2 GPR Simulation Results

Figure 2.5 shows the trace-normalized GPR simulation results for a range of capillarity values. Visible in all simulations are the airwave (A) and the groundwave (B) arrivals associated with the direct arrival of the GPR energy through the air and ground, respectively. In addition to these arrivals, Figure 2.5a–c show a unique characteristic described as 'shingling' (C) by *van der Kruk et al.* [2006], which is indicative of dispersion. Figure 2.5a shows the GPR simulation for the shock front case which has the largest amount of visible dispersion in the multi-offset section with the dispersion beginning to appear around 0.30 m offset. This shingling begins as a reflection observed at roughly 3 ns traveltime, followed by a series of multiples that interleave with each other. As the original reflection fades, the first multiple appears at 6 ns and becomes the dominant arrival. This continues as the energy bounces between the upper and lower interfaces of the waveguide creating the dispersion.

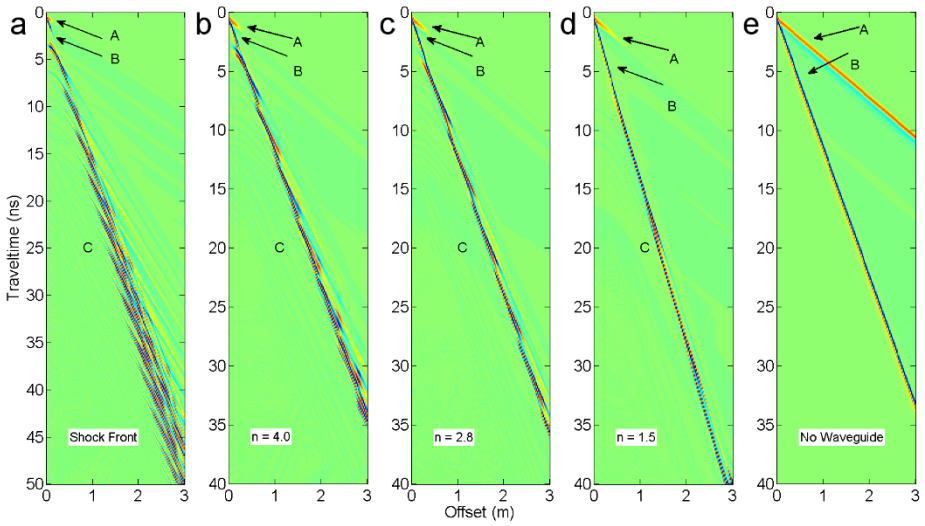

Figure 2.5**:** Trace normalized GPR simulation outputs for a) shock front case; b) *n* = 4.0; c) *n* = 2.8; d) *n* = 1.5; and e) no guide case. Arrivals are shown as follows: A – airwave, B – groundwave, C – shingled appearance indicative of dispersive waveguide.

A soil with minimal capillarity (i.e., *n* = 4.0) shows a similar pattern of dispersion (Figure 2.5b). However, the shingling is less prominent than the case of Figure 2.5a and does not begin to appear until an antenna offset of about 0.50 m. This illustrates that the contrast between the two layers is decreasing and a larger offset must be attained before the reflection coefficients in Eq. 2-1 reach unity, i.e., the critical distance must be attained between source/receiver pairs. Unprocessed simulated radar data (not shown) indicates the amplitude of the dispersed wave decreasing as the lower interface becomes more diffuse until no dispersion is visible when the waveguide is removed. This loss of amplitude of the dispersed wave is likely caused by the decrease in reflection coefficient as capillarity increases. While the shingling effect is a good visual indicator for the occurrence of

dispersion in raw multi-offset sections, dispersion analysis can provide a considerable amount of additional information.

2.5.3 Dispersion Modes vs. Capillarity

The GPR simulation results shown in Figure 2.5, as well as additional cases, were analyzed for dispersion as described in Section 3.3.2 to obtain phase-velocity spectra. Figure 2.6a shows the normalized phase-velocity spectrum for the shock front case. The red areas of the plot indicate the dominant phase velocity of a given frequency, i.e., the modal dispersion curve. Multiple dispersive modes (curves) are visible in the spectra with a new mode appearing for every 500 MHz increase in frequency. The discontinuity between curves is associated with the cutoff frequency for each mode of dispersion (Eq. 2-3 to 2-6). For the shock front case, velocity values range from 0.07 – 0.14 m ns^{-1} while the frequency ranges from 0 – 3000 MHz for the entire spectrum. The high number of dispersive modes indicates that there is a significant amount of energy being trapped in the waveguide by the upper and lower boundaries and that the critical angle is relatively small. These results show a similar pattern to those observed by *van der Kruk et al.* [2006] for idealized numerical simulations of layered media.

The spectra for the hydrologic simulations (Figure 2.6b-d) still show multiple modes of dispersion resulting from the precipitation induced waveguide. The number of dispersive modes present in each frequency spectra, however, decreases while each mode covers a larger range of frequencies as the lower wetted zone boundary becomes more diffuse (Figure 2.6c, d). Furthermore, the range of phase velocities decreases as soil

capillarity increases providing evidence of less dispersion as the phase velocities and group velocity converge to the same value. This is illustrated well in Figure 2.6e where no waveguide is present and the velocity range has collapsed to a singular value of 0.092 m ns^{-1} which is identical to the velocity input into the GPR model. Given that the thickness of the waveguide is constant, these observations are consistent with Eq. 2-6 which shows that for a given frequency bandwidth, the number of higher order modes increases with fixed waveguide thickness and increasing contrast between the waveguide and lower half-space permittivities [*van der Kruk* 2006]**.**

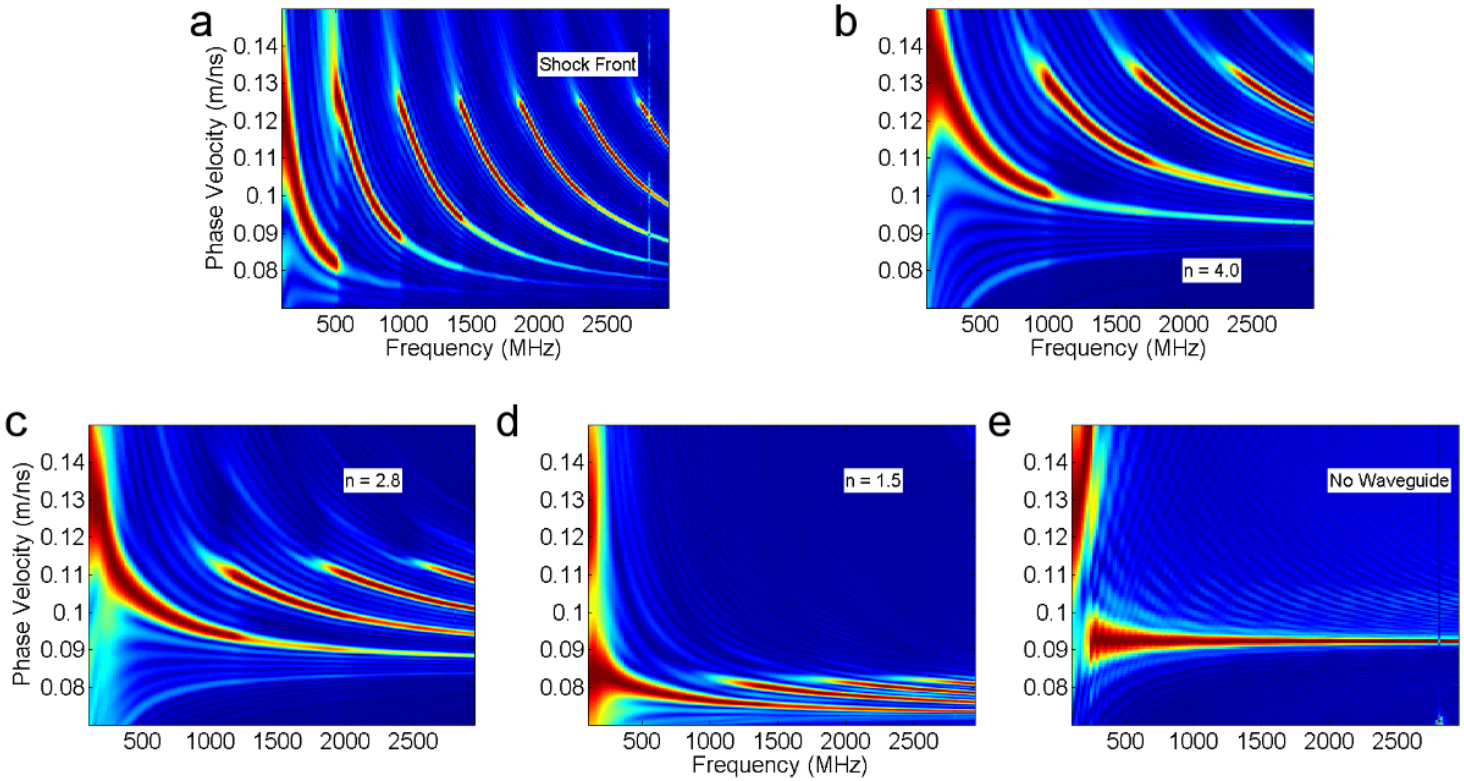

Figure 2.6**:** Normalized frequency spectra of the GPR simulation results for a) shock front; b) *n* = 4.0; c) *n* = 2.8; d) *n* = 1.5; and e) no waveguide.

The decrease in dispersive modes with increasing capillarity, i.e. decreasing *n*-value, is illustrated by the average frequency spectrum of selected simulations (Figure 2.7). The source wavelet of the GPR simulations has a clearly defined central frequency of 900 MHz. Transitioning from the most diffuse lower boundary of the waveguide, i.e., $n = 1.5$, to the extreme shock case there is a shift from a uni-modal frequency distribution to a multi-modal frequency distribution. The peaks of the multi-modal shock frequency distribution reflect the central frequency of each mode, while the troughs indicate the cutoff frequencies between modes (indicated with vertical lines for each *n*). This clearly demonstrates how the different modes present in the dispersed GPR data vary depending on the distribution of water within the dispersive waveguide.

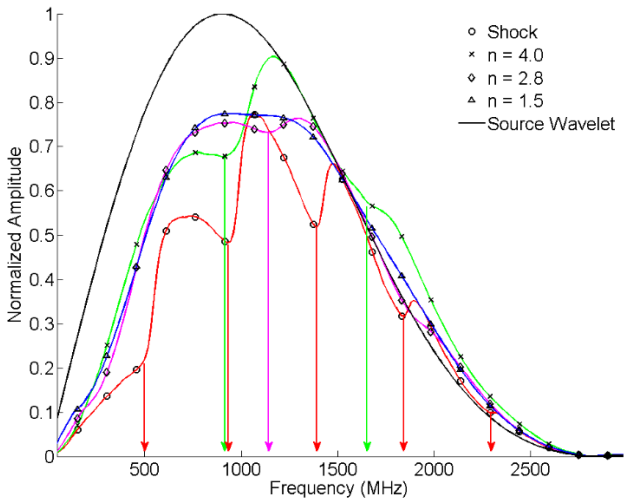

Figure 2.7**:** Average frequency spectra for selected GPR simulations illustrating the transition from a uni-modal frequency distribution (source wavelet) to multi-modal frequency distribution (shock front case). Vertical lines indicate interpreted cutoff frequencies for individual modes.

2.5.4 Inversion Results and Discussion

Dispersion curves were picked from the phase-velocity spectra (Figure 2.6) and inverted as discussed in section 3.4.3 and 3.4.4 to resolve water content profiles. Though inversions of single and multiple modes can be used [*van der Kruk* 2006; *van der Kruk et al.* 2010], we choose to focus on the joint inversion of the fundamental (TE0) and first order (TE1) dispersive modes (Figure 2.1) as these are present in all phase-velocity spectra (Figure 2.6) and higher order modes are not commonly available.

The data fit of the two parameterization methods along with the corresponding final cost function values are shown in Figure 2.8. To allow direct comparison of the data misfit, the smoothness term in the cost function for the piece-wise linear inversion (Eq. 2-13) was omitted. For all values of the soil's *n*-parameter, a very small misfit to the data is achieved, regardless of the choice of the model, i.e., piece-wise linear versus two-layer. Note that the cost function value is smallest, however, when using the piece-wise linear model, indicating that we are capturing more information that is relevant to the dispersion with this parameterization.

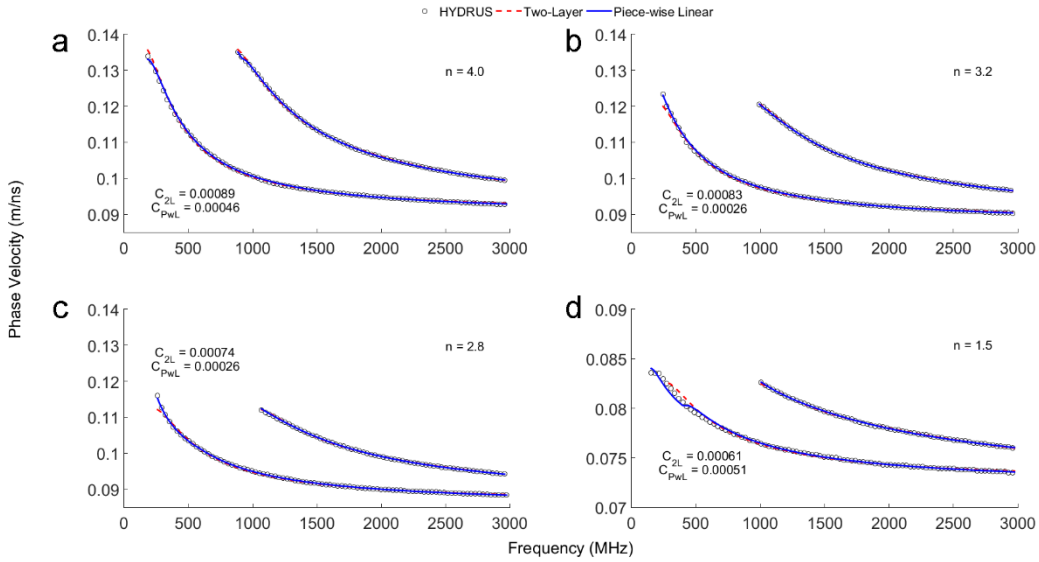

Figure 2.8**:** Data and inversion results for both inversion methods for a) *n* = 4.0; b) *n* = 3.2; c) *n* = 2.8; and d) *n* = 1.5. Cost function units are dimensionless.

The actual water content profiles from HYDRUS-1D are compared to the two-layer and piece-wise linear inversion results for selected values of the soil *n*-parameter in Figure 2.9. The profiles returned from the piece-wise linear inversion closely follow the actual water content depth profiles to 0.2 m. Below a depth of 0.2 m the piece-wise linear profile reflects the initial water content profile entered into the SCE algorithm. In contrast, the two-layer model's inherently blocky structure prevents it from capturing the detailed gradational nature of the water content change, though it does show net shifts in water content that are representative of the actual profile. The root mean squared error (RMSE) was calculated from 0-0.20 m depth to quantify the misfit of the water content profiles returned from both inversion approaches (Figure 2.9). Using a point by point assessment

of the misfit based on the node locations from the HYDRUS-1D model, the piece-wise linear model RMSE ($PwL_{allpoints}$) is substantially smaller than the two-layer model RMSE ($2Layer_{allpoints}$). In this case, we see a 50% reduction, on average, of the RMSE when using the piece-wise linear model. This illustrates that more information about the distribution of water within the waveguide is captured by utilizing a continuous piece-wise linear function compared to the blocky two-layer model.

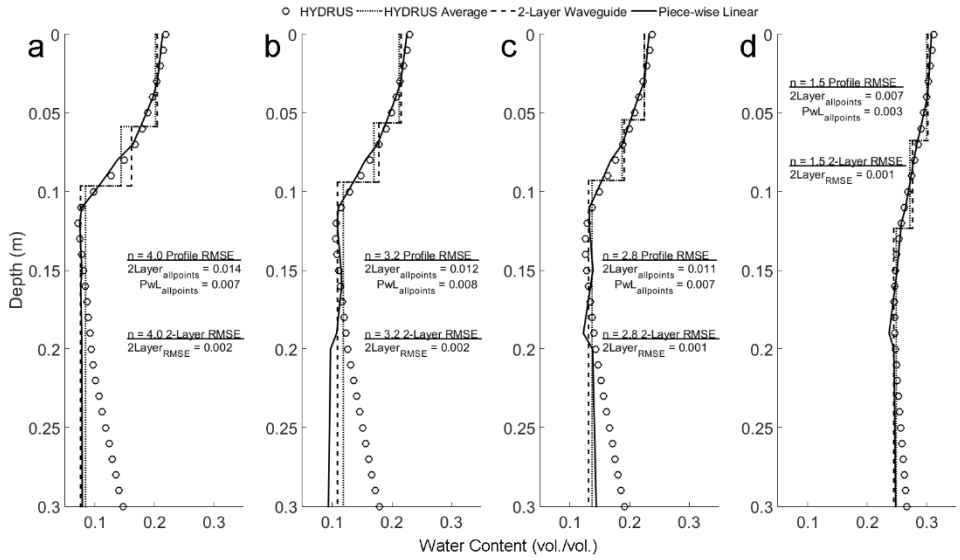

Figure 2.9**:** Results of two-layer and piece-wise inversions compared to actual and average water content profile from HYDRUS for a) *n* = 4.0; b) *n* = 3.2; c) *n* = 2.8; and d) *n* = 1.5. RMSE values are in water content, i.e. vol. vol^{-1}.

It is important to note, however, that interpretation of the two-layer model results should not, in general, be used to infer the water content at a specific point in the soil column, but rather represents an average or effective value over a discrete depth interval. For example, *van der Kruk et al.* [2010] previously demonstrated that the volumetric

average of the permittivities obtained from the two-layer inversion of dispersion data produces a similar result as that obtained from a single layer inversion.

In addition to the inversion results, we have therefore also plotted the average water content profile (HYDRUS Average in Figure 2.9), calculated by upscaling the actual water content profile obtained from HYDRUS-1D using the volumetric average over each depth interval returned by the two-layer inversion. From this we see that the two-layer model result is representative of the actual average water content for a given section of the profiles to a depth of 0.2 m. The fit is best for the first layer of the two-layer model and it degrades for deeper layers. The volume-weighted RMSEs between the two-layer inversion results and the up-scaled actual water content obtained from HYDRUS-1D are indicated by the $2Layer_{RMSE}$ in Figure 2.9. Note that these RMSE values should not be directly compared to the other RMSE values, as they were not calculated in a similar manner. The relatively small values obtained indicate, however, that the two-layer model closely describes the volumetric average of the water content over the specific depth interval of each layer, as noted by *van der Kruk et al.*, [2010].

The piece-wise linear model has shown the ability to capture significant information about the water content profile while maintaining versatility that would require substantially more parameters if a multi-layer model were used. While the two-layer models may be able to explain dispersion of GPR energy nearly as well, the geometry of the layers has a significant impact on the interpretation of the results as average properties. Perhaps more important, however, is that the 'blocky' profile of water content produced

by the layered medium model is far from what a hydrologist would expect to observe in the subsurface in response to infiltration, whereas the piece-wise linear parameterization results in physically-reasonable profiles. While there are many applications where average water content estimates are appropriate, there are also applications where it is important to accurately represent the depth distribution of water content. Significant value therefore rests in both of the model parameterizations, however, practitioners should be aware that they should select an appropriate model that suits the application.

2.6 Conclusions

Combined hydrologic and GPR forward modeling was used to test the hypothesis that dispersion would increase as the influence of capillarity in a porous media decreased. Capillarity of the porous media was controlled using the *n*-parameter of the Mualem-van Genuchten soil model. We observed that the dispersion of GPR waves varies with capillary effects given a precipitation induced dispersive waveguide controlled by hydrologic properties of the soil. We found that as the sharpness of the lower boundary of the dispersive waveguide decreases the number of dispersive modes in the GPR data decreases. Specifically, there is a clear difference in the dispersion of GPR waves when they encounter diffuse boundaries with a gradient of water content.

Given the sensitivity of dispersion data to the hydrologic characteristics of precipitation-induced dispersive waveguides, a revised parameterization of the forward model for the dispersion of GPR waves in a porous media was generated. Rather than represent the subsurface using layers, we utilized a piece-wise linear function which better

represents the gradational nature of the distribution of water within a waveguide. With this revised model, we were able to decrease the misfit between the dispersion data and the dispersion simulation which indicates that the piece-wise linear model incorporates more information about the distribution of water within a precipitation-induced waveguide. The misfit in the estimated water content distribution over the depth of the waveguide showed a 50% decrease, confirming that the piece-wise linear function outperforms the two-layer approach for fitting the full water content profile. We again stress, however, that the layered model is able to accurately capture depth-averaged water content values. Specifically the inversion results in this work: i) stress the importance of selecting a representative model for heterogeneity (e.g., layer versus piece-wise linear), ii) illuminate the implications of those models in a hydrologic context, and iii) show that dispersive GPR data contains substantial information regarding the distribution of water in dispersive waveguides.

Given these findings, we expect to have a reasonable amount of success in resolving hydrologic properties by coupling the dispersive forward model to a hydrologic forward model. Given that this was a strictly numerical study, further research is warranted to explore the effects of factors encountered when field data is considered, e.g. noise, heterogeneities, and signal attenuation. In conclusion, this study demonstrates that dispersive GPR data holds valuable information regarding the distribution of water in dispersive waveguides and shows promise for capturing the early-time dynamics of infiltration in homogeneous soils.

2.7 Acknowledgements

This material is based upon work supported by, or in part by, the US Army Research Office (W911NF-10-1-0365, W911NF-10-1-0292), and the National Science Foundation (EAR-1151294). We acknowledge the efforts of the associate editor (Niklas Linde) and three reviewers that improved the manuscript.

CHAPTER 3 - RESOLVING PRECIPITATION-INDUCED WATER CONTENT PROFILES BY INVERSION OF DISPERSIVE GPR DATA

3.1 Abstract

Automatically collected high-resolution GPR data were collected in common midpoint and common offset profile geometries before, during, and after a 24 minute forced infiltration event in a large sand tank. Data showed evidence of dispersion during early infiltration times (5-10 minutes), indicated by a shingled appearance of arrivals on trace-normalized common midpoint projections and a dependence between phase-velocity and frequency of the GPR signal. Dispersion curves were picked from selected profiles and inverted using a piece-wise linear function and a blocky layer model to resolve water content profiles of the infiltrating wetting front. Results from the inversions show good agreement with in-situ soil moisture measurements and a calibrated hydrological model. The piece-wise linear model, however, is able to honor the gradational nature of hydrologically induced waveguide phenomena and is in better agreement with observed soil moisture data. More work is needed, however, to quantify the effect of waveguide heterogeneity on the dispersion of the energy given that evidence of non-uniform water flow was observed in soil moisture probe data and interpreted common offset profiles. In conclusion, dispersive data holds substantial information about the distribution of water within the waveguide which may prove to be valuable for resolving important soil hydraulic properties through non-invasive automated time-lapse GPR imaging of infiltration processes.

3.2 Introduction

The strong relationship between electromagnetic wave velocity and volumetric water content in soils has allowed ground-penetrating radar (GPR) to become a valuable tool for studying subsurface variability [*Huisman et al.* 2003; *Topp et al.* 1980]. The fundamental dependence of GPR signals on water content makes this imaging tool particularly promising for non-invasive monitoring of hydrologic processes over multiple scales in time and space [*Busch et al.* 2013; *Grote et al.* 2005; *Lunt et al.* 2005; *Mangel et al.* 2012; *Mangel et al.* 2015a; *Moysey* 2010; *Steelman et al.* 2012; *Vellidis et al.* 1990]. Most surface-based imaging studies focus on using wave traveltime information to infer electromagnetic velocities, such as the normal moveout behavior illustrated for central mid-point (CMP) surveys in Figure 3.1a-c. Standard traveltime analyses are not possible early in an infiltration event, however, when the wetting front is near the ground surface and neither the direct groundwave nor reflected waves from a shallow wetting front can be readily identified in the data. Regardless, *van der Kruk et al.*, [2010] showed that the shallow wetted zone produced by a rainfall event may act as a waveguide that causes dispersion within the GPR data.

Electromagnetic wave dispersion occurs when individual frequency components, i.e., phases, within the GPR signal travel at different velocities [*Arcone* 1984; *van der Kruk* 2006; *van der Kruk et al.* 2006]. This phenomenon can be produced by a shallow, low-velocity waveguide that is less than the GPR wavelength in thickness such that reflection multiples interfere with each other and the direct groundwave to create a shingled

appearance in the data (Figure 3.1d-e). The frequency dependence of the wave velocity is readily described by dispersion curves in the phase-velocity spectrum (Figure 3.1f). The shape and number of dispersion curves, i.e. dispersive modes, that occurs is dependent upon the permittivity and thickness of the waveguide layer as well as the distribution of water within these layers [*Bakker et al.* 2011; *Mangel et al.* 2015b; *van der Kruk et al.* 2010].

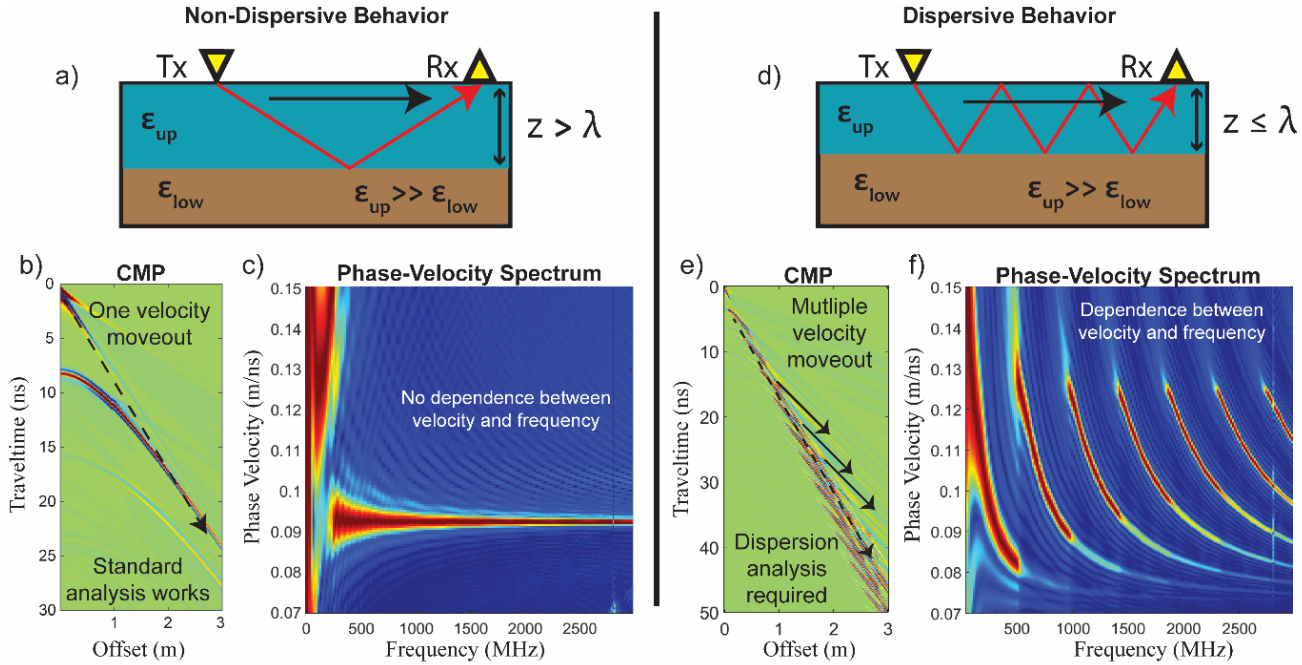

Figure 3.1: Differences between non-dispersive and dispersive behavior: a) conceptual model of non-dispersive behavior showing the separation of the groundwave (black solid line) and reflected raypaths (red solid line); b) simulated CMP data from (a) showing the moveout of the groundwave at a constant velocity (black dashed arrow); c) phase-velocity spectrum from data in (b); d) conceptual model of dispersive behavior showing interference between the reflected (red) and groundwave (black) raypaths; e) simulated CMP data from (d) showing group moveout (dashed black arrow) and individual phase moveouts (solid arrows); f) phase-velocity spectrum from data in (e).

van der Kruk et al. [2010] showed that the information captured within GPR dispersion curves can be used to estimate water content within a layered model of the subsurface, where the waveguide represents a zone of infiltrating water overlying an initially dry soil. A layer model is not necessarily the best representation of a wetting front, however, as the water content at the wetting front will vary with depth due to capillary effects [*Mangel et al.* 2015b]. *Mangel et al.* [2015b] used a numerical study to show that analysis of GPR dispersion data results in an estimate of water content that averages over the variability within each layer. Furthermore, these authors showed that dispersive GPR data contain sufficient information to constrain a piece-wise linear model for velocity variations with depth. This model was able to better reproduce the variability in water content associated with the wetting front compared to a two-layer model. The authors, however, only applied the analysis to idealized numerical simulation results. This work therefore extends the analysis to assess whether the method can be applied to real empirical data.

The objectives of this work are i) to evaluate the feasibility of a newly parameterized model that represents the waveguide layer using a piece-wise linear equation with empirical data, ii) to advance the understanding of the infiltration process, and iii) provide a non-invasive method for determining volumetric soil moisture content profiles.

3.3 Methods

In this manuscript we present the experimental methods and overview of the analysis techniques relevant to the specific experiment performed. The fundamentals of

waveguide dispersion and modal theory are given by *Arcone et al.* [2003] and *Mangel et al.* [2015b] provides details of the blocky layer and piece-wise linear models used in the inversions for this paper. Additional information regarding the application of dispersive GPR data in hydrogeophysical applications can be found in *van der Kruk* [2006], *van der Kruk et al.* [2006], and *van der Kruk et al.* [2010].

3.3.1 Data Collection

Infiltration experiments were performed in a large lysimeter (4 m x 4 m x 2m) constructed from wood and lined with a rubber mat for waterproofing that is partially filled with sand to a depth of 0.6 m (Figure 3.2). Irrigation sprayers were used to apply water at a constant, though not necessarily completely uniform, rate across the soil sand. Soil moisture probes were installed at multiple locations and depths in the irrigated area to log volumetric water content at 10 second intervals. Moisture probes were placed at the perimeter of the wetted area to minimize reflections from these objects in the GPR data.

GPR data were collected using a 1000 MHz bistatic radar coupled to an automated data collection system [*Mangel et al.* 2015a]. Data collection consisted of two common midpoint profiles (CMPs) along the y-direction followed by two constant offset profiles (COPs) collected in both the x and y directions. CMPs were collected at x = 2.0 m, y = 2.0 with offsets ranging from 0.17 – 2.17 m and trace spacing at 0.006 m; two CMPs were collected in each survey cycle as the antennas were spread apart with increasing offset (CMP1) and subsequently brought back together again (CMP2). Perpendicular COPs were collected in the y-direction at x = 2.0 and in the x-direction at y = 2.0. Offset was set to a

constant value of 0.17 m with trace spacing at 0.006 m. This data collection cycle [CMP, CMP COPx, COPy] took 30 seconds to complete, and was repeated 50 times during the 27 minute experiment for a total of 164,000 traces. Two cycles of data collection were completed prior to initiating irrigation of the surface of the sand at a constant flux rate of 0.003 m/min. The surface was irrigated for a total of 24 minutes during the experiment and ceased just before GPR data collection completed.

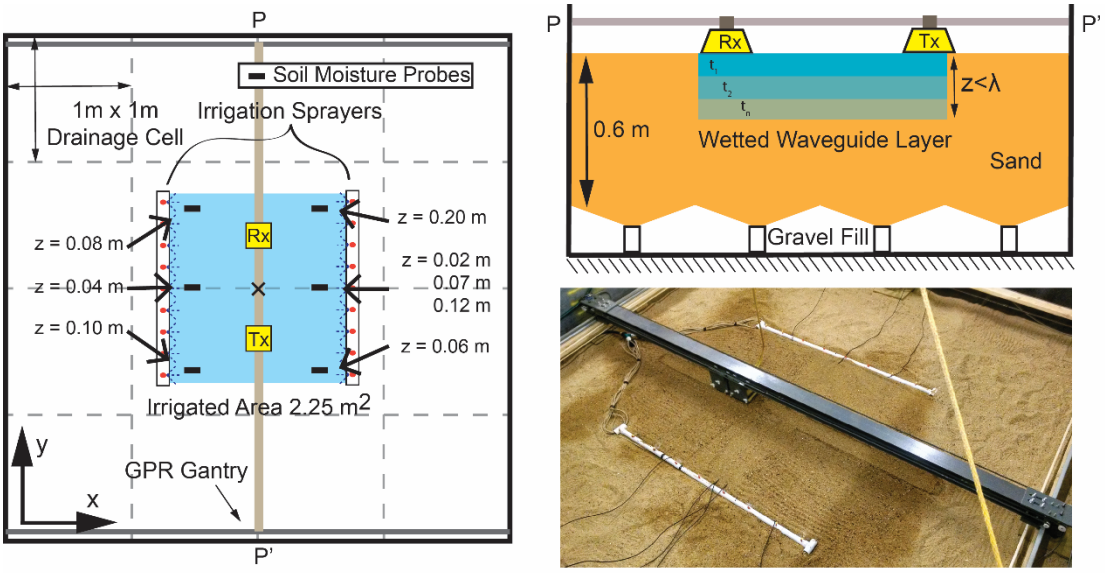

Figure 3.2: Experimental setup for the experiment.

3.3.2 HYDRUS Inversion

Data available from the soil moisture probes was used to invert for parameters of the Mualem-van Genuchten soil model, which is commonly used to describe the soil water retention curve [*Mualem* 1976; *van Genuchten* 1980], using HYDRUS-1D[*Simunek and van Genuchten* 2005]. Key parameters estimated include saturated water content, θ_s,

saturated hydraulic conductivity, K_s, and the two shape parameters, α, and n. Starting and final parameters from this inversion are listed in Table 3-1. Starting parameters were determined from lab-scale core experiments using a hanging column and constant head permeameter. Final parameters were used to forward model the hydrologic response, producing a 1D profile of the water content over time to compare with inversion results.

Table 3-1: Mualem-van Genuchten soil model parameters from inversion of the soil moisture data.

	θ_s [vol./vol.]	K_s [m/min]	α [1/m]	n [-]
Starting Value	0.38	0.046	5.8	4.6
Final Value	0.365	0.0123	6.8	3.72

3.3.3 Data Processing and Inversion Methods

Dispersive GPR data sets were selected for further analysis after plotting the trace normalized CMP data and evaluating the presence of dispersion, e.g. shingled arrivals. Given that these data likely occur near the beginning of the experiment, CMPs collected during the first 10 minutes were evaluated and processed using the Fourier transform to determine if there was a dependency between frequency and phase-velocity [*van der Kruk* 2006]. Dispersion curves were picked from the phase-velocity spectrum for CMPs that exhibit this behavior and used as data in the inversions for waveguide properties, i.e., the full GPR signal is not used in the inversion. In total, this provided 18 dispersive CMPs collected between 5-10 minutes after the start of the experiment. Inversions of the dispersion curves are performed using a single blocky layer and a piece-wise linear function to represent the waveguide layer.

For the single layer inversion, a global grid search followed by a simplex search of the top performing models is used to return a single effective layer value for the waveguide layer and lower halfspace.

$$C(\varepsilon_1, \varepsilon_2, z) = \frac{\sum_{i=1}^{nf_{data}} \frac{|v_{data}(f_i) - v_{mod}(f_i, \varepsilon_1, \varepsilon_2, z)|}{v_{data}(f_i)}}{nf_{mod}} \left[\frac{nf_{data}}{nf_{mod}}\right] \tag{3-1}$$

Where f is the frequency, $\varepsilon_1$and ε_2 are the permittivity for the waveguide and lower halfspace, respectively, z is the waveguide thickness, $v_{data}$and v_{mod} are the picked and modeled dispersion curves, and and nf_{data} and nf_{mod} are the number of frequencies available in the data and the modeled dispersion curves.

For the piece-wise linear inversion, the shuffled complex evolution (SCE) algorithm [*Duan et al.* 1993] is used to return parameters of a five-layer piece-wise linear function, as well as a regularization parameter, β, which controls the influence of the data fit versus the model fit. The piece-wise linear function is defined as:

$$f(z) = \begin{Bmatrix} m_1 z + b_1 & 0 \le z < 0.04 \\ m_2 z + b_2 & 0.04 \le z < 0.08 \\ m_3 z + b_3 & 0.08 \le z < 0.12 \\ m_4 z + b_4 & 0.12 \le z < 0.16 \\ m_5 z + b_5 & 0.16 \le z < 0.20 \end{Bmatrix} \tag{3-2}$$

This inversion uses the following cost function which utilizes an extra term to impose smoothness of the water content distribution in space:

$$C(f(z), \beta) = \frac{\sum_{i=1}^{nf_{data}} \frac{|v_{data} - v_{mod}(f_i, f(z))|}{v_{data}}}{nf_{mod}} \left[\frac{nf_{data}}{nf_{mod}}\right] + (s - 0.0142)^{\beta} \tag{3-3}$$

$$s = \frac{\Sigma\left(\frac{d^2(\varepsilon)}{dz^2}\right)^2}{N} \tag{3-4}$$

The smoothness constraint on the solution is defined as the squared error between the smoothness of the profile and an average smoothness value, 0.0142, calculated from multiple simulation results as the capillarity of the soil was varied [*Mangel et al.* 2015b]. Smoothness, *s*, is defined as the average squared second derivative taken over all the points, *N*, of the profile.

The workflow for these inversions attempts to minimize the amount of prior information used to determine waveguide properties. First, the single layer inversion is performed with the only constraint being that the waveguide layer have a higher permittivity than the lower halfspace. This is reasonable considering this is a fundamental physical feature that is required for dispersion to occur. Once the single layer inversion completes, the estimated parameters are used as a starting model to fit the piece-wise linear function. The SCE algorithm needs bounds for all parameters, which is not straightforward to obtain for the parameters of the piecewise linear function. The bounds for the piecewise linear function for water content in each layer were therefore determined from an ensemble of water content profiles generated by varying the n-parameter of the Mualem-van Genuchten soil model for multiple values in the range of 1.5-4.0 within HYDRUS1D. We solely varied this parameter due to the fact that it controls the capillarity of the soil, which effects the gradient of the water content profile between the wetted and non-wetted zones. Bounds for the regularization parameter were set at 1 and 1000, with the starting parameter set to 10.

3.4 Results

Although there is a wealth of hydrogeophysical information available in the data for this experiment, the focus of this paper revolves around analysis of the dispersive data sets, which were collected between 5-10 minutes after imaging began. We will quantitatively compare results from the inversion of dispersion curves derived from these data to measurements from in-situ soil moisture probes. Results obtained from the calibrated HYDRUS-1D model will be used to determine if our assumptions of a 1D profile are correct by qualitatively comparing the shape of dispersion curves generated by the HYDRUS model profiles to those from the data.

3.4.1 Soil Moisture Data

Data from the embedded soil moisture probes show changes in volumetric water content of the soil in response to a forced irrigation flux at the sand surface (Figure 3.3). As expected, the first response from a probe to the infiltrating water occurs at a depth of 0.02 m (lateral position: x=2.5m and y=2.0m). Two additional probes were buried at the same position, but 5 and 10 cm below the shallow probe (i.e., at depths of 0.07 and 0.12m from the surface). These probes respond sequentially in time as would be expected with a vertically migrating wetting front. If the infiltration front were spatially uniform, we would also expect the first response from other probes to respond sequentially with depth, regardless of their position. We observe, however, that the arrival of the wetting front occurs in the following depth sequence: 0.10, 0.04, 0.07, 0.08, 0.06, 0.12, and 0.20 m. The probes at a depth of 0.10 and 0.06 m are clearly out of sequence and indicate spatial

variability in the wetting front depth and, therefore, the thickness of the GPR waveguide. Both of these probes are located along one edge of the irrigated region (y=1.6m) and show opposite behaviors, i.e., the probe at 0.10m depths shows an early response, whereas the probe at 0.06m depth shows a late arrival of the wetting front (Figure 3.3c). This behavior may be related to application of a non-uniform flux at the edge of the wetted zone by the irrigation system, which has been observed during testing of the irrigation system.

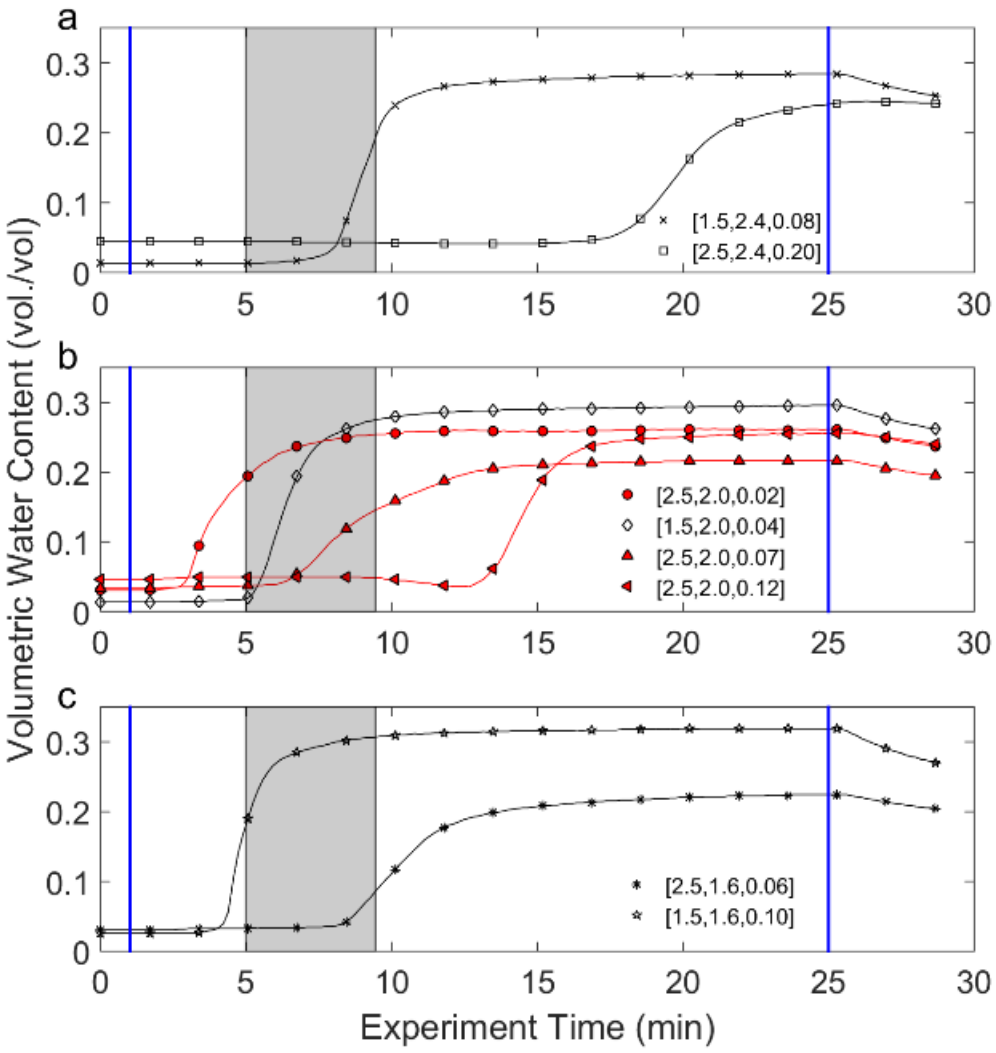

Figure 3.3: Volumetric water content measured at the in-situ moisture probe locations: a) probes located at y = 2.4 m; b) probes located at the CMP location, y = 2.0 m; c) probes located at y = 1.6 m. The legend reflects the [x, y, z] location of each moisture probe in meters. Vertical solid blue lines indicate the start and stop of irrigation. The grey area indicates the time when dispersion was detected in the CMP gathers.

3.4.2 GPR Data

Of the 100 CMPs collected during this experiment, 18 exhibited evidence of dispersive behavior. These data were selected knowing the general time when dispersion would occur, and by inspecting the CMPs for evidence of dispersion. All CMP data is de-wowed, time-zero corrected, and trace normalized before being analyzed for frequency content.

As water moves through the soil column, the GPR data change dramatically, showing evidence of dispersion between 5-10 minutes experiment time, i.e. about 4 minutes after irrigation begins (Figure 3.4). Prior to irrigation, the airwave (A), groundwave (G), and reflection (R) caused by the bottom of the sand layer at 0.60 m depth appear in the data (Figure 3.4a). After irrigation begins, evidence of dispersion is observed (high amplitude arrivals outlined by the thick dashed lines), making it difficult to identify the groundwave and bottom of sand reflection (Figure 3.4b). Controlling the overall moveout of the package of dispersed waves is the group velocity (thick black arrows), with individual arrivals moving out at different apparent phase velocities (thin dashed arrows) (Figure 3.4c-d). Once the waveguide layer is thicker than the wavelength of the GPR signal, evidence of dispersion is no longer present, however, arrivals other than the groundwave and airwave are still difficult to resolve (Figure 3.4e)

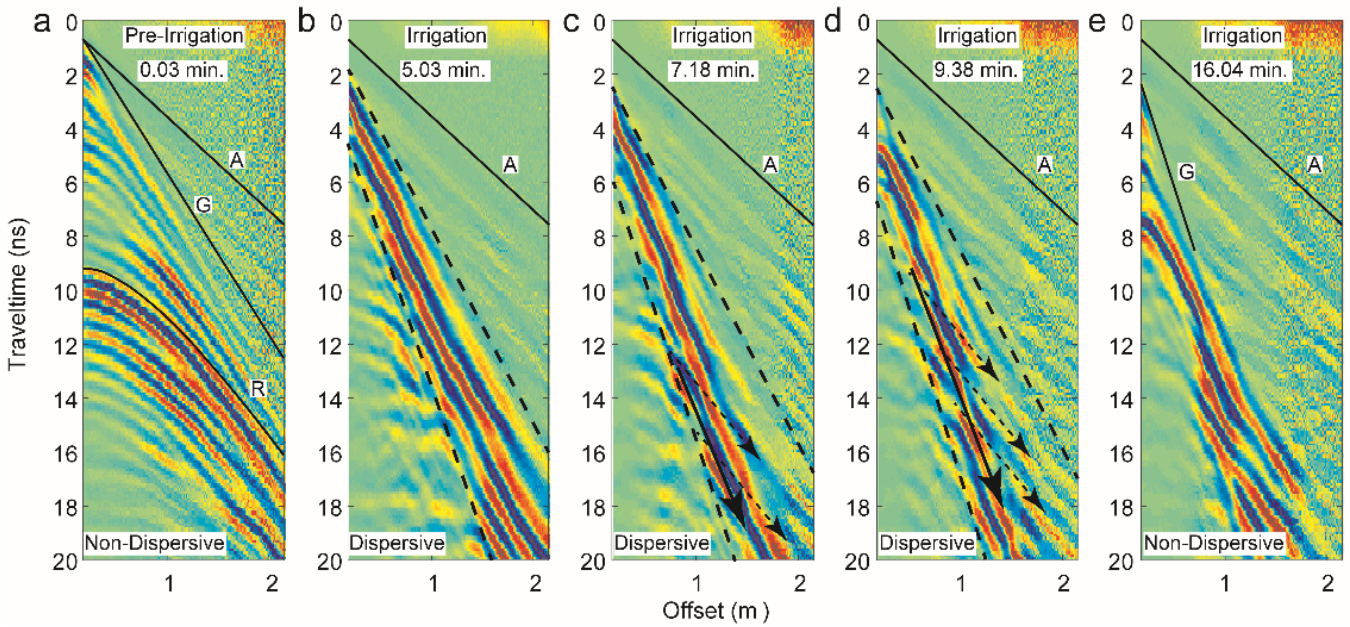

Figure 3.4: CMP data collected during the experiment: a) pre-irrigation initial conditions showing the (A) airwave, (G) groundwave, and (R) reflection arrivals; b – d) data collected during irrigation showing evidence of dispersion encased by dashed lines, the apparent group velocity moveout (solid arrow) and phase velocity moveouts (dashed arrows); e) return to non-dispersive conditions during irrigation.

3.4.3 Dispersion Analysis and Inversion Results

The phase-velocity spectrum was calculated for each of the dispersive CMPs by correcting the data for normal moveout and summing amplitudes over all offsets in the frequency domain for a range of velocity values. This analysis produces the phase-velocity spectrum that illustrates the dependence between phase velocity and frequency, allowing us to pick the dispersion curves for inversion (Figure 3.5).

The first, or fundamental, mode of dispersion was visible in all data sets, with higher order modes appearing as broken or discontinuous energy (Figure 3.5c). This indicates that the signal to noise ratio at large offsets was relatively low, also indicated by substantial noise in the data at large offsets (Figure 3.4). Forward modeling of the dispersion curves using profiles from HYDRUS-1D indicated that higher order curves should be present, however, they were not picked due to inconsistencies in the dispersion spectra. In an attempt to resolve the higher order modes, a limited offset range was used, but produced similar results for all curves. Additionally, inversion results from the multiple fundamental curves obtained by altering the offset range showed identical results for waveguide properties.

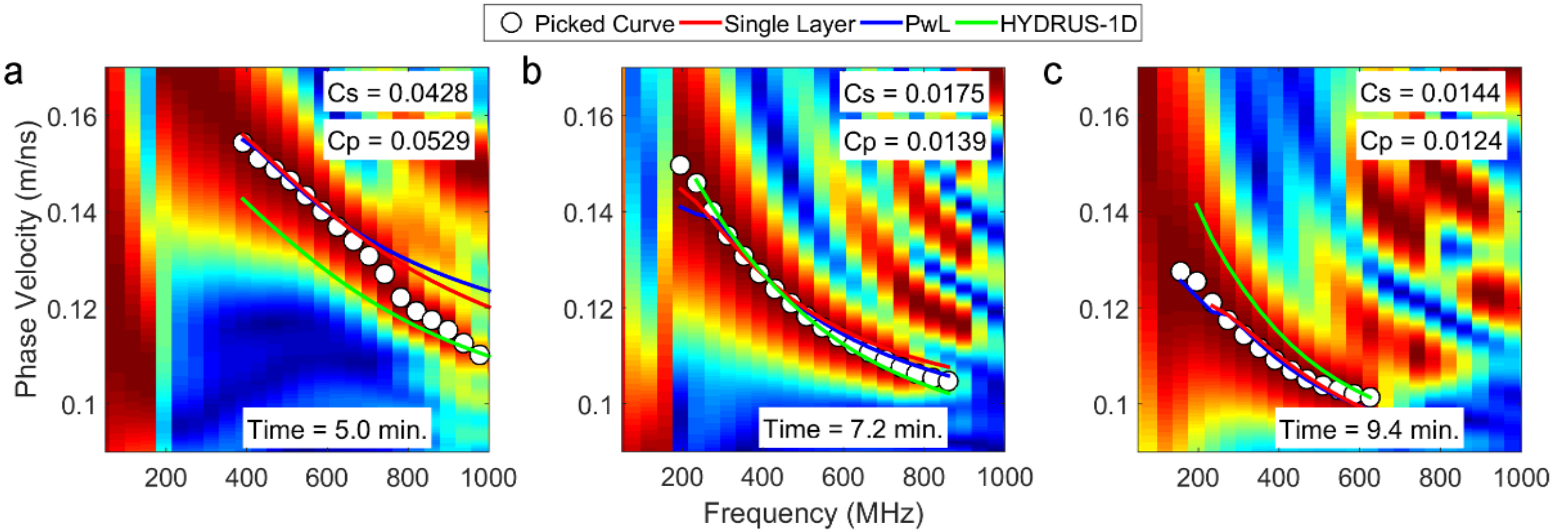

Figure 3.5: Phase velocity spectra and data fit of inversion results for dispersive data at a) 5.0 minutes; b) 7.2 minutes; and c) 9.4 mintues. Data misfit values for the inversions are plotted.

The first dispersion curve was picked for all phase velocity spectra and used to invert for waveguide properties in the single layer and piece-wise linear inversions. Calculating the data norm for both the single-layer and piece-wise linear methods (Eq. 3-3) shows that the data fit is comparable, as indicated by the similar cost function values given in Figure 3.5. The dispersion curve generated from forward modeling in HYDRUS-1D typically follows the trend of the dispersion curve, but is off in magnitude in some cases. While shifts in the dispersion curves likely related to the HYDRUS-1D model failing to accurately replicate the water content of the waveguide and the lower halfspace (Figure 3.5c), deviations in the shape of the data dispersion curves compared to the idealized HYDRUS-1D curves indicate increased noise in the data, possibly caused by a non-uniform waveguide (Figure 3.5a). Although both the HYDRUS-1D simulations and the dispersion analysis assume a 1D flow regime, water content profiles produced in the experiment do not necessarily honor those assumptions.

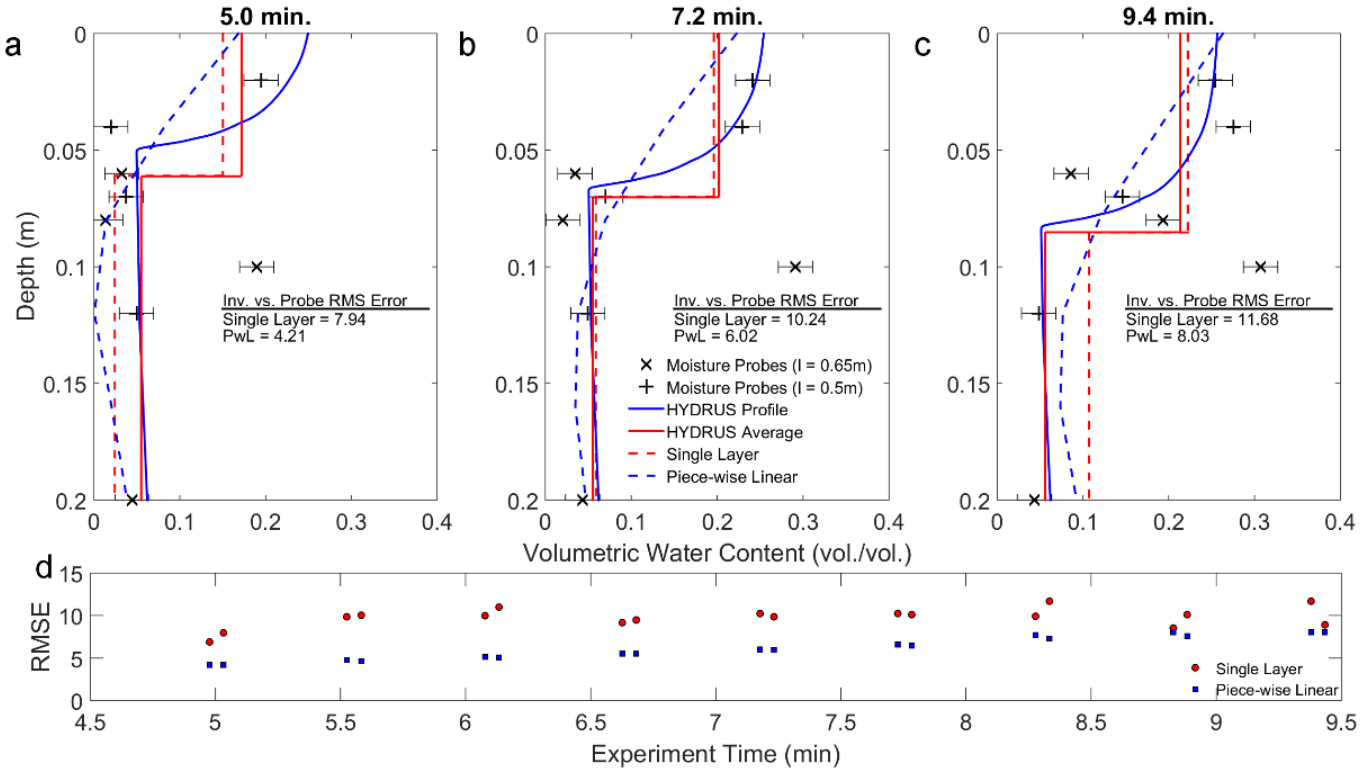

Figure 3.6: Results from dispersion curve inversion compared to probed data and HYDRUS inversion results at a) 5.0 minutes; b) 7.2 minutes; and c) 9.4 minutes experiment time; d) RMS error between probes and inversion results for all dispersive data. Readings from moisture probes are plotted using depth of the probe and Pythagorean distance (l) from the CMP location.

Posterior models for the waveguide layer from both inversion methods are in fair agreement with measurements from in-situ soil moisture probes and show a thicker and wetter waveguide layer over time, which is consistent with time-dependent spatial patterns of 1D infiltration, even though the inversions were not constrained in time (Figure 3.6). In general, the response from the soil moisture probes is relatively heterogeneous when compared to the dispersion inversion results, especially considering the probe at 0.10 m depth, which responded out of sequence to the infiltrating water (Figure 3.3c). Noisy probe measurements should be expected when compared to the dispersion inversions, however, considering the small sample volume of the probes (< 1L) compared to the GPR.

From root mean squared error (RMSE) calculations, the piece-wise linear inversion returns a consistently better fit to the probe data (Figure 3.6d). To calculate the RMSE between the dispersion inversion results and the probes, the soil moisture probe at 0.10 m depth was ignored. For the single layer inversion, probe measurements above and below the waveguide depth returned by the inversion were averaged together. This enables the point measurements from the probes to be compared to the average soil moisture values returned by the single layer inversion. Soil moisture probes were compared directly to the piece-wise linear function, considering that it is a continuous function. The results of the layer inversion, however, are in excellent agreement with average soil moisture from the HYDRUS-1D model taken over the same interval, indicating that the single layer model is performing as expected and returning a reliable effective layer value and potentially less susceptible to noise in the data. The misfit between the piece-wise linear model and the

HYDRUS1D results, however, indicates that this method may be more susceptible to noise in the data potentially caused by non-uniform flow.

If all results from the 18 CMPs analyzed are considered, however, we can see that the layer inversion seems less stable in time, with fluctuating thicknesses of the waveguide layer that are inconsistent with time-dependent spatial patterns expected during infiltration (Figure 3.7a). Although the layer inversion results reflect an overall trend of an increasing waveguide thickness, the piece-wise linear inversion results appear to be more stable in time, with the exception of three profiles at 8, 8.5, and 9 minutes (Figure 3.7b). Additionally, the piece-wise linear inversion results return consistent profiles for CMPs collected at short time intervals; a pattern that arises from the data collection pattern [CMP, CMP, COPx, COPy] with short time gaps between two CMPs, followed by a longer period in which the common-offset data were collected. (Figure 3.7b-c). Most importantly, the piece-wise linear results reflect a much more diffuse boundary between the wetted and non-wetted layers, which is in good agreement with the HYDRUS-1D results (Figure 3.7c). Both inversion methods return a few erratic profiles after 8 minutes, however, no spikes in the data norms for these inversions are observed. This may indicate that dispersive conditions are waning, considering that the probes at 0.07 and 0.10 m depth show increases in water content at this time. Note that for 1000 MHz antenna, dispersion will not occur once the waveguide reaches 0.10m depth.

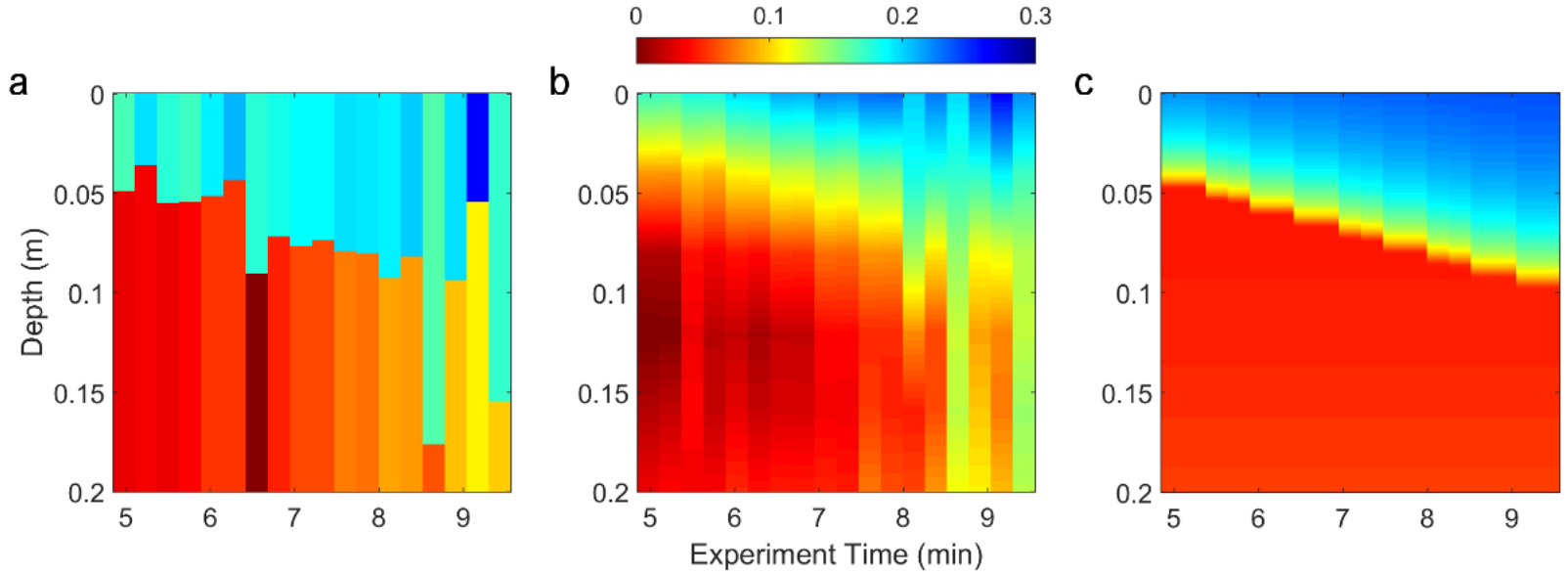

Figure 3.7: Results from inversion of all dispersive CMP data using: a) the single layer inversion and b) the piece-wise linear inversion. The results from c) the HYDRUS 1D simulation are included for comparison.

3.5 Discussion

Data quality for the inversion may be impacted by heterogeneities in the waveguide layer caused by non-uniform flow of water through the soil column. This was evident in the soil moisture probe data with deeper probes measuring increases in water content prior to shallower probes. Additionally, evidence of heterogeneity is observed in GPR reflection images (i.e., COPs) by interpreting the data through time as the only changes are caused by the infiltration of water (Figure 3.8).

Prior to irrigation, the data show that the groundwave (G) and bottom of sand reflection (R) are relatively flat, indicating homogenous water content across the profile (Figure 3.8a). During irrigation of the sand surface at 5.4 minutes into the experiment, however, the data show a substantially heterogeneous response with undulations in the groundwave (G) and wetting front reflection (W) (Figure 3.8b). Given that the data are not migrated, this could potentially be explained by lateral variations in velocity. Legs of diffraction hyperbolas (D) are also visible in the data indicating the existence of small scale heterogeneities at the interface between the wetted and non-wetted layers which are scattering the GPR energy (Figure 3.8b). The non-uniform flow is evident in a later COP as well (Figure 3.8c), where a large shift in the traveltime of the wetting front reflection (W) is observed. This may be a contributing factor to noise in the data and therefore erratic results observed in the dispersion inversion results beyond 8 minutes (Figure 3.7).

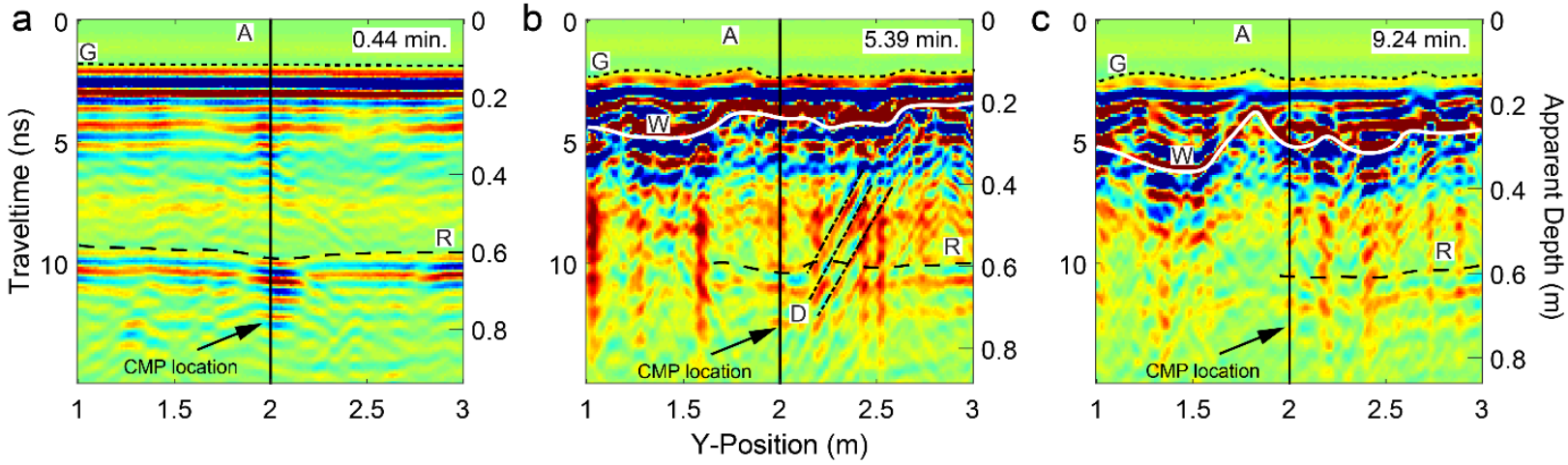

Figure 3.8: Common offset profiles from the GPR data showing evidence of non-uniform water flow through time at a) 0.44 minutes; b) 5.39 minutes; and c) 9.24 minutes. Arrivals annotated are the airwave (A), groundwave (G), bottom of sand reflection (R), wetting front reflection (W), and diffraction hyperbola legs (D).

Noise in the data likely effects the two methods for dispersion curve inversion in different ways. For example, the single layer inversion results are in excellent agreement with average profiles extracted from the results of the HYDRUS-1D profile. This indicates that the single layer inversion is less susceptible to the noise in the data and returns a profile representative of a 1D flow regime. However, the single layer inversion has substantially less flexibility in fitting realistic water content profiles that may not be 1D, evidenced by the increased RMSE for the single layer inversion in replicating the noisy probe measurements when compared to the piece-wise linear inversion (Figure 3.6d).

Lateral heterogeneity in waveguide layers is expected given the poorly understood mechanisms of preferential flow and general instability of unsaturated flow. Some work has been done to investigate the effect of waveguide heterogeneity on the inversion of dispersion curves, however, the study did not consider hydrologically derived waveguide layers [*van der Kruk et al.* 2012]. Although the study concluded that the effect of waveguide heterogeneity is relatively small, more work is required to validate this conclusion in a hydrologic framework. Regardless, both methods, when coupled with automated GPR data collection, show promise for revealing the early time dynamics of water content profiles associated with an infiltration event.

3.6 Conclusions

Electromagnetic waveguide dispersion of GPR energy is caused by shallow low-velocity layers which may arise from an infiltrating wetting front. Dispersive GPR data collected during an infiltration event into a homogeneous soil was inverted to obtain

waveguide properties using a blocky layer model and a piece-wise linear model, which had only been previously tested on idealized numerical data. Both inversion approaches returned good data fits, indicating that both methods can describe the dispersive behavior.

However, given that these waveguides are hydrologically derived, the piece-wise linear model is more representative of the underlying infiltration process, and showed improved agreement with data from in-situ soil moisture probes when compared to a single layer model. Additionally, the gradational nature of the water content distribution was well preserved when compared to the calibrated HYRDUS-1D model results. Notably, without the application of temporal constraints, the piece-wise linear inversion results were more consistent with the results of the calibrated HYDRUS-1D model through time, indicating a progressively thicker waveguide layer. The blocky layer inversion was also relatively successful in replicating measurements from soil moisture probes, although to a lesser degree. Single layer inversion results were generally in excellent agreement with average water content values derived from a calibrated HYDRUS-1D forward model, indicating that this method is less sensitive to noise in the data that may be generated by non-uniform flow.

In conclusion, the piece-wise linear inversion was successfully applied to empirical data, and shows promise in honoring characteristics of hydrologically derived dispersive waveguides. Further work is necessary to determine the impact of waveguide heterogeneity on dispersion curve inversion, however, both inversion methods remain as unique approaches for revealing the early time dynamics of infiltration events. Also worth

noting is that the temporal resolution of the data could not be obtained without the automation of the GPR data collection, which enabled the ability to study the highly dynamic infiltration process.

3.7Acknowledgements

This material is based upon work supported by, or in party by, the National Science Foundation under grant number EAR-1151294. We would also like to acknowledge Clemson University for generous allotment of compute time on Palmetto cluster.

CHAPTER 4 - RESOLVING SPATIOTEMPORAL WETTING PATTERNS FROM DYNAMIC HYDROLOGIC EVENTS WITH GPR REFLECTION TOMOGRAPHY IN HOMOGENEOUS SOIL

4.1 Abstract

GPR is evaluated as a tool for providing information regarding transient soil moisture measurements in 2D using reflection tomography in the post-migrated domain. GPR data, as well as numerical simulation results are evaluated using the reflection tomography algorithm and compared to true water content values. Tomography results from the simulated data set are in good agreement with true water content distributions from simulations with errors typically falling between 5-10% vol./vol. Water content distributions produced by the tomography of the empirical data sets are in good agreement with in-situ soil measurements, with similar errors observed to those in the numerical study. Additionally, water content distributions from tomography of the data reveal a heterogeneous flow pattern which allowed for the re-conceptualization of the wetting front geometry. Overall, the automation of GPR data collection is paramount to monitoring dynamic hydrologic events and enables higher-order data analysis algorithms, like reflection tomography, that show promise in estimating unprecedented information regarding the 2D spatial distribution of water content through time independent of ancillary information typically considered in geophysical data inversion.

4.2 Introduction

Surface-based hydrologic monitoring with ground-penetrating radar (GPR) is capable of producing rich hydrogeophysical data sets at multiple scales in time and space [*Buchner et al.* 2011; *Busch et al.* 2013; *Haarder et al.* 2011; *Lunt et al.* 2005; *Mangel et al.* 2012; *Moysey* 2010; *Steelman and Endres* 2010; *Vellidis et al.* 1990], largely due to the dependence of electromagnetic (EM) wave velocities on soil volumetric water content [*Topp et al.* 1980]. In particular, when deployed in a time-lapse fashion, studies have shown that GPR data can provide valuable information regarding dynamics, i.e. heterogeneities, of subsurface hydrologic processes [*Guo et al.* 2014; *Haarder et al.* 2011; *Mangel et al.* 2012; *Mangel et al.* 2015a; *Moysey* 2010; *Saintenoy et al.* 2007; *Steelman et al.* 2012]. Given the importance of infiltration in the critical zone to recharging important groundwater supplies [*Brantley et al.* 2006], time-lapse GPR is especially attractive, given that this process can be largely heterogeneous in time and space [*Flury et al.* 1994].

Often, analysis of GPR data for soil moisture estimation in these studies relies on *a priori* or ancillary information to resolve water content images as a function of space or time. This may include extra information such as depth to a reflector [*Lunt et al.* 2005] or the coupling of the analysis to a hydrologic model [*Busch et al.* 2013; *Rossi et al.* 2015]. This can be avoided in time-lapse studies, however, results are typically limited to only illustrating differential soil moisture shifts in space and time [*Truss et al.* 2007]. While these studies have profoundly advanced the field of hydrogeophysics and the use of GPR in monitoring soil moisture dynamics, they are susceptible to conceptual errors, hard

constraints imposed by the coupled model, and suffer from limitations introduced by assumptions.

Limitations introduced to time-lapse GPR studies, however, are commonly a result of operational limitations of commercially available equipment. This is why multi-offset data, which contains information about subsurface velocity structure, is typically collected at sparse locations and applied to high-resolution data collected using common-offset geometry, i.e. where the transmitting and receiving antennas are at a fixed distance apart and used to profile across the surface [*Neal* 2004]. The common-offset surveys are substantially easier to collect since the triggering can typically be controlled with an odometer wheel or GPS link and generally suffice for most GPR studies. Studying infiltration with time-lapse approaches, however, requires that the velocity be resolved at a much higher resolution to provide information about water content distributions using petrophysical relationships.

Bradford [2006], introduced reflection tomography in the post-migrated domain to GPR and showed the power of the algorithm in resolving highly heterogeneous velocity distributions at two field sites. *Bradford* [2008] further expanded on the application of the reflection tomography algorithm to GPR data, highlighting how it could be used to measure subsurface water content distributions. For infiltration, however, the time required to collect the data for the reflection tomography algorithm can be problematic considering the inherently dynamic and spatially heterogeneous nature of unsaturated flow [*Flury et al.* 1994; *Hendrickx and Flury* 2001; *Ritsema et al.* 1993]. Using automated data collection

approaches, however, the data required for reflection tomography can be collected on the order of minutes, and subsequently repeated immediately after at exactly the same points from the previous survey [*Mangel et al.* 2015a]. This enables the use of algorithms like reflection tomography for studying infiltration and has potential to expand geophysical monitoring of hydrologic processes to new horizons.

The authors are not aware of any previous applications of the reflection tomography algorithm in surface-based time-lapse GPR studies, and expect that this is largely due to the data that is required for the algorithm. Methods such as reflection tomography should be explored for these applications, however, considering that the algorithm solely relies on adjusting the velocity model to match the traveltime vs. offset relationship, i.e. the moveout, of arrivals on multi-offset GPR data [*Bradford* 2006; *Bradford* 2008; *Stork* 1992]. This separates the GPR data inversion from ancillary information or assumptions about how the velocity field is changing, giving the algorithm potential to inform important choices about how conceptual models are formulated.

Given that the novel approach to data acquisition presented by *Mangel et al.,* [2015] is enabling the application of the reflection tomography algorithm to an entirely new problem, the objective of this study is to evaluate reflection tomography of high-resolution GPR data as a tool for observing and characterizing unsaturated flow patterns during infiltration into a homogeneous soil. To evaluate the efficacy of the algorithm in resolving dynamic soil water content in 2D, we first test the algorithm using numerical simulations and compare the results to true water content distributions. The algorithm is also applied

to time-lapse GPR data collected during an infiltration and recovery event in a homogeneous soil and compared to measurements from in-situ soil moisture probes.

4.3 The Reflection Tomography Algorithm

Reflection tomography was originally developed to provide an analytical method for resolving velocity fields from seismic data, of which there are many approaches [*Bishop et al.* 1985; *Gardner et al.* 1974; *Yilmaz and Chambers* 1984]. Although the tomography algorithm was originally developed for use with seismic data sets, it can also be directly applied to GPR data if absolute amplitude reconstruction is not desired [*Bradford* 2006]. For brevity, we will discuss the key ideas and methods of the tomography algorithm, however, for a full description of the original tomography algorithm we refer the reader to *Stork* [1984] for the original development and *Bradford* [2006] for application to GPR data.

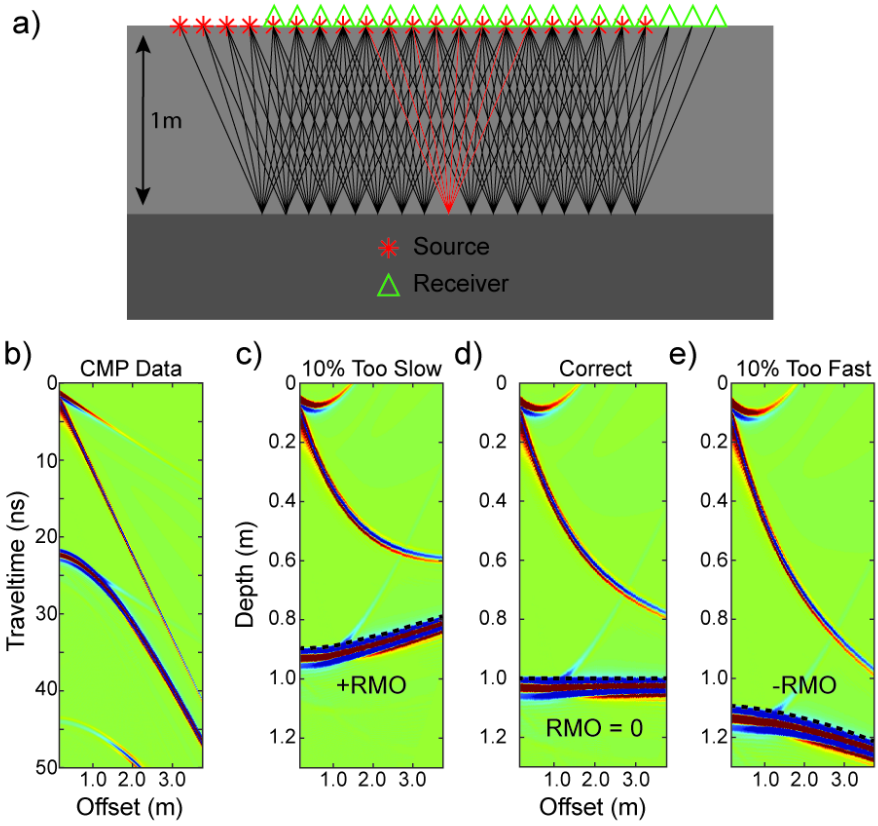

Figure 4.1: a) Data collection geometry required for the reflection tomography; b) CMP gather from the model in (a); c) CDP gather with the velocity 10% too slow; d) CDP gather with the correct velocity; and e) CDP gather with the velocity 10% too fast.

The data required for this algorithm is an ensemble of multi-offset data collected at multiple points along a line (Figure 4.1a). Given that GPR data is a time record of electromagnetic energy arriving at a point in space, we must know the proper velocity structure to migrate the data and produce a depth registered image of the GPR energy, i.e.

the stack. To solve for the velocity structure and properly migrate the data, the reflection tomography algorithm proceeds as follows [*Bradford* 2006; *Stork* 1992]:

1. Generate a starting depth vs. velocity model.
2. Migrate the data with the starting velocity model and stack the data.
3. Pick horizons on the stacked image.
4. Perform ray-tracing to the picked horizons with the velocity model.
5. Evaluate horizons for residual moveout.
6. Adjust velocity model using reflection tomography.
7. Apply revised velocity model using migration and quality check RMO.
8. Iterate at step three if necessary.

To begin the tomography algorithm a starting velocity model is required, which can be derived from any sort of prior information or analysis of the data, e.g. 1D velocity analysis. The starting velocity model is used to migrate and stack the data in the CMP ensemble. After migration using the Kirchhoff algorithm [*Yilmaz and Doherty* 2001], the CMPs are referred to as common-depth profiles (CDPs) and are essentially redundant depth registered images of the subsurface at one location. The traces within each CDP are then averaged to form one trace and placed adjacent to other migrated CDPs, i.e. stacked, to form a single depth registered 2D image of the data. Spatially coherent energy on the stack indicates a potential subsurface reflector, or horizon, that can be used for residual moveout analysis.

The goal of sequential iterations of the tomographic inversion is to minimzed the residual moveout (RMO) metric which globally optimizes the velocity structure for the entire ensemble. Figure 4.1b shows an example of CMP data acquired from the model in Figure 4.1a. If this data is migrated with the correct velocity, reflections from layers in the subsurface become flattened as a function of offset (Figure 4.1d). If the velocity estimate is incorrect, e.g. 10% too slow (Figure 4.1c) or 10% too fast (Figure 4.1e), the arrival is not flat, or exhibiting residual moveout. By globally minimizing RMO across all CMPs through correction of the velocity model, the tomography algorithm is extremely sensitive to resolving the appropriate 2D velocity structure to correctly migrate the data. Adjustments to the velocity model are made using the RMO metric and a ray-tracing algorithm which traces the paths of the GPR energy through the velocity model.

For this work, the reflection tomography was performed using the ProMax software suite which incorporates the Kirchhoff migration algorithm and the pre-stack depth migration algorithm outlined by *Stork* [1984].

4.4 Experimental Setup and Conceptual Model

A large tank (4 m x 4 m x 2 m) was constructed to facilitate the controlled study of unsaturated flow phenomenon with GPR (Figure 4.1a). The tank is constructed of wood and lined with an impermeable rubber liner. The tank is filled to a depth of 0.60 m with a medium-grained sand; hydrologic properties of the sand are listed in Table 4-1. Below the sand is a 0.30 m layer of gravel that acts as backfill for 16 individual drain cells that are pitched toward individual central drains. The drains are plumbed to individual outlets on

the outside of the tank using PVC pipes through the gravel layer. An automated data collection system was constructed to allow for the high-resolution collection of GPR data. The systems enables the rapid collection of data in the tank using three motors to control the position of the two GPR antennas [*Mangel et al.* 2015a].

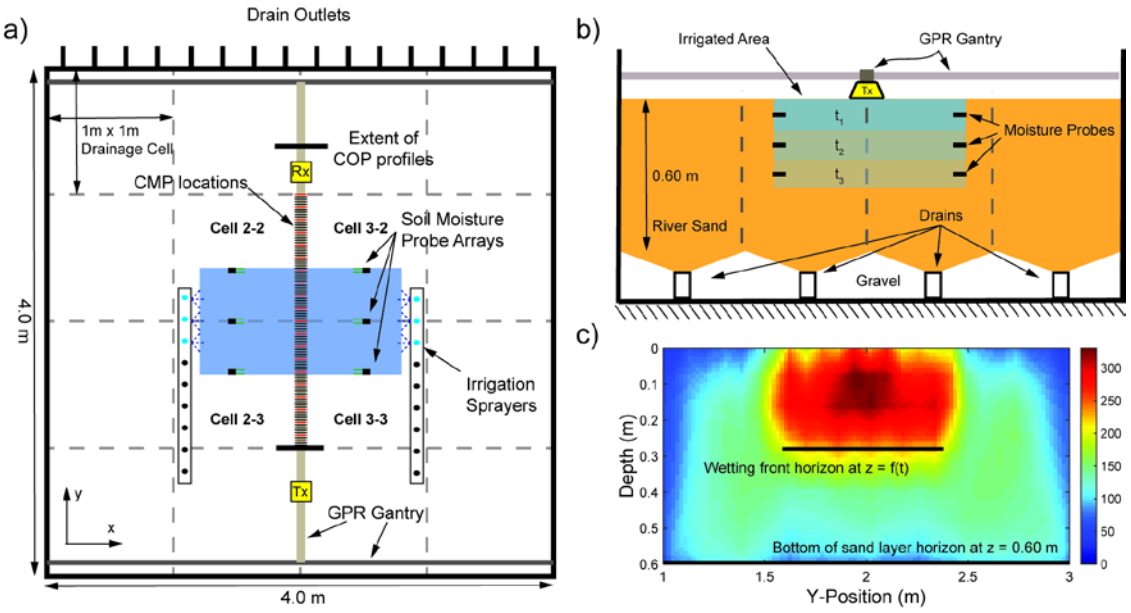

Figure 4.2: a) Schematic drawing and b) conceptual model of the experimental setup showing relative location of the irrigation sprayers, soil moisture probes and GPR data collection line. The plot in c) shows the expected ray coverage, in % of ray coverage, given the collection geometry in (a) and conceptual model in (b).

For this study, infiltration of water into the sand layer will be monitored with in-situ soil moisture probes and time-lapse multi-offset GPR surveys (Figure 4.2b). The reflection tomography algorithm will be used to estimate the velocity model by minimizing the RMO at horizons created by a static reflector at depth, i.e. the bottom of the sand layer,

and a transient wetting front reflector. The expected ray coverage, in percent of average ra y coverage, using these horizons is shown in Figure 4.2c.

Table 4-1 Mualem-van Genuchten parameters for the sand.

	Residual Water Content θ_r [vol vol^{-1}]	Saturated Water Content θ_s [vol vol^{-1}]	Air-entry parameter A [cm^{-1}]	Shape Parameter [-]	Saturated Hydraulic Conductivity [cm min^{-1}]
Equilibrium Initial Conditions	0.06	0.38	0.058	4.09	4.6
Dry Initial Conditions	0.06	0.38	0.058	4.09	1.0

4.5 Reflection tomography of Numerical Simulations

In this section we investigate reflection tomography of simulated GPR data and evaluate the ability of the algorithm to reproduce patterns associated with an infiltrating wetting front. The objectives of this section are to 1) evaluate the efficacy of the reflection tomography algorithm in reproducing the known 2D water content distributions, and 2) to gain knowledge in performing the inversions using the numerical simulations so the same protocols can later be applied to empirical data. Note that the airwave and groundwave are visible in the data, but are not analyzed, or further discussed in this work.

4.5.1 Numerical Simulations

Soil parameters from Table 4-1 were used in HYDRUS-2D to simulate the hydrologic response to an infiltration event. Two separate models were utilized to illustrate

the impact of spatial variability in water content on resolving the water content distribution. For one set of simulations, initial conditions for the model were set to equilibrium conditions, i.e. the water retention curve. The second set of simulations used uniformly dry initial conditions and a reduced hydraulic conductivity to increase the magnitude of the infiltrating wetting front relative to the background. For both simulations, the upper boundary condition was set to a constant flux of 0.125 cm/min from y = 1.6 - 2.4 m to reflect the average rate of irrigation flux used in the lab experiment. Remaining nodes at the surface were set to no flow boundaries and lower nodes were set to a seepage face with the pressure head equal to zero. For both simulations, the model domain had a depth of 0.6 m and a length of 4.0 m. Cell size was targeted as 0.04 m, however, some refinement was used at the top of the model to stabilize the solution in highly dynamic sections of the domain.

A subset of the HYDRUS-2D simulation results from both simulations were selected for GPR simulation using a MATLAB based 2D finite-difference time-domain code [*Irving and Knight* 2006]. The GPR model domain was set as a rectangle with a length of 4.0 m and a height of 1.1 m. Cell size for the simulations was set to 0.002 m in the x and z-direction. Simulations were run to obtain CMPs at locations spaced at 0.02 m intervals from y = 1.0 - 3.0 m at offsets at 0.01 m intervals from 0.16-1.0 m. The lower 0.3 m of the domain was set to gravel to resemble the lower layer of the tank with dielectric permittivity (ε) set to 2.25, electrical conductivity (σ) set to 0 mS/m, and magnetic permeability (μ) set to 0 H/m. The upper 0.2 m of the domain was set to air to simulate

the air-soil interface ($\varepsilon = 1$, $\sigma = 0$ mS/m, $\mu = 0$ H/m). Magnetic permeability and electrical conductivity of the soil were set to constant values of 1.25 μH/m and 1 mS/m, respectively. Although the conductivity would likely change as a function of the water content, we decided to keep it constant considering our focus on wave kinematics and the inability of the reflection tomography algorithm to produce absolute amplitudes [*Bradford* 2006]. Dielectric permittivity of the model domain was set using the water content values from the selected HYDRUS-2D results and the Topp equation, which relates soil moisture to dielectric permittivity for low-loss soils [*Topp et al.* 1980]. For quick computation, simulations were deployed on the Palmetto supercomputer cluster at Clemson University. Using compute nodes with 8 CPUs and 32 GB of RAM a single source simulation with a 35 ns time window finishes in about 20 minutes.

4.5.2 Results from HYDRUS and GPR Simulations

Figure 4.3 shows the representative results from numerical simulations. The HYDRUS-2D output shows the development of an infiltrating wetting front in variable background conditions. The wetted volume extends from 1.5-2.5 m in the y-direction extending slightly beyond the region of applied flux, indicated by the vertical dashed lines.

For conditions prior to irrigation, the bottom of sand reflection is horizontal on the common-offset gather, indicating a constant velocity across the model domain (Figure 4.3b). Additionally, the CMPs show identical moveout, i.e. the offset vs. traveltime relationship, of the arrivals independent of location indicating a homogeneous velocity across the model domain (Figure 4.3c, d, e). Simulations from dry initial conditions show

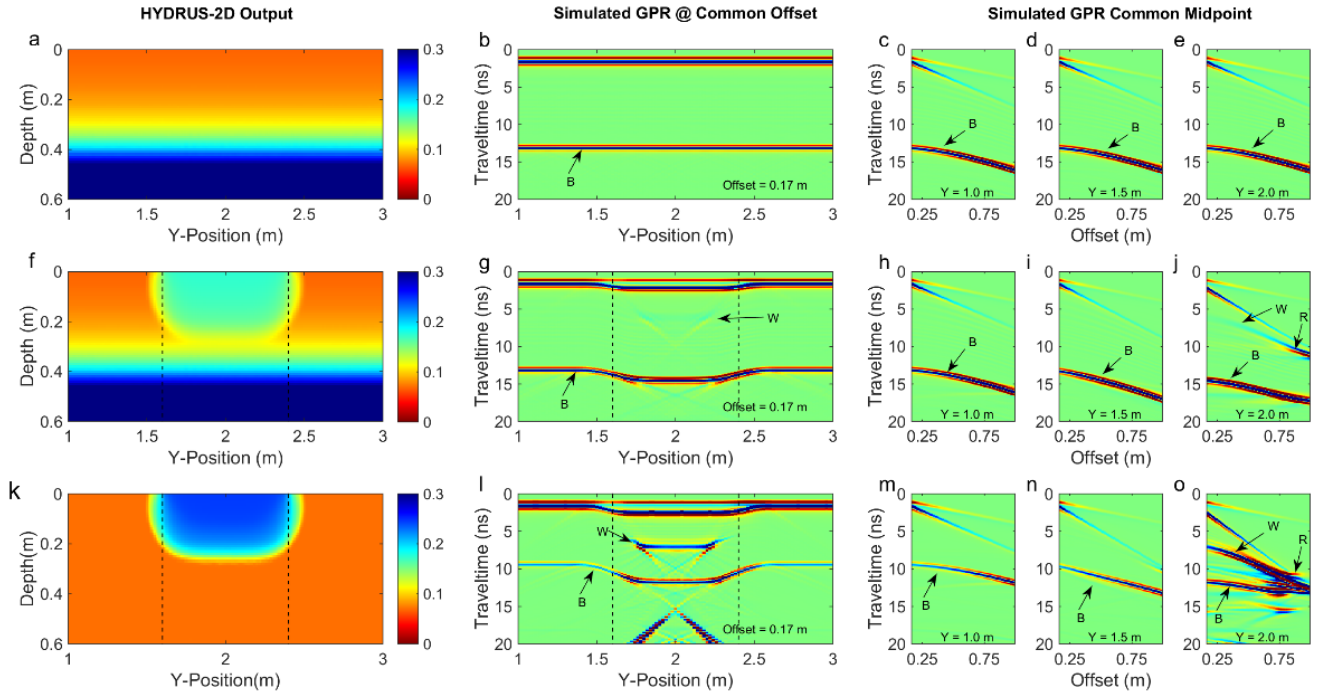

Figure 4.3: Results from numerical simulations: a, f, k) results from HYDRUS-2D simulations; b, g, l) simulated common-offset GPR data for HYDRUS-2D output at a fixed antenna offset of 0.16 m; c, d, e, h, i, j, m, n, o) simulated common-midpoint multi-offset GPR data for HYDRUS-2D output at Y = 1.0, 1.5, and 2.0 m. Vertical lines indicate the extent of the wetted surface. Arrivals annotated in the figures are the bottom of the sand layer reflection (B), the wetting front reflection (W), and a refracted arrival (R).

a nearly identical response, with the bottom of sand reflection arriving at an earlier traveltime, due to the lower water content.

For infiltration conditions with equilibrium initial conditions the common-offset simulated GPR response shows a reflection from the base of the sand layer (B) as well as the infiltrating wetting front (W). Here, the base of sand reflection is distorted at the center of the domain due to the decreased velocity caused by the infiltrating water (Figure 4.3g). Notice that the wetting front reflection (W) is incredible faint due to a lack of contrast in the water content above and below the wetting front. For the GPR, this means that the dielectric permittivity of the materials above and below the wetting front are similar and therefore, a small amount of GPR energy is reflected at this interface. The CMPs collected at y = 1.0 m show little difference than those collected at initial conditions while the CMPs collected at y = 1.5 and 2.0 m indicate changes in the velocity field (Figure 4.3h-j). Although the wetting front reflection is not observed at y = 1.5 m, the non-hyperbolic moveout of (B) indicates lateral heterogeneity in the velocity field. The CMPs at y = 2.0 m illustrate the wetting front reflection (W) well, however, some interference at large offsets is observed with a refracted wave and the base of sand reflection. Again, a reduced amplitude is observed for the wetting front reflection here, due to the small differences in water content above and below the wetting front.

A similar response is observed for a wetting front with a higher water content in a homogeneous dry background (Figure 4.3k-o). Here we see a similar amount of distortion in the bottom of sand arrival (B) on the common-offset profiles (Figure 4.3l), however, the

wetting front reflection is much stronger here when compared with Figure 4.3g. This is due to the increase contrast between the wetted volume and the background, essentially causing a larger amount of the GPR energy to be reflected back to the surface. The CMPs also reflect a similar response with the CMP at y = 1.0 m indicating no changes from initial conditions, a slight distortion in the hyperbolic moveout of the bottom of sand reflection at y = 1.5 m, and a wetting front reflection occurring at y = 2.0 m with slight interference at large offsets (Figure 4.3 m-o).

4.5.3 Reflection Tomography of Numerical Simulation Results

The reflection tomography algorithm outlined in Section 2.0 is used to resolve water content distributions from selected numerical simulations. Starting velocity models for the algorithm are determined using a 1D semblance velocity analysis [*Neidell and Taner* 1971]. At each CMP location, a single velocity is picked to flatten the bottom of sand layer reflection. The 2D velocity model is constructed by concatenating and smoothing the 1D velocities derived from individual CMPs. Data is migrated with the starting velocity model and stacked to pick the bottom of sand and wetting front horizons for RMO analysis. Results from the reflection tomography of the GPR simulation results are compared to the respective true water content distributions in Figure 4.4. For comparison, horizontal dashed lines indicate the depth of the wetting front while vertical dashed lines indicate the extent of the irrigated zone at the surface.

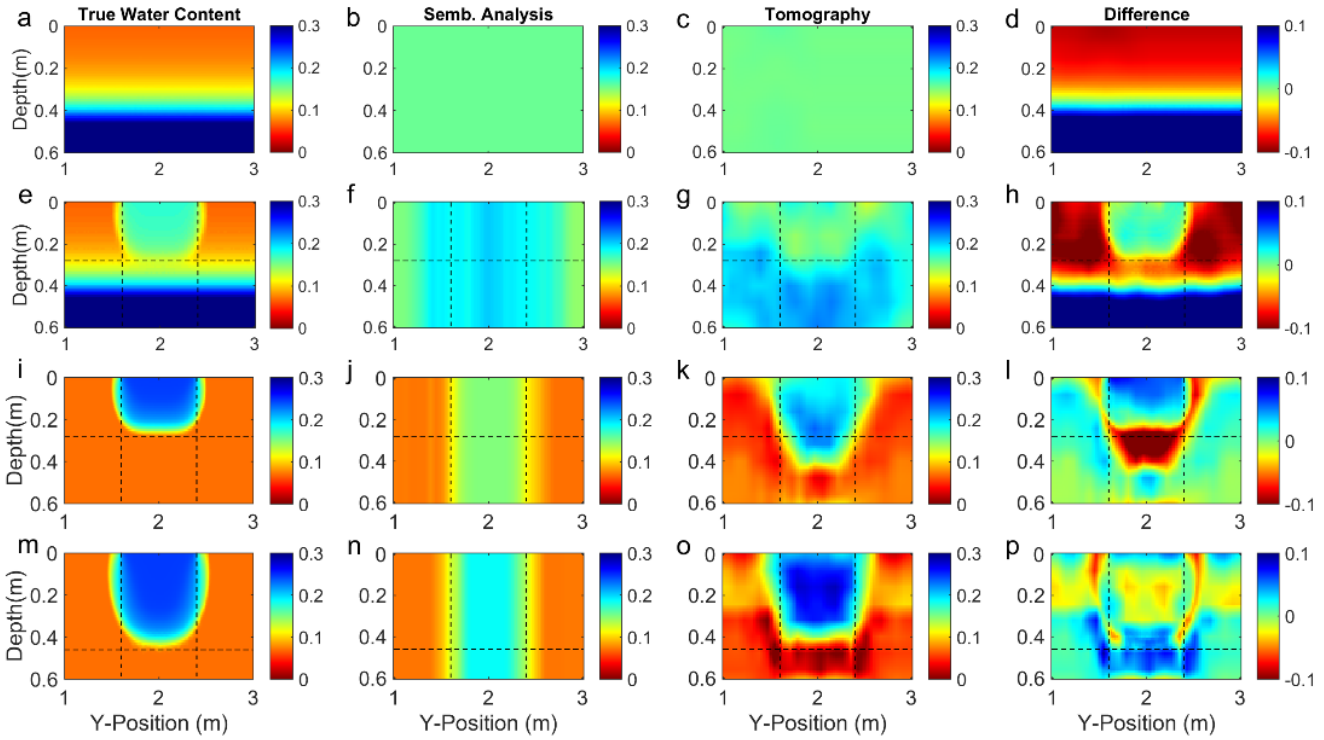

Figure 4.4: Tomography results from simulated GPR data for multiple scenarios: a, e, i, m) true water content distributions from HYDRUS-2D; b, f, j, n) water content distribution from semblance velocity analysis; c, g, k, o) water content distribution from tomography of the simulated GPR data; d, h, l, p) difference plots between the tomography results and true water content.

Prior to irrigation, the reflection tomography algorithm performs as well as the semblance analysis in resolving the distribution of water when equilibrium conditions are considered (Figure 4.4a-d). Essentially, both of these algorithms are unable to resolve the vertical distribution in water content due to the data coverage, i.e. there is simply not enough information present in the data to resolve the capillary rise at the base of the model. Therefore, the inversions produce averaged water contents and generally large errors when compared to true values (Figure 4.4d).

During infiltration conditions, however, the wetting front horizon introduces more information into the tomography inversion. With this additional horizon, reflection tomography is able to better resolve the wetter layer near the base of the domain. Additionally, although considerable errors in the tomography results persist, the tomography is able to resolve the shape and magnitude of the infiltrating wetting front when compared to the true model (Figure 4.4e-h).

When the wetted area created by the wetting front is surrounded by a homogeneous and relatively dry background, the tomographic inversions are much better at resolving the water content distribution (Figure 4.4 i-p). Water content distribution determined from the tomography of the GPR data is in good agreement with the true model produced by HYDRUS2D with the majority of errors falling below 5% water content. Overall, the vertical and horizontal trends in water content are reproduced well in both cases, however, the inversion struggles with matching the true model near the surface and has a propensity

to place the maximum depth of the wetting front around 0.40 m, despite the difference in the depth of about 0.20 m between the two cases.

In general, the magnitudes of the water content from the tomography results are in good agreement with those from the true model, however, details in the internal structure are missed by the tomography. Additionally, the tomography algorithm struggles to reproduce water content distributions consistent with capillary rise phenomenon, however, this appears to be a result of a lack of information in the GPR data. The same procedures will now be applied to the empirical data sets.

4.6 Reflection tomography of GPR data

To evaluate the performance of the tomography algorithm for field applications, we also collected empirical data in our large sand tank. Here, we monitor an infiltration and recovery period using multi-offset automated GPR data collection and in-situ soil moisture probes in a controlled study.

4.6.1 Empirical Data Collection

The GPR data were collected to optimize available multi-offset data for reflection tomography while retaining important information about the spatial geometry of reflectors. One-hundred and one CMPs were collected in a continuous fashion at 0.02 m spacing along a line located at x = 2.0 m from y = 1.0 – 3.0 m (Figure 4.2). The step size for the CMPs was set to 1 cm and the minimum and maximum offset values for the CMP were set to 0.165 m and 1.0 m, respectively. In addition to the 101 CMPs, a COP at an offset of 0.165

m was collected in the y-direction at x = 2.0 m at a 1 cm step size. With this configuration, a CMP is collected in 1.8 seconds with repeat traces collected at 3.9 minute intervals.

Irrigation is controlled using an analog flow meter and a gate valve. The water was distributed over an approximately 1.5 m x 0.80 m area on the surface at the center of the tank using a sprayer hose assembly mounted to PVC pipes. Fifteen soil moisture probes are installed at multiple locations in the tank and logged at 10 second intervals during the experiment (Figure 4.2a, b).

A GPR data set was collected prior to the start of irrigation to evaluate background conditions of the tank. Data collection continued as water was applied to the surface of the sand at a flux rate of 0.125 cm min^{-1} for a duration of 2.13 hrs. GPR data was also collected for a recovery period of 40 min. after the irrigation was terminated. In total, the experiment ran for 3 hours wherein the data collection repeated 45 times for a total of more than 500,000 traces. Selected data sets from initial, irrigation, and recovery conditions were analyzed using reflection tomography to resolve spatiotemporal patterns in water content of the soil column.

4.6.2 Ground-Penetrating Radar Results

Radar data collected in the sand tank during the infiltration experiment shows the effect of the changes in water content of the soil on the GPR data over time (Figure 4.5). At initial conditions, the bottom of the sand layer reflection (B) is visible at 10 ns traveltime in the common-offset profile collected over the imaging area (Figure 4.5a). The relatively flat appearance of this reflector indicates lateral homogeneity in the water content across

the tank. Looking at the moveout of this reflection as a function of offset at y = 1.0, 1.5, and 2.0 m, we can see that the arrival follows a hyperbolic pattern that is consistent with a normal moveout, again indicating lateral homogeneity of the water content in the sand layer (Figure 4.5b, c, d). These results are similar to observations from numerical simulation results shown in Figure 4.3.

At the onset of irrigation, the water content of the sand layer increase substantially as increases in the traveltimes of arrivals are observed (Figure 4.5e-h). Similar to observed changes in the simulated GPR response, the traveltime of the bottom of sand reflection (B) has increased by roughly 5 ns and remains at the original traveltime of 10 ns at the periphery (Figure 4.5e). Contrary to the numerical simulations, however, the appearance of a coherent reflection for the wetting front is not observed. Instead, there seem to be multiple discrete reflectors (W) that appear after the irrigation begins, indicating heterogeneity in the water flow through the sand layer. Furthermore, while the CMPs at y = 1.0 m and y = 1.5 m show a hyperbolic moveout of the base of sand reflection similar to Figure 4.5b-d, the CMP at y = 2.0 m shows a non-hyperbolic moveout pattern, indicating substantial heterogeneity in soil moisture content (Figure 4.5h). The GPR response from 95 min. shows a similar response to the previous data set, with slight differences in traveltime and amplitude of the selected arrivals (Figure 4.5i-l).Finally, after irrigation is terminated, the GPR data collected at 173 min. shows a similar response with a slight rebound in the traveltime of the bottom of sand reflection due to the now decreasing water content of the sand layer (Figure 4.5m-p).

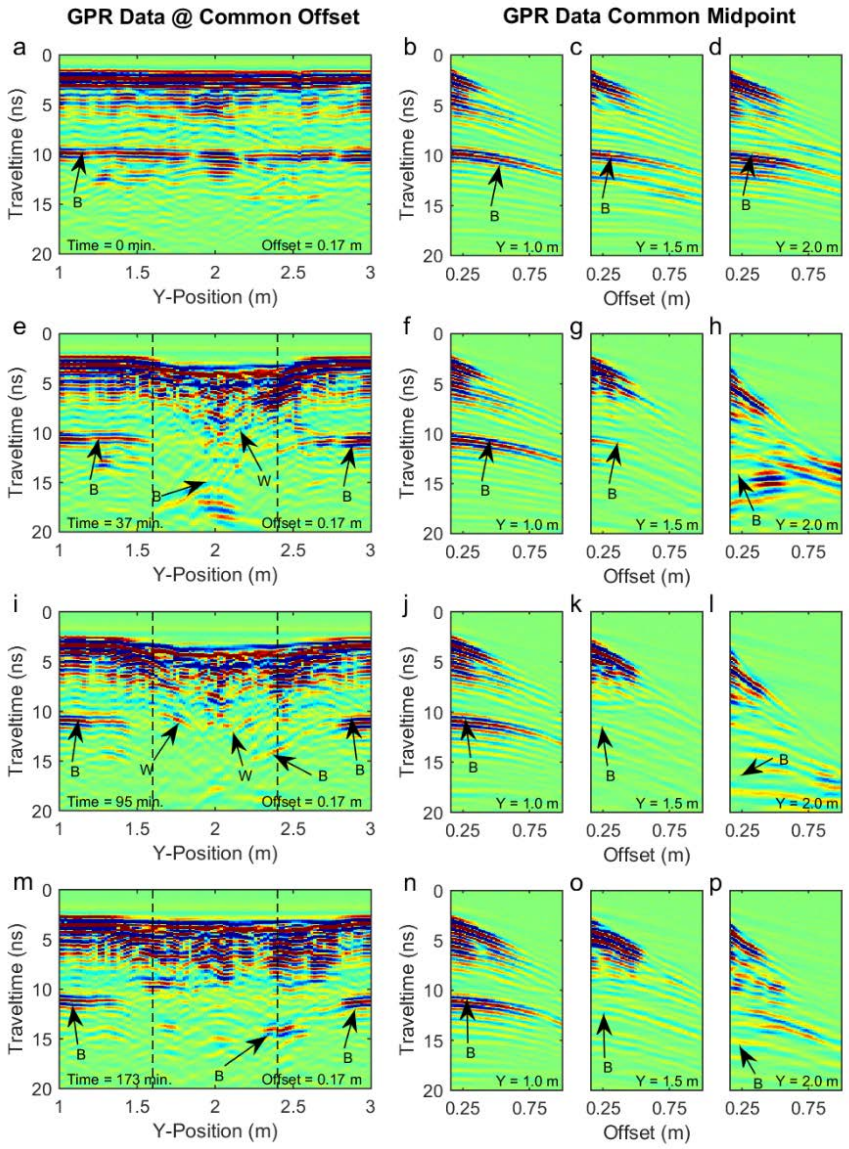

Figure 4.5: GPR data collected during the sand tank experiment in common and multi-offset projections, a-d) data collected prior to irrigation; e-h) data collected during irrigation at 37 min.; f-l) data collected during irrigation at 95 min.; m-p) data collected during recovery, after irrigation terminus at 173 min. Vertical lines indicate the extent of the wetted surface. Arrivals annotated in the figures are the bottom of the sand layer reflection (B) and the wetting front reflection (W).

Overall, the GPR data confirm a bulk increase in water content at the center of the tank and little to no changes in water content on the periphery. Additionally, the GPR data indicate that the wetting process is occurring in a relatively heterogeneous manner when compared to the idealized numerical simulation results. While this may pose an issue in picking a coherent wetting front horizon for RMO analysis, the multiple discrete reflectors associated with the wetting of the soil will suffice for the horizon analysis.

4.6.3 Reflection Tomography Results

The reflection tomography algorithm was applied to the GPR data sets presented in the previous section. Results from the tomography of the GPR data are seen in 6 and show the progression on an infiltrating wetting front over time followed by drainage of the soil during the recovery phase. Vertical lines indicate the extent of the wetted area at the surface where the irrigation was applied. Shapes on the tomography results indicate the location of points used for comparison to soil moisture probes.

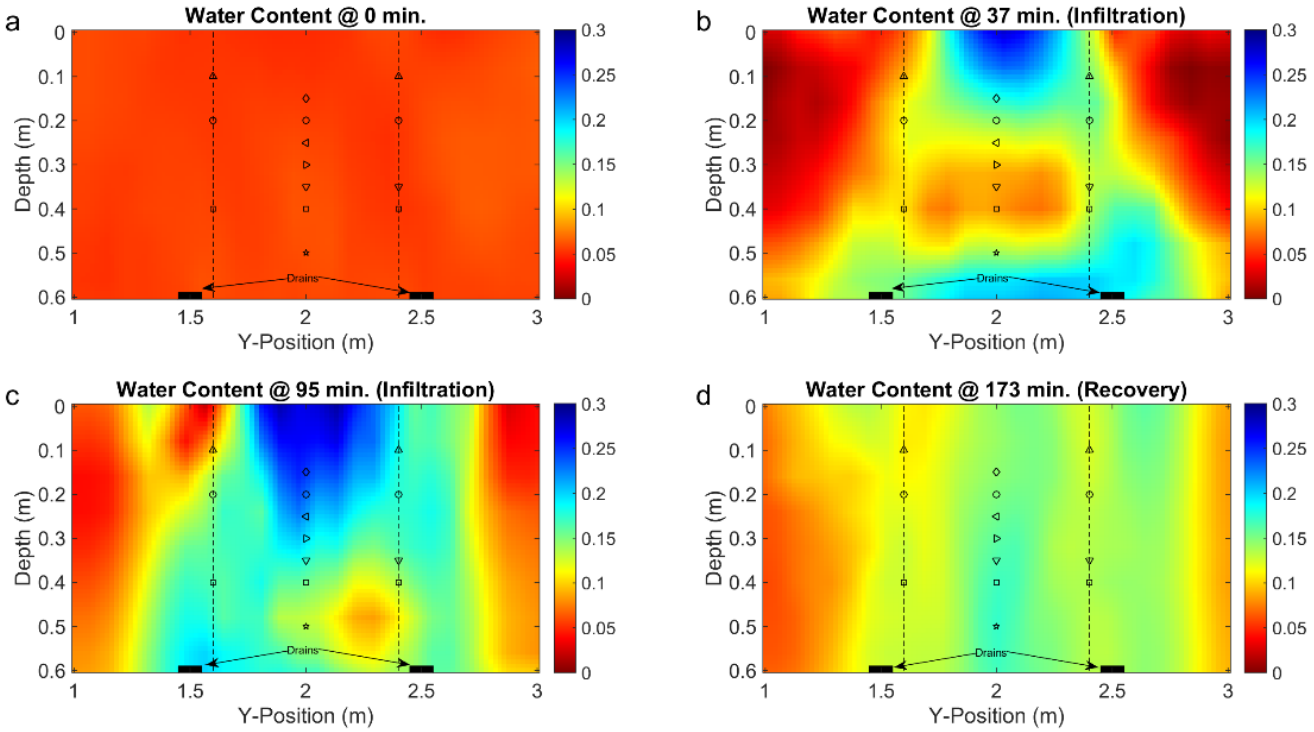

Figure 4.6: Tomography results for the GPR data: water content distributions at a) initial conditions; b) 37 min. during infiltration; c) 95 min. during infiltration; d) 173 min. during recovery, after irrigation terminus. Vertical lines indicate the extent of the wetted surface. Shapes indicate the locations used to compare to soil moisture probes in Figure 4.7.

From the initial GPR data set collected prior to irrigation, the tomography results show a generally homogeneous water content distribution for the sand layer with only slight variability, e.g. < 1% vol. / vol (Figure 4.6a). Although a distribution resembling a water retention curve should be expected, i.e. increased water content near the base consistent with a capillary rise. While the soil could potentially reach these extremely dry conditions, the homogeneous appearance is likely due to a lack of information in the data to constrain the wetter soil near the base of the sand layer, as observed in the tomography results from numerical simulations.

After the onset of irrigation, the tomography results at 37 min. reveal a considerably wetter section at the center of the tank that has propagated to an average depth of roughly 0.30 m (Figure 4.6b). The edges of the sand layer remain relatively dry with the bulk of the increased soil moisture occurring near the top of the soil in a symmetric hemisphere similar to observed patterns in the simulation results. There is a considerable increase in water content, however, around the substantially wetter bulb, which may be due to smoothing of the velocity field during the inversion. In general, given hydrologic simulation results, a sharper wetting front should be expected during infiltration. Additionally the water seems to have reached the bottom of the sand layer and spread laterally, although this is not likely. This apparent increase in water content is most likely a result of wetter soil at the base of the sand layer from capillary forces, which is appearing now in the tomography results due to the added information from analyzing the wetting front horizon, as observed in the numerical simulations.

Tomography results of the radar data collected at 95 min. show an interesting wetting pattern in response to the infiltrating water with a slightly deeper wetted area on the left of the wetted zone (Figure 4.6c). Compared to the previous time, the wetting front is significantly deeper and wider, although a small area of relatively dry soil exists at depth. At 173 min. experiment time, 36 min. after irrigation ended, the tomography results show a vertically homogeneous wetted zone that grades into drier sections toward the periphery. Again, with the absence of a wetting front reflection, the tomography is lacking information available to constrain an expected increase in soil moisture near the base of the layer.

Comparing the results of the tomography to the in-situ probe measurements shows that the tomography reflects the overall spatial and temporal trends observed in the soil moisture readings (Figure 4.7). For the probes located at multiple depths along $y = 1.6$ m the tomography results slightly overestimate the water content during infiltration, but are in excellent agreement with the soil moisture probe data at initial conditions and during recovery (Figure 4.7a). While the tomography overestimates the water content during infiltration, the results are still within about 5% vol. / vol. of the measured values. The tomography results substantially overestimate the water content at $y = 2.4$ m, however, although the tomography results are in good agreement with soil moisture probes prior to irrigation (Figure 4.7c).

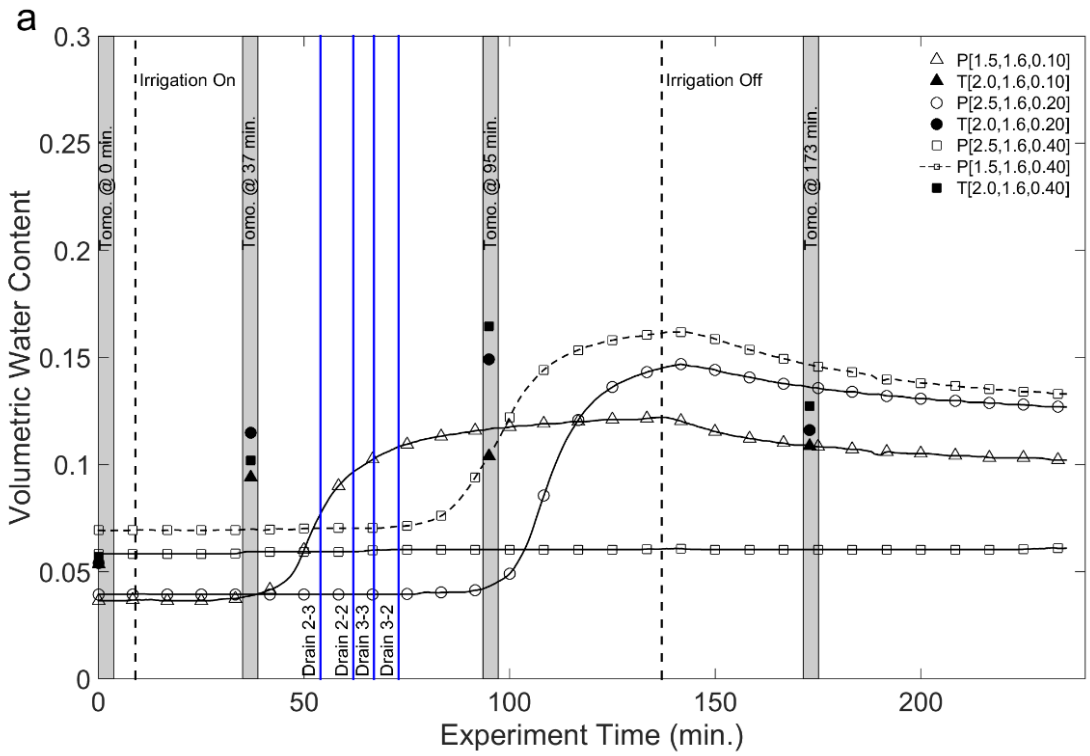

Figure 4.7a: Volumetric water content from probes located at y = 1.6 m. Vertical dashed lines indicate the start and stop of irrigation. Vertical solid lines indicate the time at which water was observed at the outflows from a specific cell (see Figure 4.2). The width of the gray bars where the tomography results are plotted are representative of the time required to collect the GPR data.

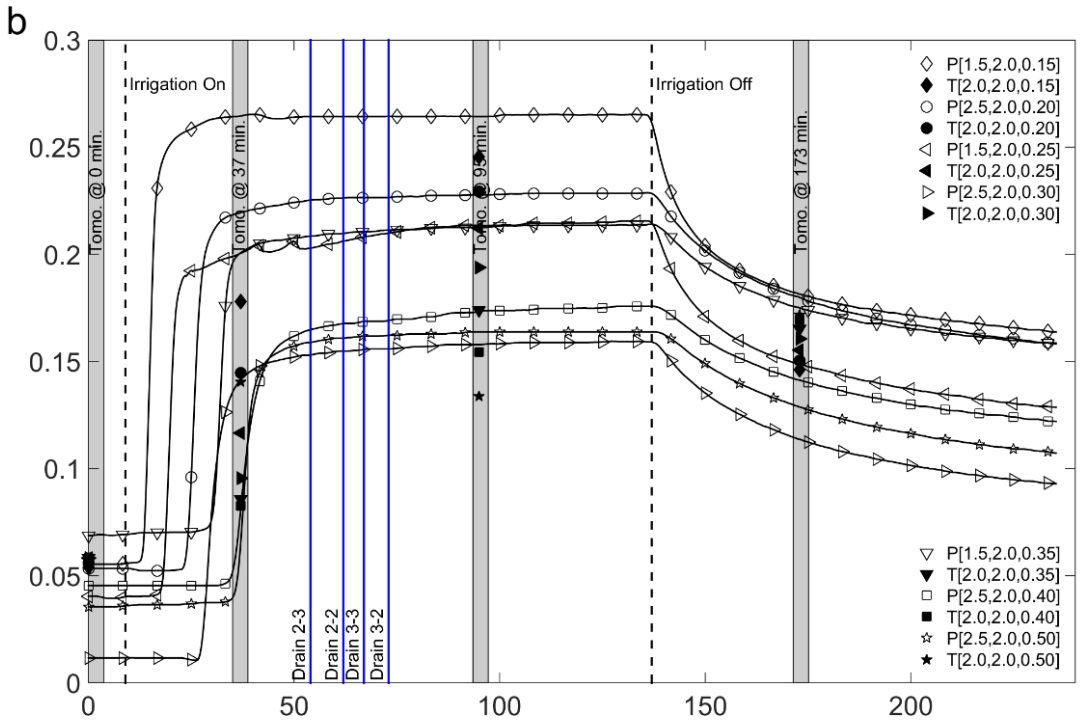

Figure 5.7b: Volumetric water content from probes located at y = 2.0 m. Vertical dashed lines indicate the start and stop of irrigation. Vertical solid lines indicate the time at which water was observed at the outflows from a specific cell (see Figure 4.2). The width of the gray bars where the tomography results are plotted are representative of the time required to collect the GPR data.

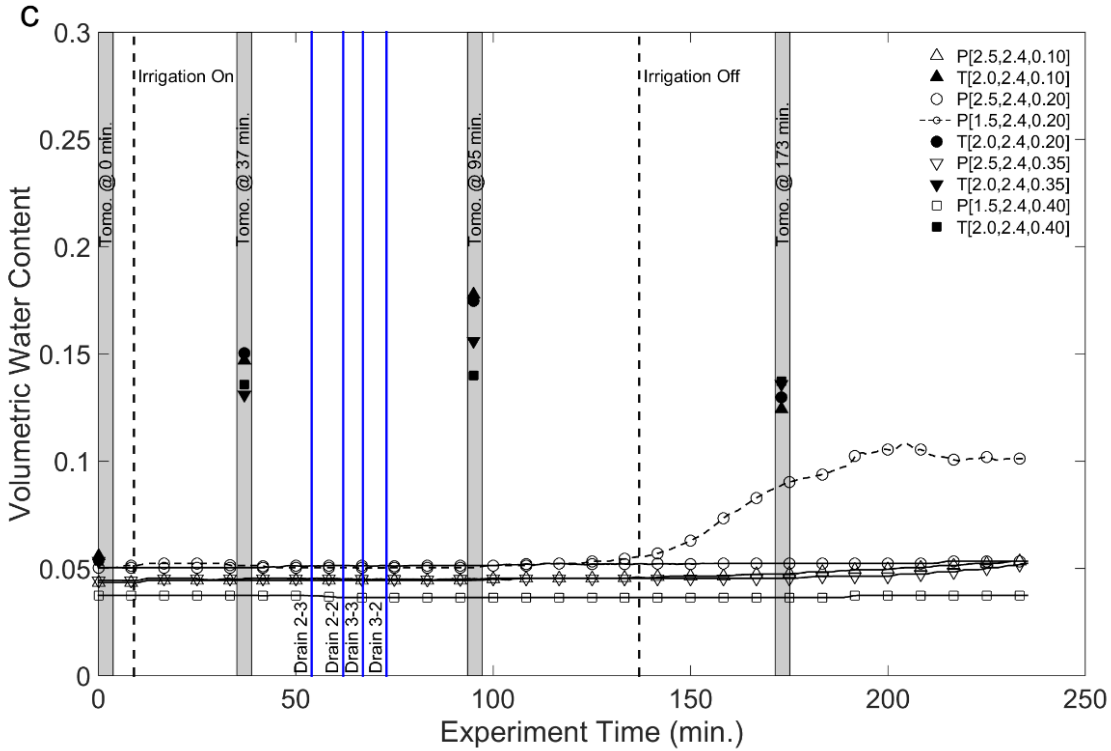

Figure 5.7c: Volumetric water content from probes located at y = 2.4 m. Vertical dashed lines indicate the start and stop of irrigation. Vertical solid lines indicate the time at which water was observed at the outflows from a specific cell (see Figure 4.2). The width of the gray bars where the tomography results are plotted are representative of the time required to collect the GPR data.

In general, the inversion results are in excellent agreement with the soil moisture probe data collected at y = 2.0 m (Figure 4.7b), given that all inversion results fall within the measured soil moisture responses, with the exception of two points at 95 minutes. Additionally, with the exception of a few points at 37 minutes, all tomography results are within 5% volumetric water content values measured by the in-situ moisture probes.

4.7 Discussion

Overall, our approach to imaging dynamic water content values provides unprecedented data-derived information regarding the 2D distribution of water at time scales on the order of a few minutes. In general, the reflection tomography algorithm was able to produce images of the water content distribution that were within 5% vol. / vol. of true water content values from the numerical simulations and the in-situ measurements from the soil moisture probes.

Our novel approach to monitoring near-surface hydrologic processes could potentially change the way ancillary information is used to invert GPR data. For example, the infiltration for this study was conceptualized in HYDRUS2D with a homogeneous layer and a constant flux across a discrete length at the top of the model domain. Evidence from tomography of the data and the soil moisture probes, however, indicated that the water flow was considerably heterogeneous compared to the idealized numerical simulations. Re-conceptualizing our model, a heterogeneous wetting front can be produced (Figure 4.8a). The radar data appear similar to previous simulation results, however, the asymmetry of the wetting front is clear in the common-offset data as the base of sand arrival (B) is

distorted in a way that reflects the asymmetry of the wetting volume (Figure 4.8b). Additionally, the wetting front reflection (W) is considerably different from previous simulations, and illustrates the dipping nature of the wetted volume. The tomography results are similar to previous simulations, where it generally resolves the shape of the wetting front but misses the fine details associated with the heterogeneous distribution of water (Figure 4.8g, h). In general, it is difficult to recognize similar patterns in the GPR data where this heterogeneity is observed (Figure 4.5i), however, there is no evidence indicating the heterogeneous distribution of water is unlikely.

More work is required, however, to investigate the sources of errors in reconstructing true water content distributions from the numerical simulations. Primarily, the utilization of a more robust migration algorithm, like reverse-time migration, should be investigated. For example, using Kirchhoff migration with the true velocity field to migrate the simulation results in Figure 4.3f-j should theoretically produce a perfect migration. However, the bottom of sand (B) and wetting front (W) horizons are not flat-lying on the multi-offset gathers (Figure 4.9a-e), which translates to migration artifacts on the stack (Figure 4.9f). This indicates that the Kirchhoff migration algorithm may not be well-suited to handle complex wave phenomena of GPR data collected during infiltration. Reverse-time migration, however, offers a solution to migrating data in the presence of complex wave phenomena and has been shown to improve stacked images in the presence of steeply dipping layers or large velocity contrasts [*Baysal et al.* 1983].

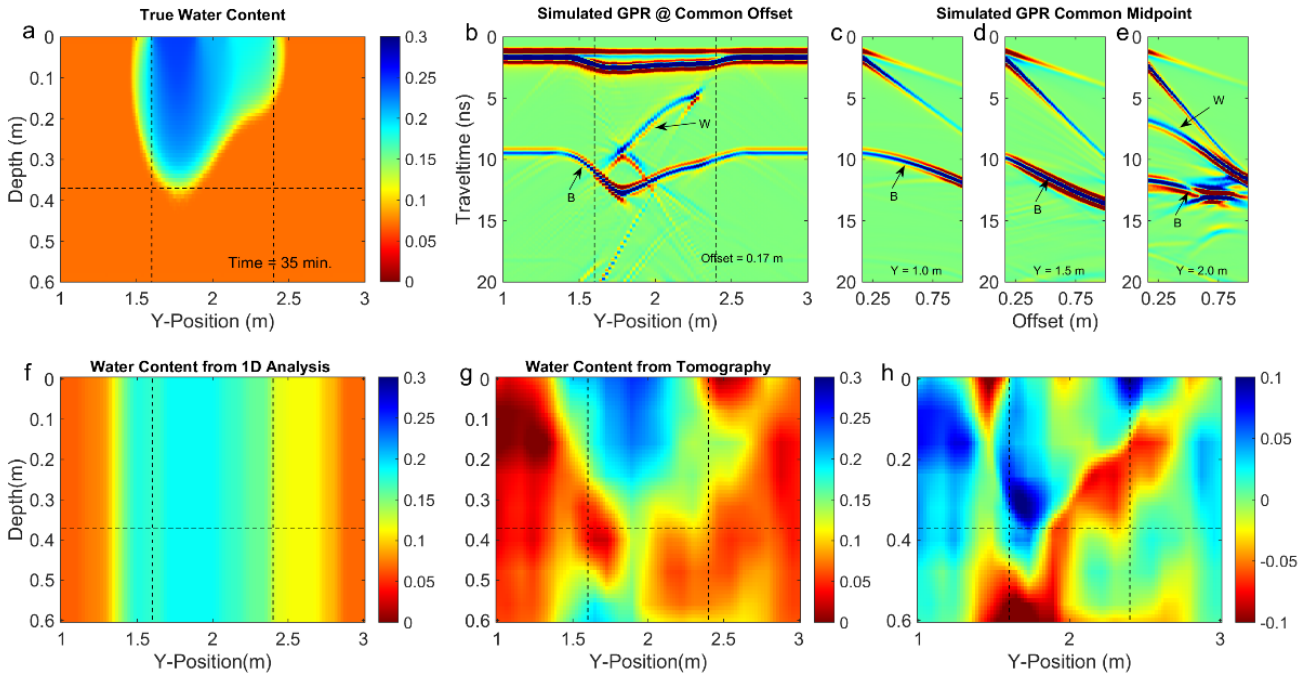

Figure 4.8: Numerical simulation results of the re-conceptualized heterogeneous wetting of the soil: a) HYDRUS 2D output; b) common-offset GPR results; c) multi-offset CMP results; d) water content from semblance analysis; e) water content from tomography; f) difference plot between tomography results and true water content. Vertical lines indicate the extent of the wetted surface. Arrivals annotated in the figures are the bottom of the sand layer reflection (B) and the wetting front reflection (W).

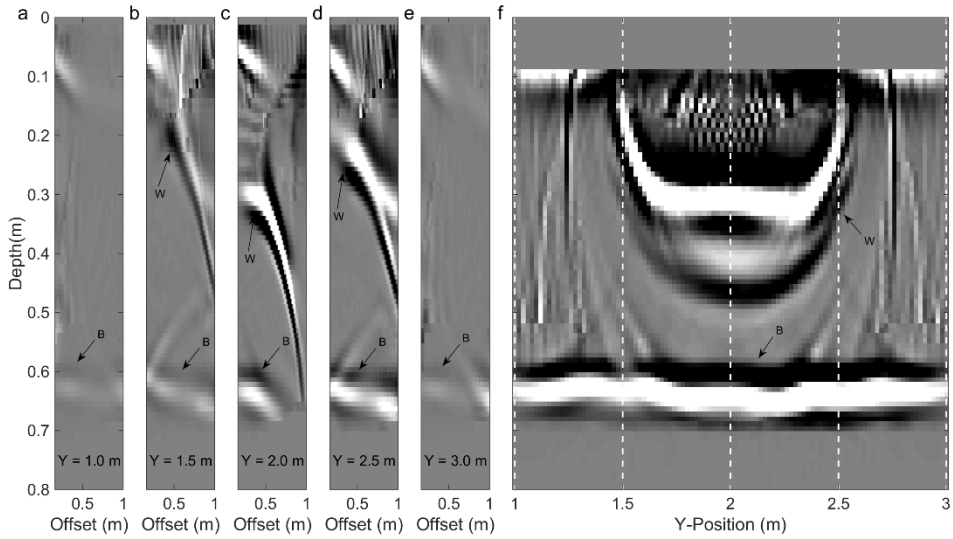

Figure 4.9: Stacks produced by migrating the simulation results and empirical GPR data: a) GPR simulation results from 35 min. stacked with the true velocity; b) GPR simulation results from 35 min. stacked with the velocity from tomography; c) GPR data from 37 min. stacked with the velocity from tomography; d) GPR simulation results from 60 min. stacked with the true velocity; e) GPR simulation results from 60 min. stacked with the velocity from tomography; f) GPR data from 95 min. stacked with the velocity from tomography.

Regardless of potential improvements to the algorithm that will be made over the coming years, the method as it stands provides a wealth of information regarding 2D distributions of water content through time. Furthermore, the method acts independently of ancillary information typically needed for inverting geophysical data and avoids making assumptions regarding subsurface reflector geometry. Additionally, the velocity models from the reflection tomography algorithm could be used as starting models for higher-order

inversion techniques, like full-waveform inversion [*Klotzshe* 2014], in a similar way that the 1D normal-moveout semblance analysis was used to generate starting models for this approach. Overall, coupling automated GPR data collection with reflection tomography provides a new method for informing conceptualization of subsurface hydrologic processes and a new method for determining transient 2D soil moisture distributions.

4.8 Conclusions

Reflection tomography in the post-migrated domain was introduced as a viable method for resolving transient soil moisture content in 2D associated with an infiltration and recovery event in a homogeneous soil. The tomography algorithm was first tested on idealized numerical simulations which produced water content distributions that were in good agreement with true water content values from the simulations, however, lacked details regarding the distinct shape of the wetted region. For most cases, the tomography was able to match the true water content values within 5-10% vol. /vol. Analysis of the data collected in the sand tank proved to be more difficult, however, the tomography was able to produce hydrologically realistic distributions of water content in space and time that were in good agreement with measurements from in-situ soil moisture probes.

More work is required, however, given errors in the migration of the simulation results using the true velocity distributions. Advance migration algorithms, like reverse-time migration, may prove to benefit this algorithm, however, when the reflection tomography algorithm is coupled with automated data collection it provides unprecedented images of dynamic soil moisture. Additionally, results from the tomography algorithm

may prove to be beneficial to higher-order inversion techniques, like full-waveform inversion, which requires accurate starting models for convergence. Overall, the automation of the GPR data collection proves to be a priceless asset in hydrogeophysical applications, which enables the usage of the reflection tomography algorithm for determining the spatiotemporal patterns in soil moisture associated with highly dynamic hydrologic events.

4.9 Acknowledgements

This material is based upon work supported by, or in part by, the National Science Foundation under grant number EAR-1151294. We would also like to acknowledge Clemson University for generous allotment of compute time on Palmetto cluster.

CHAPTER 5 - INCORPORATING CONTEXTUAL ENVIRONMENTAL INFORMATION INTO ARTIFICIAL NEURAL NETWORK TOPLOGY FOR IMPROVED TARGET CLASSIFICATION IN VARIABLE ENVIRONMENTAL SETTINGS

5.1 Abstract

Artificial neural networks (ANNs) are used to classify unexploded ordnance (UXO) and inert target signatures in simulated and empirical ground-penetrating radar (GPR) data by utilizing common offset GPR data and contextual environmental information. Minimally processed GPR data were used as stimuli for a feed-forward classification network in two different approaches. The first approach involved decoupling the signal variability from the classification by training a network to transform an arbitrary pattern back to a reference state prior to classification. The second approach involved ignoring variability in the pattern and allowing the classifier to compensate during training. Both approaches were also tested to quantify how the incorporation of the volumetric water content data would affect the classification. Classification results show significant improvement in classifier performance when contextual information is included and also show that including this information in preprocessing helps to stabilize target classification. Additionally, classification results show that utilizing the GPR data as a network stimulus can provide good network validation and generalization to other simulated data patterns, however, networks trained on simulated data are not directly applicable to field data. Finally, we suggest that while there is substantial value in first removing environmental

variability in target patterns prior to classification, more information regarding target properties should be incorporated using signal attributes derived from 3D and multi-fold GPR data.

5.2 Introduction

Artificial neural networks (ANNs) have shown significant potential for the efficient and robust classification of unexploded ordnance (UXO) signatures in ground-penetrating radar (GPR) data [1]-[6]. For example, the authors of [*Al-Nuaimy et al.* 2000] used statistical feature extraction algorithms and ANN classifiers to create an automated workflow to identify buried pipes and land mines in near real-time. Similarly, the authors of [*Kobashigawa et al.* 2011] used ANNs to classify the geophysical signatures of UXOs, steel plates, and horseshoes in multiple orientations. However, many of these studies fail to address the influence of environmental variability on the target signatures, which is an important issue in dealing with real world conditions [*Hong et al.* 2001].

GPR is sensitive to dielectric properties of the subsurface, giving it the capability to see non-metallic targets; a distinct advantage over other electromagnetic induction tools used for UXO identification. As a result, however, physical soil heterogeneities as well as spatial and temporal variability in the water content of the soil can have a significant impact on the geophysical signature of subsurface targets. Figure 5.1a illustrates that GPR reflections produced by moving antennas with a fixed spacing across a buried object (i.e., a downtrack or B scan) produces a characteristic hyperbolic signature. These signatures are not unique to UXOs and may change dramatically based on the electrical properties, shape, and orientation of the object (Figure 5.1a-e). These signatures may also vary due to soil moisture conditions (Figure 5.1f-j) given the strong relationship between soil moisture and dielectric permittivity [*Huisman et al.* 2003].

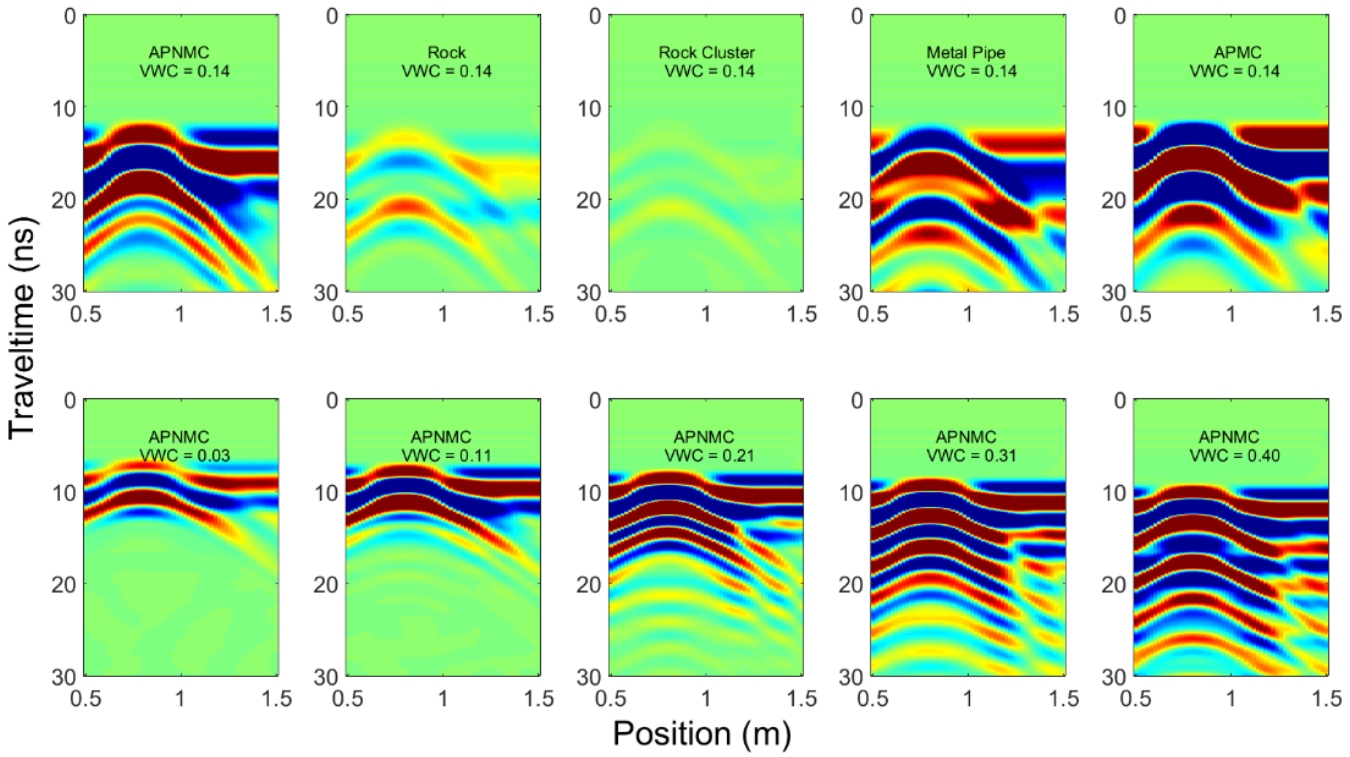

Figure 5.1: Examples of the GPR simulation outputs showing the variability in the GPR response as a function of the object shape and dielectric permittivity and the soil volumetric water content.

Few examples exist, however, which discuss the effect of soil moisture variability on target classification [*Caorsi and Cevini* 2005; *Hong et al.* 2001; *Ratto et al.* 2011; *Yang and Bose* 2005]. The authors of [*Ratto et al.* 2011], for instance, devised a context identification phase in their classification algorithm to account for changes in surface roughness and soil moisture. However, the contextual identification and target classification phases were performed independently and integrated using a relevance vector machine during the final step of the algorithm.

We hypothesize that contextual information about soil water content incorporated within the ANN topology will affect the accuracy of UXO classification. We compare the performance of five different network topologies that integrate information in different ways (Table 5-1). In all cases, the networks have a common classification network consisting of a sigmoidal data reduction layer followed by a softmax decision layer. The alternative approach we explore uses an additional sigmoidal layer as a preprocessing step to adjust the observed context-dependent GPR signals to a corrected reference state that is independent of soil moisture content. The motivation for this approach is that the extra "signal correction" layer captures contextual dependencies in the GPR data, so that the classification network itself can be trained only for only the reference state.

Table 5-1: Network topology for all ANNs considered.

Network	*Contextual Information*	**HypTan Layer**	*Contextual Information*	**Sigmoidal Layer**	*Contextual Information*	**Softmax Layer**
Cls	*N/A*	**0**	*No*	**20 nodes**	*No*	**2 nodes**
ConClsI	*N/A*	**0**	*Weighted Water Content*	**20 nodes**	*No*	**2 nodes**
ConClsII	*N/A*	**0**	*No*	**20 nodes**	*Water Content Bias*	**2 nodes**
PrpCls	*No*	**20 nodes**	*No*	**10 nodes**	*No*	**2 nodes**
ConPrpCls	*Weighted Water Content*	**20 nodes**	*No*	**10 nodes**	*No*	**2 nodes**

5.3 Methods

Five distinct objects were selected as targets for this research: i) an anti-personnel non-metallic cylindrical (APNMC) mine surrogate [*Chant et al.* 2005], ii) a metallic pipe, iii) a rock the size of an APNMC mine, iv) a cluster of small rocks, and v) a metallic object the size of an APNMC mine. The main focus of our study considers GPR responses generated by numerical simulation, thus allowing us to investigate neural network performance for a wide variety of target responses. We also collected experimental data in the lab for these targets, however, to evaluate whether it might be feasible to utilize numerical simulations as an approach to train contextual-classification networks that could

then be applied to field data. For both the numerical and experimental study, all targets were buried at a depth of 0.05 m.

5.3.1 Numerical Simulations

The simulated common-offset GPR responses of the targets were calculated for both homogeneous and heterogeneous background soil moisture conditions using a two-dimensional finite-difference, time-domain GPR forward model [*Irving and Knight* 2006]. The signal was simulated for each target object at homogeneous background water content values ranging from 1-40% volumetric water content, thus generating a homogeneous reference data set for each target. Heterogeneous soil moisture distributions were obtained by randomly selecting water contents at each pixel from a Gaussian distribution with the mean of the noise set to the desired background water content value and the standard deviation set to 5% of the mean. Dielectric permittivity for the domain was determined using the Topp equation, which relates soil moisture and dielectric permittivity for low-conductivity, lossless soils [*Topp et al.* 1980]. The electrical conductivity and magnetic permeability of the soil were set to constant values of 1 mS/m and 1.26 μH/m. Target properties were set using values from the literature for rocks, paraffin wax, and steel.

The results of the GPR simulations were pre-processed with mean background subtraction to remove the ground wave. The data were also manually clipped to remove data that did not contain the diffraction hyperbola from the target, which is similar to automated detection approaches reported by *Al-Nuaimy et al.* [2000] and *Yang and Bose* [2005] and is akin to assuming that a successful target detection has been achieved prior to

proceeding with target classification. The homogeneous water content simulations are used to train and validate the networks, whereas the heterogeneous water content simulations and adjacent object simulations are used to test the generalization of the networks.

5.3.2 Empirical Data Collection

The empirical GPR data were collected in three separate experiments in a large tank [4m x 4m x 0.60m] where the APNMC mine, metallic pipe, and rock embedded in homogeneous sand. The data were collected with an automated collection system [*Mangel et al.* 2015a] allowing fast and precise imaging, i.e., each target section could be collected in about 4 seconds . This high speed radar acquisition ensured that instantaneous snapshots of the target signal could be acquired under different environmental conditions, which were created by irrigating the surface of the sand for one hour at a constant flux rate of 0.53 cm/min followed by drying under ambient conditions. GPR data were collected at discrete intervals during drying of the sand, starting immediately after irrigation ceased. We used data from the drying phase of the experiment rather than the wetting phase so that water contents around the target would be more likely to be uniform and non-uniform distributions of water content associated with the infiltrating wetting front would be avoided. Water content was measured by taking the average of multiple measurements obtained with probes buried near the target objects.

5.3.3 Network Topology and Training

The topology of the five networks evaluated in this study is shown Table 5-1 and described in more detail below. All network weights were initialized using random Gaussian numbers from a normal distribution. The simulation results for the homogeneous water content conditions were split randomly in to training and validation data sets used to train each of the networks. Generalization of the networks was tested using results from the heterogeneous soil moisture simulations the empirical data sets collected in the tank. Network performance during generalization tests was determined using the area under the curve (AUC) metric of the receiver operating characteristic (ROC) curves, which compares the true positive (TP) and false positive (FP) rates for different classifier operating thresholds [*Fawcett* 2006].

The classifier network used for all approaches consists of a data reducing sigmoidal node layer followed by a softmax decision layer to produce a probability of the target being a UXO. This network is trained using context-dependent GPR patterns as input and the corresponding target response as output; hazardous landmines [1, 0] or inert targets [0, 1]. This classifier incorporates contextual information in different ways: 1) non-contextual classification (Cls), 2) contextual classification utilizing water content as a weighted input on the sigmoidal layer (ConClsI), and 3) contextual classification utilizing water content as a bias on the softmax layer (ConClsII). To train the network, pattern error (e_p) was defined using the cross-entropy performance function which compares the network output (o_p) and the desired response (t_p) [*Bishop* 1995; *Dunne and Campbell* 1997].

$$e_p = \sum_{p=1}^{n} t_p \log(o_p) \tag{5-1a}$$

We also take an alternative approach to the previous topology by using an additional sigmoidal layer as a preprocessing step to adjust the observed context-dependent GPR signals to a corrected reference state that is independent of soil moisture content. Once the data is corrected by this layer, it is fed to the previous non-contextual classification network (Cls). Two approaches were used for the preprocessing network where contextual information was not used (PrpCls) and also included as a weighted input on the sigmoidal layer (ConPrpCls). This network is trained using the context-dependent GPR data as input and a reference state of the same data at a specific background water content as output. For this contextual standardization network, pattern error was defined as the L1 norm of the network output and the desired response.

$$e_p = \sum_{p=1}^{n} |t_p - o_p| \tag{5-1b}$$

Note that epoch error was used for all network error evaluation and is the sum of all pattern errors for one training iteration.

5.4 Network Performance Results

All networks were trained with results from idealized GPR simulations with a target buried in a soil with homogeneous water content. Given that homogeneity is rarely the case in field applications, we also discuss the performance of each network using ROC curves obtained for two additional data sets: i) simulation results with heterogeneous water content and ii) empirical data collected in homogeneous soil. Optimal operating thresholds

were also determined for all networks with the cost of a false negative set as three times the cost of a false positive. A summary of performance measures from all networks can be seen in Table 5-2.

Table 5-2: Network Performance Results Summary: AUC = Area under the ROC curve, Opt = Optimal operating threshold, TP = True positive rate, FP = False positive rate.

	Homogeneous Training				***Homogeneous Validation***				***Heterogeneous Generalization***				***Empirical Generalization***			
Network	AUC	Opt	TP	FP	AUC	Opt	TP	FP	AUC	Opt	TP	FP	AUC	Opt	TP	FP
Cls	0.999	0.59	0.97	0	1.0	0.56	1	0	0.771	0.99	0.41	0.04	0.518	1.0	0	0
ConClsI	0.999	0.66	0.95	0	1.0	0.53	1	0	0.840	0.56	0.81	0.11	0.468	1.0	0.29	0.08
ConClsII	0.999	0.61	0.97	0	1.0	0.58	1	0	0.838	0.99	0.49	0.06	0.550	1.0	0.13	0
PrpCls	0.996	0.57	0.98	0.02	0.999	0.58	0.97	0	0.773	0.99	0.49	0.06	0.543	1.0	0	0
ConPrpCls	0.958	0.74	0.73	0.01	0.993	0.57	0.97	0.03	0.849	0.89	0.74	0.10	0.548	1.0	0	0

5.4.1 Network Training and Validation Results

All networks were trained using the back-propagation algorithm with epoch error misfit functions until less than 5% improvement was seen in the validation or the epoch error decreased below 10. A maximum epoch error of 10 was chosen based on validation performance with the homogeneous validation set, i.e. values lower than this resulted in an over-trained network.

Training and validation using the homogeneous simulations return ROC curves with AUC approaching one for all networks (Figure 5.2). When the preprocessing layer is brought into the classification algorithm, the AUC decreases slightly to 0.996 and even more in the training of the contextual preprocessing network where it drops to 0.958. There is a significant decrease in the TP rate for the ConPrpCls network, although FP rates remain very low.

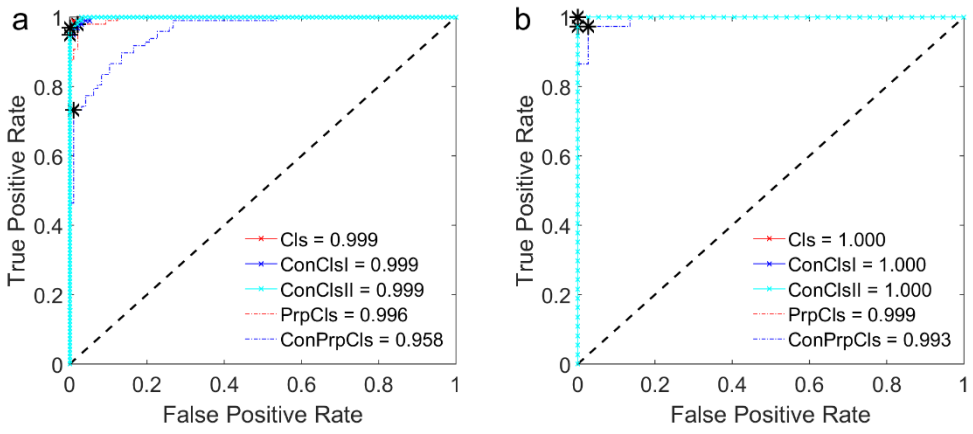

Figure 5.2: ROC curves for all networks using homogeneous training and generalization data sets.

Similar results from the validation set are observed as well, where large AUC metrics are present for all networks and small FP rates occur with the addition of the preprocessing layer. However, a reduction in the TP rates was not observed for the ConPrpCls network as observed in the training, indicating larger pattern variability in the training set. In general, training and generalization results from the homogeneous data set indicate that the classifiers are capturing important differences in the signal to discriminate between UXO and clutter.

5.4.2 Network Performance with Heterogeneous Simulation Results

The contextual preprocessing classifier network (ConPrpCls), which used contextual data to correct GPR signals prior to a non-contextual classification, had the best performance according to ROC metrics with the heterogeneous data set. This is followed closely by the contextual classifier network (ConClsI), which utilized a contextual approach to the standard classification network. In both of these cases, the ROC curves show a typical concave shape with high values for the AUC metric (Figure 5.3), i.e., 0.840 for the ConCls network and 0.849 for the ConPrpCls network. The optimal operating point on the ConCls ROC curve, indicated by the asterisk on the line, occurs at FP = 0.11 and TP = 0.81 using a detection threshold of 0.56. The optimal operating point on the ConPrpCls ROC curve occurs at FP = 0.10 and TP = 0.74 using a detection threshold of 0.89.

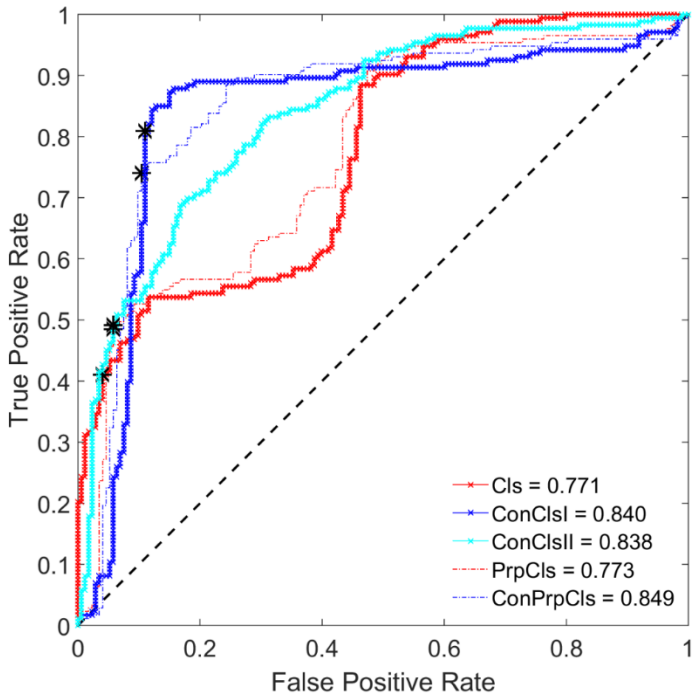

Figure 5.3: ROC curves for generalization of the networks to simulation results that used a heterogeneous background water content.

The ConClsII network also performed well by the AUC metric (0.838) however, has a low TP rate (0.49) at the optimal point. In general, the other networks perform very poorly for classifying the targets in a heterogeneous environment, indicated by relatively low AUC values and low TP rates at their optimal operating points. Additionally, all networks, except for the ConClsI network, have extremely high optimal operating thresholds, indicating that these networks are having difficulty in distinguishing key features between the clutter and UXO signals in parameter space for some patterns.

5.4.3 Network Performance with Empirical Data

Network generalization to patterns from empirical data sets was largely unsuccessful as all of the networks showed classification nearly similar to that of a random classifier (Figure 5.4), i.e. all networks show AUC values approaching 0.50. Given the poor performance of this classifier on these empirical data patterns, further steps must be taken to improve the applicability of simulation-trained classifiers for field deployment. This may be accomplished through more representative simulations, i.e. more accurate models, or by evolving the classifier to interrogate features of the data, e.g. spectral information, rather than the data itself.

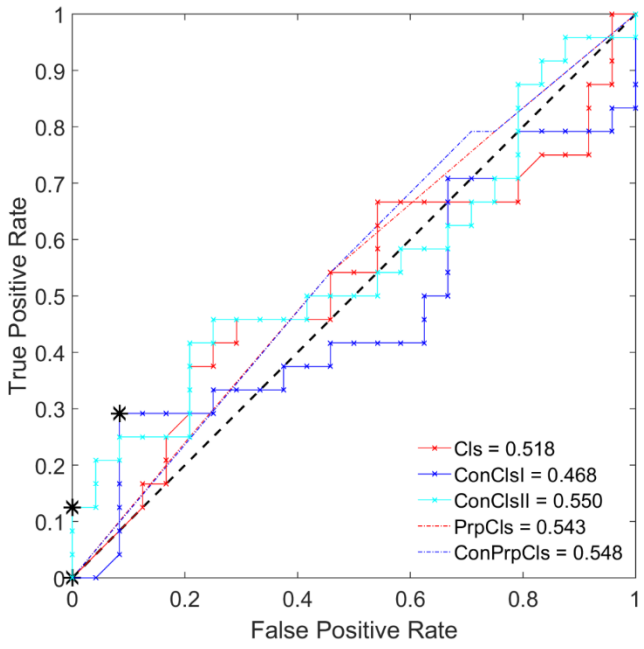

Figure 5.4: ROC curves for generalization of the networks empirical data patterns.

5.5 Discussion

Classification results from simulated data patterns indicate that the inclusion of contextual information and changes in network topology can alter the performance of neural network classifiers. The non-contextual networks are being largely outperformed by the contextual networks as indicated by the separation of these networks in the ROC space, i.e. a significant increase in classifier performance occurs when contextual information is included (Figure 5.3). This indicates that the utilization of contextual information in context-dependent data classification algorithms carries value in discriminating between clutter and UXO targets.

In order to clarify how these networks are handling the data, the heterogeneous data set was fed through the trained ConClsI, ConPrpCls, and PrpCls networks (Figure 5.5). Figure 5.5a shows the true class for each pattern, note that water content increases from the lowest to highest pattern number for a given target. This variability in the target signal as a function of water content can be seen in the classification output from the ConClsI and PrpCls networks (Figure 5.5b, d). However, the contextual preprocessing network was able to eliminate the variability in target classification due to changes in water content (Figure 5.5c). This is less prevalent in the non-contextual preprocessing network for the pipe and rock clutter targets, however, the network generally struggles in classifying these objects as clutter, i.e. high values compared to the true class.

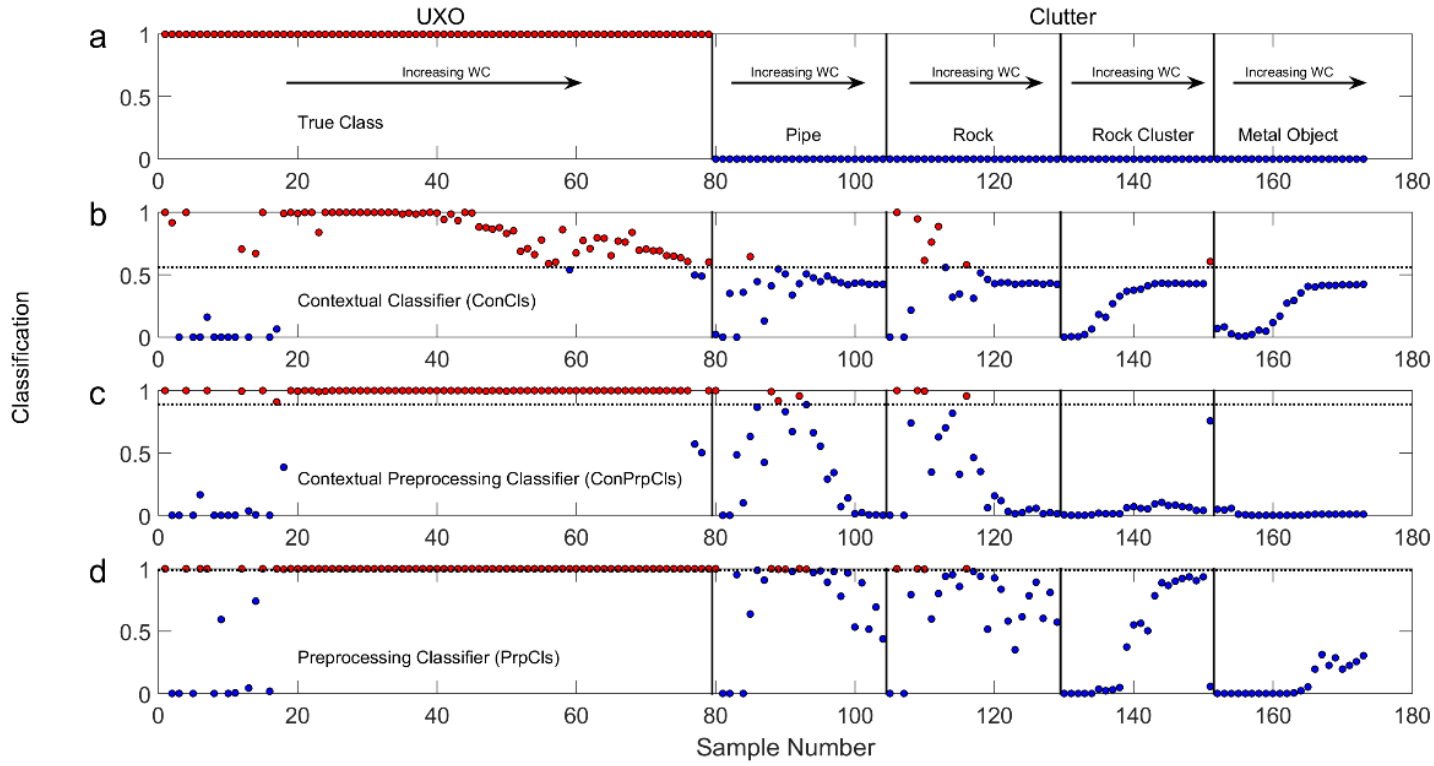

Figure 5.5: Classification results from the heterogeneous data set.

Overall, it seems that all classifiers struggle with objects buried in very dry conditions and have some range of water content that optimizes classification. All networks have difficulty in classifying the UXO and buried rock at low water content. This is less true for the pipe, rock cluster, and metal clutter targets due to greater differences in target signatures when compared to UXO signatures. However, this indicates that there may be some optimal range for each target that the preprocessing step could be optimized to mimic, effectively increasing the performance of the classifier.

Given the ROC performance measures in Table 5-2, and a visual inspection of network outputs from Figure 5.5, the contextual preprocessing classifier successfully classifies the majority of targets while eliminating target variability due to environmental conditions. This indicates that volumetric water content may be better applied in regularizing signal patterns in classification algorithms rather than in the decision layer.

More information can also be derived, however, regarding target properties from a more complete data set. It has been established that these objects are very clearly visible on 3D GPR data and that the amount of information from these high-resolution images is clearly valuable to UXO classification [*Sato et al.* 2012], however, no studies to date have investigated the use of this information in UXO classification. Additionally, several studies have shown success in utilizing signal attributes from standard 2D common offset GPR data [*Gader et al.* 2004; *Ho et al.* 2004; *Kleinmann et al.* n.d.; *Zyada et al.* 2011] which motivates the usage of multi-offset data given that it holds important information about

target electrical properties, which can be derived using amplitude versus offset (AVO) relationships [*Baker* 1998].

5.6 Conclusions

Artificial neural networks (ANNs) were used to classify unexploded ordnance (UXO) and inert target signatures in simulated and empirical ground-penetrating radar (GPR) data by utilizing common offset GPR data and contextual environmental information. Results show that classifiers that incorporate contextual information, e.g. average water content, are best at discriminating between UXO and clutter on context-dependent GPR data. Additionally, contextual information may be more effectively used in signal processing steps prior to classification of the target as it is able to help correct patterns to a reference state and stabilize target classification. While there is value in including environmental information in signal processing steps prior to classification, 3D and multi-fold GPR data have the potential to provide more information about target properties and features, which could substantially improve classifier performance. Finally, we conclude that additional steps must be taken to classify targets on field data using algorithms trained on idealized simulations.

5.7 Acknowledgements

This material is based upon work supported by, or in party by, the US Army Research Office (W911NF-10-1-0365, W911NF-10-1-0292). We would also like to acknowledge Clemson University for allotment of compute time on Palmetto cluster.

CHAPTER 6 – WORKS CITED

Al-Nuaimy, W., Y. Huang, M. Nakhkash, M.T.C. Fang, V.T. Nguyen & A. Eriksen, 2000. Automatic detection of buried utilities and solid objects with GPR using neural networks and pattern recognition. *Journal of Applied Geophysics*, 43(2-4), pp.157–165. Available at: http://linkinghub.elsevier.com/retrieve/pii/S0926985199000555.

Arcone, S.A., 1984. Field observations of electromagnetic pulse propagation in dielectric slabs. *Geophysics*, 49(10), pp.1763–1773. Available at: http://library.seg.org/doi/abs/10.1190/1.1441584.

Arcone, S.A., P.R. Peapples & L. Liu, 2003. Propagation of a ground-penetrating radar (GPR) pulse in a thin-surface waveguide, Geophysics, 68(6), pp.1922–1933. Available at: http://library.seg.org/doi/abs/10.1190/1.1635046.

Baker, G.S., 1998. Applying AVO analysis to GPR data. *Geophysical Research Letters*, 25(3), pp.397–400. Available at: http://doi.wiley.com/10.1029/97GL03773.

Bakker, J., J. van der Kruk, J. Bikowski & H. Vereecken, 2011. Two-layer inversion of dispersive GPR data due to freezing induced waveguides — A synthetic study. *2011 6th International Workshop on Advanced Ground Penetrating Radar (IWAGPR)*, pp.1–5. Available at: http://ieeexplore.ieee.org/lpdocs/epic03/wrapper.htm?arnumber=5963841.

Baysal, E., D. Kosloff & J. Sherwood, 1983. Reverse Time Migration. *Geophysics*, 48(11), pp.1514–1524.

Bishop, C.M., 1995. *Neural Networks for Pattern Recognition*, New York, NY: Oxford University Press.

Bishop, T.N., K.P. Bube, R.T. Cutler, R.T. Langan, P.L. Love, J.R. Resnick, R.T. Shuey, D.A. Spindler & H.W. Wyld, 1985. Tomographic determination of velocity and depth in laterally varying media. *Geophysics*, 50(6), pp.903–923.

Bradford, J.H., 2006. Applying reflection tomography in the postmigrated domain to multifold ground-penetrating radar data. *Geophysics*, 71(1), pp.K1–K8. Available at: http://library.seg.org/doi/abs/10.1190/1.2159051 [Accessed November 3, 2014].

Bradford, J.H., 2008. Measuring Water Content Heterogeneity Using Multifold GPR with Reflection Tomography. *Vadose Zone Journal*, 7(1), p.184. Available at: https://www.soils.org/publications/vzj/abstracts/7/1/184 [Accessed October 18, 2014].

Brantley, S., T.S. White, A.F. White, D. Sparks, D. Richter, K. Pregitzer, L. Derry, J. Chorover, O. Chadwick, R. April, S. Anderson & R. Amundson, 2006. *Frontiers in Exploration of the Critical Zone: Report of a workshop sponsored by the National Science Foundation (NSF)*, Newark, DE.

Buchner, J.S., A. Kuhne, B. Antz, K. Roth & U. Wollschlager, 2011. Observation of volumetric water content and reflector depth with multichannel ground-penetrating radar in an artificial sand volume. *2011 6th International Workshop on Advanced Ground Penetrating Radar (IWAGPR)*, pp.1–5. Available at: http://ieeexplore.ieee.org/lpdocs/epic03/wrapper.htm?arnumber=5963910.

Budden, K.G., 1961. *The wave-guide mode theory of wave propagation*, Englewood Cliffs, NJ: Prentice Hall Inc.

Busch, S., L. Weihermüller, J.A. Huisman, C.M. Steelman, A.L. Endres, H. Vereecken & J. van der Kruk, 2013. Coupled hydrogeophysical inversion of time-lapse surface GPR data to estimate hydraulic properties of a layered subsurface. *Water Resources Research*, 49(12), pp.8480–8494. Available at: http://doi.wiley.com/10.1002/2013WR013992 [Accessed October 10, 2014].

Caorsi, S. & G. Cevini, 2005. An Electromagnetic Approach Based on Neural Networks for the GPR Investigation of Buried Cylinders. *IEEE Geoscience and Remote Sensing Letters*, 2(1), pp.3–7. Available at: http://ieeexplore.ieee.org/lpdocs/epic03/wrapper.htm?arnumber=1381337.

Carsel, R.F. & R.S. Parrish, 1998. Developing joint probability distributions of soil water retention characteristics. *Water Resources Research*, 24(5), pp.755–769.

Chant, I., D. Lee & D. Ireland, 2005. *DSTO Landmine Detection Test Targets*

Duan, Q.Y., V.K. Gupta & S. Sorooshian, 1993. Shuffled complex evolution approach for effective and efficient global minimization. *Journal of Optimization Theory and Applications*, 76(3), pp.501–521.

Dunne, R. & N. Campbell, 1997. On the pairing of the Softmax activation and cross-entropy penalty functions and the derivation of the Softmax activation function. *Proc. 8th Aust. Conf. on the Neural Networks*, pp.1–5. Available at: http://citeseerx.ist.psu.edu/viewdoc/download?doi=10.1.1.49.6403&rep=rep1&type=pdf.

Fawcett, T., 2006. An introduction to ROC analysis. *Pattern Recognition Letters*, 27(8), pp.861–874. Available at: http://linkinghub.elsevier.com/retrieve/pii/S016786550500303X [Accessed July 9, 2014].

Flury, M., H. Flfihler, W.A. Jury & J. Leuenberger, 1994. Susceptibility of soils to preferential flow of water : A field study. *Water Resources Research*, 30(7), pp.1945–1954.

Gader, P., W. Lee & J.N. Wilson, 2004. Detecting Landmines With Ground-Penetrating Radar Using Feature-Based Rules , Order Statistics , and Adaptive Whitening. *IEEE Transactions on Geoscience and Remote Sensing*, 42(11), pp.2522–2534.

Gardner, G.H.F., W.S. French & T. Matzuk, 1974. Elements of migration and velocity analysis. *Geophysics*, 39(6), pp.811–825.

Grasmueck, M., P. Marchesini, G.P. Eberli, M. Zeller & R. Van Dam, 2010. 4D GPR Tracking of Water Infiltration in Fractured High-Porosity Limestone. *13th Internation Conference on Ground Penetrating Radar*, pp.1–6.

Grasmueck, M., R. Weger & H. Horstmeyer, 2005. Full-resolution 3D GPR imaging. *Geophysics*, 70(1), pp.K12–K19. Available at: http://library.seg.org/doi/abs/10.1190/1.1852780.

Greaves, R.J., D.P. Lesmes, J.M. Lee & M.N. Toksoz, 1996. Velocity variations and water content estimated from multi-offset , ground-penetrating radar. *Geophysics*, 61(3), pp.683–695.

Grote, K., C. Anger, B. Kelly, S. Hubbard & Y. Rubin, 2010. Characterization of Soil Water Content Variability and Soil Texture using GPR Groundwave Techniques. *Journal of Environmental & Engineering Geophysics*, 15(3), pp.93–110. Available at: http://jeeg.geoscienceworld.org/cgi/doi/10.2113/JEEG15.3.93.

Grote, K., S. Hubbard, J. Harvey & Y. Rubin, 2005. Evaluation of infiltration in layered pavements using surface GPR reflection techniques. *Journal of Applied Geophysics*, 57(2), pp.129–153. Available at: http://linkinghub.elsevier.com/retrieve/pii/S0926985104000874 [Accessed October 23, 2014].

Guo, L., J. Chen & H. Lin, 2014. Subsurface lateral preferential flow network revealed by time-lapse ground-penetrating radar in a hillslope. *Water Resources Research*, 50, pp.9127–9147.

Haarder, E.B., M.C. Looms, K.H. Jensen & L. Nielsen, 2011. Visualizing Unsaturated Flow Phenomena Using High-Resolution Reflection Ground Penetrating Radar. *Vadose Zone Journal*, 10(1), p.84. Available at: https://www.soils.org/publications/vzj/abstracts/10/1/84 [Accessed October 23, 2014].

von Hebel, C., S. Rudolph, A. Mester, J.A. Huisman, P. Kumbhar, H. Vereecken & J. van der Kruk, 2014. Three-dimensional imaging of subsurface structural patterns using quantitative large-scale multiconfiguration electromagnetic induction data. *Water Resources Research*, 50, pp.2732–2748.

Hendrickx, J.M.H. & M. Flury, 2001. Uniform and Preferential Flow Mechanisms in the Vadose Zone. In *Conceptual Models of Flow and Transport in the Fractured Vadose Zone*. Washington, D.C.: National Academy Press, pp. 149–187.

Ho, K.C., L.M. Collins, L.G. Huettel & P.D. Gader, 2004. Discrimination Mode Processing for EMI and GPR Sensors for Hand-Held Land Mine Detection. *IEEE Transactions on Geoscience and Remote Sensing*, 42(1), pp.249–263.

Hong, S., T. Miller, H. Tobin, B. Borchers, J.M.H. Hendrickx, T. Hague & B. Baertlein, 2001. Impact of Soil Water Content on Landmine Detection Using Radar and Thermal Infrared Sensors. , 4394, pp.409–416.

Huisman, J.A., S.S. Hubbard, J.D. Redman & A.P. Annan, 2003. Measuring Soil Water Content with Ground Penetrating Radar: A Review. *Vadose Zone Journal*, 2(4), pp.476–491. Available at: http://vzj.scijournals.org/cgi/doi/10.2113/2.4.476.

Huisman, J.A., C. Sperl, W. Bouten & J.M. Verstraten, 2001. Soil water content measurements at different scales : accuracy of time domain re ¯ ectometry and ground-penetrating radar. *Journal of Hydrology*, 245, pp.48–58.

Irving, J. & R. Knight, 2006. Numerical modeling of ground-penetrating radar in 2-D using MATLAB. *Computers & Geosciences*, 32(9), pp.1247–1258. Available at: http://linkinghub.elsevier.com/retrieve/pii/S0098300405002621 [Accessed October 21, 2014].

Kleinmann, L., J. Laugks & K.-P. Nick, *IMAGE PROCESSING AND PA'ITERN RECOGNITION IN GROUND PENETRATING RADAR DATA Ljudmila Kleinmann*, Jurgen Laugks*, Klaus-Peter Nick** *Fraunhofer-Institute,*

Klotzshe, A., 2014. Detection of spatially limited high-porosity layers using crosshole GPR signal analysis and full-waveform inversion. *Water Resources Research*, 50(8), pp.6966–6985.

Kobashigawa, J.S., H. Youn, M.F. Iskander & Y. Zhengqing, 2011. Classi fi cation of Buried Targets Using Ground Penetrating Radar : Comparison Between Genetic Programming and Neural Networks. *IEEE Antennas and Wireless Propagation Letters*, 10, pp.971–974.

Lagarias, J.C., J.A. Reeds, M.H. Wright & P.E. Wright, 1998. Convergence properties of the Nelder–Mead simplex method in low dimensions. *Society for Industrial and Applied Mathematics: Journal of Optimization*, 9, pp.112–147.

Lunt, I.A., S.S. Hubbard & Y. Rubin, 2005. Soil moisture content estimation using ground-penetrating radar reflection data. *Journal of Hydrology*, 307(1-4), pp.254–269. Available at: http://linkinghub.elsevier.com/retrieve/pii/S0022169404005165 [Accessed October 23, 2014].

Mangel, A.R., B.A. Lytle & S.M.J. Moysey, 2015a. Automated high-resolution GPR data collection for monitoring dynamic hydrologic processes in two and three dimensions. *The Leading Edge*, 34(2), pp.190–195.

Mangel, A.R., S.M.J. Moysey & J. van der Kruk, 2015b. Resolving precipitation induced water content profiles by inversion of dispersive GPR data: A numerical study. *Journal of Hydrology*, 525, pp.496–505. Available at: http://linkinghub.elsevier.com/retrieve/pii/S0022169415002607.

Mangel, A.R., S.M.J. Moysey, J.C. Ryan & J.A. Tarbutton, 2012. Multi-offset ground-penetrating radar imaging of a lab-scale infiltration test. *Hydrology and Earth System Sciences*, 16(11), pp.4009–4022. Available at: http://www.hydrol-earth-syst-sci.net/16/4009/2012/ [Accessed October 23, 2014].

Mertens, J., H. Madsen, L. Feyen, D. Jacques & J. Feyen, 2004. Including prior information in the estimation of effective soil parameters in unsaturated zone modelling. *Journal of Hydrology*, 294(4), pp.251–269. Available at: http://linkinghub.elsevier.com/retrieve/pii/S0022169404001040 [Accessed October 23, 2014].

Moysey, S.M., 2010. Hydrologic trajectories in transient ground-penetrating-radar reflection data. *Geophysics*, 75(4), pp.WA211–WA219. Available at: http://library.seg.org/doi/abs/10.1190/1.3463416.

Mualem, Y., 1976. A new model for predicting the hydraulic conductivity of unsaturated porous media. *Water Resources Research*, 12(3).

Neal, A., 2004. Ground-penetrating radar and its use in sedimentology: principles, problems and progress. *Earth-Science Reviews*, 66(3-4), pp.261–330. Available at: http://linkinghub.elsevier.com/retrieve/pii/S0012825204000054 [Accessed September 26, 2014].

Neidell, N.S. & M.T. Taner, 1971. Semblance and other coherency measures for multichannel data. *Geophysics*, 36(3), pp.482–497.

Ratto, C.R., P. a. Torrione & L.M. Collins, 2011. Exploiting ground-penetrating radar phenomenology in a context-dependent framework for landmine detection and discrimination. *IEEE Transactions on Geoscience and Remote Sensing*, 49(5), pp.1689–1700.

Ritsema, C.J., L.W. Dekker, J.M.H. Hendrickx & W. Hamminga, 1993. Preferential flow mechanism in a water repellent sandy soil. *Water Resources Research*, 29(7), pp.2183–2193. Available at: http://doi.wiley.com/10.1029/93WR00394.

Rossi, M., G. Manoli, D. Pasetto, R. Deiana, S. Ferraris, C. Strobbia, M. Putti & G. Cassiani, 2015. Coupled inverse modeling of a controlled irrigation experiment using multiple hydro-geophysical data. *Advances in Water Resources*, 82, pp.150–165. Available at: http://linkinghub.elsevier.com/retrieve/pii/S0309170815000639.

Saintenoy, A., S. Schneider & P. Tucholka, 2007. Evaluating GroundPenetrating Radar use for water infiltration monitoring. *2007 4th International Workshop on, Advanced Ground Penetrating Radar*, pp.91–95. Available at: http://ieeexplore.ieee.org/lpdocs/epic03/wrapper.htm?arnumber=4278854.

Sato, M., Y. Yokota, K. Takahashi & M. Grasmueck, 2012. Landmine detection by 3D GPR system. In *Proceedings of SPIE*.

Simunek, J. & M.T. van Genuchten, 2005. HYDRUS code for simulating the movement of water, heat, and multiple solutes in variably saturated porous media.

Steelman, C.M. & A.L. Endres, 2010. An examination of direct ground wave soil moisture monitoring over an annual cycle of soil conditions. *Water Resources Research*, 46(11), p.n/a–n/a. Available at: http://doi.wiley.com/10.1029/2009WR008815 [Accessed October 23, 2014].

Steelman, C.M., A.L. Endres & J.P. Jones, 2012. High-resolution ground-penetrating radar monitoring of soil moisture dynamics: Field results, interpretation, and comparison with unsaturated flow model. *Water Resources Research*, 48(9), p.n/a–n/a. Available at: http://doi.wiley.com/10.1029/2011WR011414 [Accessed October 23, 2014].

Steelman, C.M., A.L. Endres & J. van der Kruk, 2010. Field observations of shallow freeze and thaw processes using high-frequency ground-penetrating radar. *Hydrological Processes*, 24(14), pp.2022–2033.

Stork, C., 1992. Reflection tomography in the postmigrated domain. *Geophysics*, 57(5), pp.680–692. Available at: http://library.seg.org/doi/abs/10.1190/1.1443282.

Strobbia, C. & G. Cassiani, 2007. Multilayer ground-penetrating radar guided waves in shallow soil layers for estimating soil water content. *Geophysics*, 72, pp.J17–J29.

Topp, G.C., J.L. Davis & A.P. Annan, 1980. Electromagnetic Determination of Soil Water Content: *Water Resources Research*, 16(3), pp.574–582.

Truss, S., M. Grasmueck, S. Vega & D.A. Viggiano, 2007. Imaging rainfall drainage within the Miami oolitic limestone using high-resolution time-lapse ground-penetrating radar. *Water Resources Research*, 43(3), p.n/a–n/a. Available at: http://doi.wiley.com/10.1029/2005WR004395 [Accessed October 22, 2014].

van der Kruk, J., 2006. Properties of Surface Waveguides Derived From Inversion of Fundamental and Higher Mode. *IEEE Transactions on Geoscience and Remote Sensing*, 44(10), pp.2908–2915.

van der Kruk, J., N. Diamanti, a. Giannopoulos & H. Vereecken, 2012. Inversion of dispersive GPR pulse propagation in waveguides with heterogeneities and rough and dipping interfaces. *Journal of Applied Geophysics*, 81, pp.88–96. Available at: http://linkinghub.elsevier.com/retrieve/pii/S0926985111002059 [Accessed October 23, 2014].

van der Kruk, J., R.W. Jacob & H. Vereecken, 2010. Properties of precipitation-induced multilayer surface waveguides derived from inversion of dispersive TE and TM GPR data. *Geophysics*, 75(4), pp.WA263–WA273. Available at: http://library.seg.org/doi/abs/10.1190/1.3467444.

van der Kruk, J., C.M. Steelman, a. L. Endres & H. Vereecken, 2009a. Dispersion inversion of electromagnetic pulse propagation within freezing and thawing soil waveguides. *Geophysical Research Letters*, 36(18), p.L18503. Available at: http://doi.wiley.com/10.1029/2009GL039581 [Accessed October 23, 2014].

van der Kruk, J., R. Streich & A.G. Green, 2006. Properties of surface waveguides derived from separate and joint inversion of dispersive TE and TM GPR data. *Geophysics*, 71(1), pp.K19–K29. Available at: http://library.seg.org/doi/abs/10.1190/1.2168011.

van der Kruk, J., H. Vereecken & R.W. Jacob, 2009b. Identifying dispersive GPR signals and inverting for surface wave-guide properties. *The Leading Edge*, pp.1234–1239.

van Genuchten, M.T., 1980. A Closed-form Equation for Predicting the Hydraulic Conductivity of Unsaturated Soils. *Soil Science Society of America Journal*, 44(5), p.892.

van Overmeeren, R.A., S.. Sariowan & J.. Gehrels, 1997. Ground penetrating radar for determining volumetric soil water content; results of comparative measurements at two test sites. *Journal of Hydrology*, 197(1-4), pp.316–338. Available at: http://linkinghub.elsevier.com/retrieve/pii/S0022169496032441.

Vellidis, G., M.C. Smith, D.L. Thomas & L.E. Asmussen, 1990. Detecting wetting front movement in a sandy soil with ground-penetrating radar. *American Society of Agricultural Engineers*, 33(6), pp.1867–1874.

Yang, C.-C. & N.K. Bose, 2005. Landmine detection and classification with complex-valued hybrid neural network using scattering parameters dataset. *IEEE transactions on neural networks / a publication of the IEEE Neural Networks Council*, 16(3), pp.743–753.

Yapo, P.O., H.V. Gupta & S. Sorooshian, 1998. Multi-objective global optimization for hydrologic models. *Journal of Hydrology*, 204(1-4), pp.83–97. Available at: http://linkinghub.elsevier.com/retrieve/pii/S0022169497001078.

Yilmaz, O. & R. Chambers, 1984. Migration velocity analysis by wave-field extrapolation. *Geophysics*, 49(10), pp.1664–1674.

Yilmaz, O. & S. Doherty, 2001. *Seismic Data Analysis: Processing, Inversion, and Interpretation of Seismic Data* 2nd ed., Tulsa, OK: Society of Exploration Geophysicists.

Zyada, Z., T. Matsuno, Y. Hasegawa, S. Sato & T. Fukuda, 2011. Advances in GPR-based landmine automatic detection. *Journal of the Franklin Institute*, 348(1), pp.66–78. Available at: http://linkinghub.elsevier.com/retrieve/pii/S0016003209000337 [Accessed October 16, 2014].